The potential of FPV for inland waters in the Netherlands

Eline Bouma

Delft University of Technology

TU Delft

The potential of FPV for inland waters in the Netherlands

by

Eline Bouma

to obtain the degree of Master of Science
Sustainable Energy Technology
at the Delft University of Technology,
to be defended publicly on Wednesday April 29, 2026 at 09:30 AM.

Student number:	5321719	
Project duration:	September 9, 2025 – April 29, 2026	
Supervisor:	Dr. Rudi Santbergen	(PVMD)
Daily supervisor:	Mehmet Korkmaz	(PVMD)
Internal committee member:	Prof. Arno Smets	(PVMD)
External comittee member:	Dr. Wenli Shi	(DCE&S)

Cover: Taken from [1]

TU Delft

Abstract

This thesis evaluates the potential of floating photovoltaics (FPV) on inland waters in the Netherlands. As a densely populated country aiming to achieve climate neutrality by 2050, the Netherlands faces significant spatial constraints for renewable energy deployment. FPV offers a promising solution, as it does not compete for land use and may achieve higher efficiency due to the cooling effect of water.

A scenario-based approach is applied to assess both the spatial and energy potential of FPV. Nine scenarios are defined based on variations in panel tilt angle, distance from shore, and surface coverage of water bodies. Suitable deployment areas are identified using a Geographical Information System (GIS), considering spatial exclusions such as protected areas and navigation routes, as well as minimum capacity requirements. The DC energy yield is subsequently estimated using the PVMD Toolbox, incorporating spatially interpolated weather data and thermal and electrical performance models.

The results indicate that FPV systems could occupy areas ranging from 3.7 to 27.7 km², corresponding to an annual energy yield between 0.3 and 4.8 TWh. After accounting for conversion losses, the most promising scenario could supply approximately 3.1% of the national electricity demand. These findings highlight the potential contribution of FPV to the Dutch energy transition, while remaining subject to scenario-based assumptions regarding system design and environmental conditions.

Preface

I would like to express my sincere gratitude to my supervisors, Rudi Santbergen and Mehmet Korkmaz, for their continuous support, valuable insights, and guidance throughout this thesis. I truly enjoyed working on this topic, and their encouragement made this work possible. I would also like to thank Youri Blom for his support and for patiently answering all my questions regarding the PVMD Toolbox. Furthermore, I would like to extend my appreciation to the committee members, Arno Smets and Wenli Shi, for taking the time to evaluate my thesis.

Eline Bouma
Delft, April 2026

Contents

Nomenclature 6

List of Figures 7

List of Tables 9

1 Introduction 1
- 1.1 Background on Floating Photovoltaics (FPV) . . . 2
- 1.2 Advantages of FPV . . . 3
  - 1.2.1 Land use efficiency . . . 3
  - 1.2.2 Higher energy efficiency . . . 4
- 1.3 Thesis objectives and scope . . . 5
- 1.4 Thesis outline . . . 5

2 Literature review 6
- 2.1 FPV Technologies . . . 6
  - 2.1.1 Floating structure . . . 6
  - 2.1.2 Mooring system . . . 7
  - 2.1.3 Design choices for FPV . . . 8
- 2.2 Site suitability criteria . . . 10
  - 2.2.1 Exclusion Criteria . . . 10
  - 2.2.2 Ranking criteria . . . 12
- 2.3 Energy yield assessment methods . . . 12
  - 2.3.1 Empirical methods . . . 12
  - 2.3.2 Machine Learning approaches . . . 12
  - 2.3.3 Simulation based approaches . . . 13
  - 2.3.4 FPV modeling enhancements . . . 13
  - 2.3.5 Additional FPV losses . . . 14
- 2.4 Summary and knowledge gaps . . . 15

3 Available area 16
- 3.1 Definition of the Scenarios . . . 16
- 3.2 Data sources . . . 17
- 3.3 Processing software . . . 18
- 3.4 Results . . . 24
- 3.5 Discussion . . . 25
- 3.6 Conclusion . . . 26

4 Energy yield 27
- 4.1 Scenario Definition & Assumptions . . . 27
- 4.2 Energy yield modeling . . . 28
- 4.3 Results . . . 32
- 4.4 Discussion . . . 34
- 4.5 Conclusion . . . 35

5 Conclusion 36

6 Recommendations 37

A Appendix GIS-based assessment 45
- A.1 Selection of FPV system . . . 45
- A.2 Power Density calculation . . . 46
- A.3 QGIS interface . . . 47
- A.4 Overpass Query . . . 48
  - A.4.1 Water data . . . 48
  - A.4.2 Unsuitable Areas . . . 48

A.5 Step 1. C Validation 49
A.6 Site Selection Criteria 51
A.7 Datasheet selected FPV module 53

B Appendix Energy yield **56**
B.1 Shading impact analysis 56
B.2 Wave Induced Losses modelling 57
B.3 Selection of surface albedo 58
B.4 Meteorological data 58
B.4.1 Selection of meteorological data source. 58
B.4.2 Adjustments for solar azimuth and solar altitude variables 60
B.4.3 Spatial interpolation 61
B.5 Provincial results 65
B.6 Spatial distribution of Specific Yield 66

Nomenclature

$4P25S$	4 in parallel, 25 in series configuration
α	Design solar altitude angle [°]
β	PV tilt angle [°]
A_z	Solar azimuth angle [°]
A_{alloc}	Allocated surface area (Area covered by FPV grid blocks) [km^2]
A_{array}	Effective array area (Area covered by FPV panels) [km^2]
AMY	Actual Meteorological Year
APV	Agriculture Photovoltaics
$BIPV$	Building Integrated Photovoltaics
$BSRN$	Baseline Surface Radiation Network
DHI	Direct Horizontal Irradiation [W/m^2]
DNI	Direct Normal Irradiation [W/m^2]
EY	Energy yield [GWh]
fid	Feature identifier
FPV	Floating Photovoltaics
$G_{DNI-cor}$	Corrected DNI irradiation term [W/m^2]
G_{POA}	Plane of array irradiation
GHI	Global Horizontal Irradiation [W/m^2]
GIS	Geographical Information System
$GMPV$	Ground-Mounted Photovoltaics
h_s	Solar altitude angle[°]
$HDPE$	High-Density Polyethylene
IDW	Inverse Distance Weighting
$LOOCV$	Leave-one-out cross-validation
$MCDA$	Multi-Criteria Decision Analysis
$NOCT$	Nominal Operating Cell Temperature
$O\&M$	Operations and maintenance
OPV	Offshore Photovoltaics
OSM	Open Street Map
PV	Photovoltaics
$PVMD$	Photovoltaic Materials and Devices
$QGIS$	Quantum Geographical Information System

$RIVM$ Rijksinstituut voor Volksgezondheid en Milieu

$RMSE$ Root mean square error

RPV Rooftop Photovoltaics

SHJ Silicon hetero junction

$SMARTS$ Simple Model of the Atmospheric Radiative Transfer of Sunshine

STC Standard Test Conditions

SY Specific yield [kWh/kWp]

T_a Air temperature at 2 meters height [°C]

TMY Typical Meteorological Year

$TRLs$ Technology Readiness Levels

U Thermal transmittance [W/(m^2*K)]

v_w Wind speed at 10 meters height [m/s]

WIL Wave-induced losses

PVsyst PhotoVoltaic System (Software)

List of Figures

1.1 Study map area of the Netherlands [8]. . . . 2
1.2 Schematic of FPV system on a lake connected to the onshore transmission system. Taken from [9] and enhanced with AI (Artlist). . . . 2
1.3 Global FPV development by installed capacity (MWp) and percentage of FPV over total global PV installations [11]. . . . 3
1.4 Land use distribution in the Netherlands in 2017 [12]. . . . 4

2.1 Overview of categorization of FPV structures. Pictures of FPV structures taken from [29, 30]. . . . 7
2.2 FPV buoyancy structures [30]. . . . 7
2.3 Different types of mooring and anchors, taken from [30]. . . . 7
2.4 Monofacial VS bifacial solar panels [38]. . . . 8
2.5 Different orientations for PV panels [40]. . . . 9
2.6 The tilt angle β and height shown in a schematic for FPV. . . . 9
2.7 Types of tracking systems for PV, taken from [46] and enhanced. . . . 10

3.1 Schematic presenting the side view for Scenario 1 (0° tilt, 25 m buffer), Scenario 2 (15° tilt, 50 m buffer), Scenario 3(38° tilt, 100 m buffer) . . . 17
3.2 Workflow for acquiring suitable areas for FPV . . . 19
3.3 Example of the water body *Delftse Hout* suitable for Scenario 1, showing the inner buffer zone (−25 m), the rectangles fully contained within the buffer zone (R_buffer), and the number of rectangles corresponding to 5% coverage (R_5%). . . . 23
3.4 Two graph showing the allocated and effective area [km^2] for FPV deployment in the Netherlands per scenario under different coverage percentages. The effective area is decreased substantially. . . . 24
3.5 FPV potential of installation capacity . . . 25
3.6 Allocated surface area A_{alloc} per province in the Netherlands for Scenario 2, 10% coverage. 25

4.1 Flowchart of obtaining the energy yield . . . 29
4.2 Sensitivity map of Scenario 1 (0° tilt angle). . . . 30
4.3 Energy yield results . . . 32
4.4 Spatial variability for Specific yield for Scenario 2 at 15 % FPV coverage . . . 33
4.5 Monthly specific yield for three scenarios for the water body denoted as “element 10” [53.17, 6.57] (Groningen) . . . 33
4.6 Total energy yield EY per province in the Netherlands for Scenario 2, 10% coverage. . . . 34

A.1 4P25S configuration: system top and side views . . . 45
A.2 Side view of $W_{mod}(\alpha_{cap})$ per scenario, showing that Scenario 2, 3 shading gap utitizes maintenance gap and intermodule spacing effectively . . . 46
A.3 Trade-off between POA irradiance losses and power density for weather station De Bilt . 47
A.4 Example of QGIS interface . . . 47
A.5 Workflow validation OSM data . . . 50
A.6 Example of the spatial overlap analysis near Vlaardingen, Zuid-Holland (51.94°N, 4.32°E). Seven OSM water bodies are displayed with overlap ratios of (1) 79.8%, (2) 81.8%, (3) 96.0%, (4) 85.0%, (5) 0%, (6) 97.2%, and (7) 31.6%, illustrating the Full (90–100%), Partial (50–90%), and None (<50%) agreement categories. . . . 50
A.7 Distribution of feature-level overlap ratios between filtered OSM water and classified water map. . . . 51

B.1 Wave-induced losses estimated from the data of [79] using a fitted Fourier series for two tilt angles. . . . 57

B.2 Daytime Albedo Variation (De Bilt) 58
B.3 Comparison between the distribution of the meteorological data locations 59
B.4 Estimation of calculated variables after `pvlib` adjustments for LOOCV method at 36 days 61
B.5 RMSE comparison for the four interpolation methods across the five evaluated variables . 62
B.6 Interpolation technique (IDW) performance for 5 variables 63
B.7 Ranges of Interpolated elements vs weather stations 64
B.8 Comparison of Specific Yield (SY) across three scenarios(coverage percentage 15%) . . 67

List of Tables

2.1 Various studies on the gain of tracking FPV system compared to fixed FPV system. . . . 10
2.2 Site exclusion criteria and thresholds for unsuitable areas. . . . 11
2.3 Adjusted parameter values in [10] compared to default PVsyst. . . . 13
2.4 Findings of [43] on wind direction impact on diverse tilt angles of FPV. . . . 14
2.5 Temperature of FPV cell under different wind speed conditions from [43]. . . . 14
2.6 Total efficiency of FPV under wave different conditions [78]. . . . 14

3.1 Description of the nine scenarios, combining three tilt angles and buffer zones with three FPV coverage percentages . . . 17
3.2 Distinct data formats, query for the water body extraction for city in the Netherlands (Delft), resulting in different file sizes . . . 18
3.3 Water Data by Province from Overpass Turbo Query . . . 20
3.4 Power density and required area [km^2] per scenario to achieve 2 MW_p capacity at different FPV coverage levels. . . . 21
3.5 Inland Water Bodies by Province after Step 4.B . . . 21
3.6 Dimensions of FPV system per Scenario . . . 22
3.7 Potential FPV water bodies and area in the Netherlands for different scenarios, where elements is the amount of water bodies found, A_{alloc} is the allocated surface area in [km^2] and A_{array} the effective array area in [km^2]. . . . 24
3.8 FPV potential capacity for different scenarios in [GW_p]. . . . 25

4.1 Description of the nine scenarios, combining three tilt angles and buffer zones with three FPV coverage percentages . . . 27
4.2 Description of meteorological variables required for the PVMD toolbox . . . 30
4.3 RMSE statistics for LOOCV for 36 datapoints for the variables using pvlib and IDW interpolation . . . 31
4.4 Energy yield of FPV system for distinct scenarios, where EY is the total energy yield in TWh, SY is the specific yield in kWh/kWp, with SY_μ representing the mean value, and SY Range the range across water bodies. . . . 32

A.1 Simulated scenarios with selected sun altitude of $14.4°$ . . . 47
A.2 Distribution of overlap ratio categories . . . 51
A.3 Long-term averages of terrain and climatic factors of the Netherlands . . . 52
A.4 Site selection criteria for floating photovoltaic (FPV) deployment based on literature review 52

B.1 Solar altitude angles based on tree height and distance for different scenarios . . . 56
B.2 Average shading angles for Scenario 1 under different FPV coverage percentages . . . 57
B.3 Average Daytime Albedo for Weather Stations . . . 58
B.5 Comparison of GHI, DNI, and DHI from different datasets with respect to reference. Values are shown as $value \pm error$ (kWh/m² or %). . . . 59
B.4 Geographical coordinates of the 34 Meteonorm meteorological stations . . . 60
B.6 RMSE statistics across 34 weather stations for solar azimuth angle (A_z) and solar altitude angle (h_s) . . . 61
B.7 Comparison of interpolation method performance using RMSE for each variable . . . 62
B.8 Provincial division of potential FPV for Scenario 1, where A_{alloc} is the allocated area in km^2, EY is the energy yield in GWh, SY_μ is the mean specific yield in kWh/kWp . . . 65
B.9 Provincial division of potential FPV for Scenario 2, where A_{alloc} is the allocated area in km^2, EY is the energy yield in GWh, SY_μ is the mean specific yield in kWh/kWp . . . 65
B.10 Provincial division of potential FPV for Scenario 3, where A_{alloc} is the allocated area in km^2, EY is the energy yield in GWh, SY_μ is the mean specific yield in kWh/kWp . . . 66

1

Introduction

Approximately 20% of the total surface area of the Netherlands (Figure 1.1) consists of water, and the country is densely populated. The goal of the Netherlands is to achieve climate neutrality by 2050 [2]. One way to achieve this is to use solar energy. There are four main types of solar energy: Photovoltaic (PV), thermal, passive and hybrid. TNO, a Dutch company, states that PV electricity production should reach 200 GW_p by 2050 [3]. However, the cumulative solar photovoltaic capacity in the Netherlands in 2024 was only 24 GW_p [4], meaning that a significant amount of additional capacity is required. In PV technology there are six types of installations [5, 6]: (1) Ground-mounted PV (GMPV), (2) Building integrated PV (BIPV), (3) Agriculture PV (APV), (4) Rooftop PV (RPV), (5) Offshore PV (OPV), (6) Floating PV (FPV). While RPV is becoming increasingly full, with 33% already occupied [7], and most of the land is being used for other purposes, there is little land available for GMPV. The abundance of water reservoirs and inland waterways in the Netherlands makes FPV systems a promising alternative for solar energy generation. Exploring this technology could contribute significantly to the transition to a fossil-free future by 2050. This chapter introduces the topic of the thesis: the potential of FPV in the Netherlands for inland waters. Section 1.1 focuses on the background of FPV and Section 1.2 highlights its advantages. The research objectives and scope are defined in Section 1.3 and the thesis outline is provided in Section 1.4.

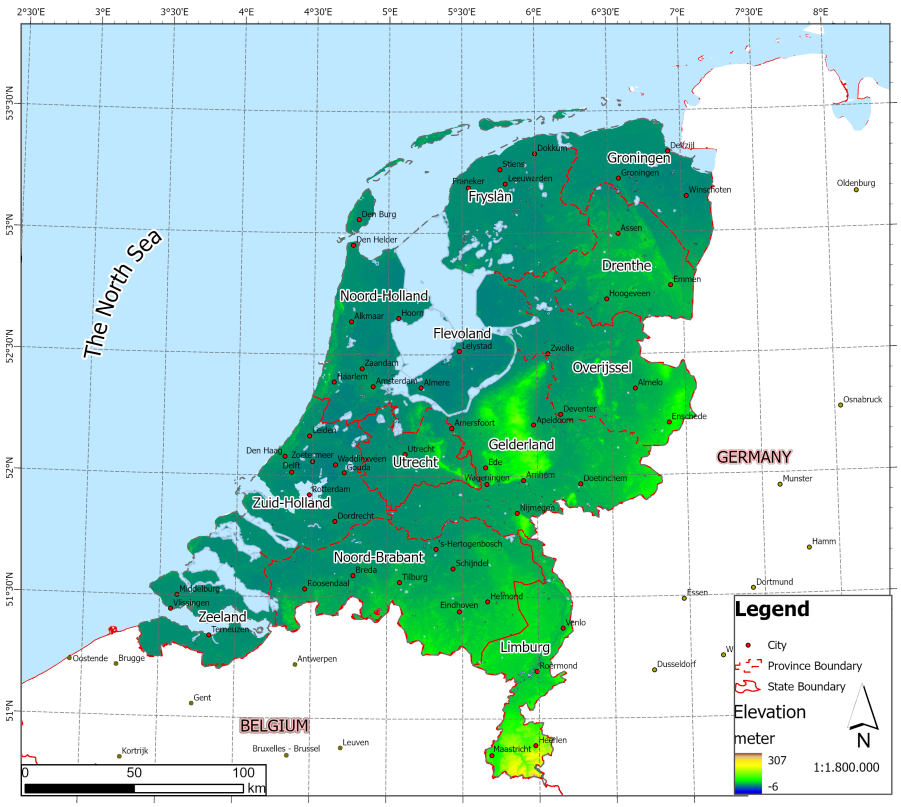

Figure 1.1: Study map area of the Netherlands [8].

1.1. Background on Floating Photovoltaics (FPV)

As the name suggests, floating photovoltaics (FPV) are solar panels installed on structures that float on water. FPV consists of the following components: (1) PV modules, (2), floats or pontoons, (3) mooring lines and anchoring, (4) inverter, (5) underwater cables, and (6) combiner box, (7) lighting protection system, as is illustrated in Figure 1.2 [9].

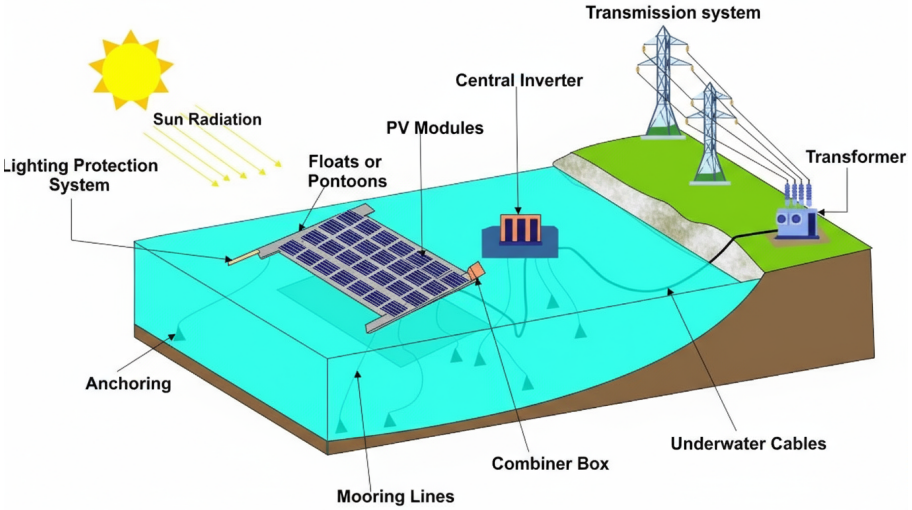

Figure 1.2: Schematic of FPV system on a lake connected to the onshore transmission system. Taken from [9] and enhanced with AI (Artlist).

Solar panels are mounted on a floating structure called a pontoon, which is secured to the bottom of a water body by mooring lines and anchoring. The mooring system is able to adjust the water level fluctuations while maintaining its position [10]. The PV panel absorbs the photons of solar radiation

and transforms them into DC electricity. The inverter is then used to convert this DC output into an AC current suitable for the electricity grid, which is then transported by an underwater cable to land. The inverter location depends on the design of the FPV system; in some cases, it is placed directly on the floating structure or on land.

Throughout the years, FPV has developed globally and will continue to do so, as is illustrated in Figure 1.3 [11]. The blue bars on the left-hand y-axis represent the cumulative global installed FPV capacity in MWp, while the red line on the right y-axis represents the percentage of installed FPV over total installed PV capacity for that year. As can be seen, the proportion of FPV is very small compared to PV: in 2022, it was only 0.5%.

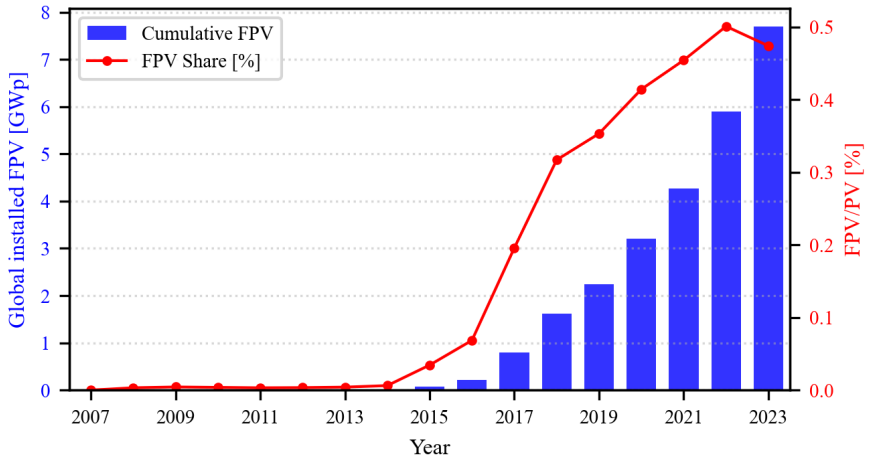

Figure 1.3: Global FPV development by installed capacity (MWp) and percentage of FPV over total global PV installations [11].

1.2. Advantages of FPV

Given that the current FPV technology has not fully developed and is still in its early stages, why should one focus on this technology rather than other types of PV technology, such as GMPV and RPV, which are much larger? Well, FPV has some advantages over other PV technoglogies and these will be discussed in Sections 1.2.1, 1.2.2 and 1.2.3.

1.2.1. Land use efficiency

A primary advantage of FPV is its ability to save land usage. The Netherlands is a very small country with 4,154,000 hectare (ha) as surfurce area. In Figure 1.4 [12] the land use distribution is shown for the Netherlands in 2017, it can be observed that approximately 50% of the land is used for agriculture, 20% for water (inland and tidal), 10% for built-up and semi built-up areas, and the remaining portions for other uses (recreation, transport, woodland and nature).

Agriculture constitutes the largest share of land use. The Netherlands is the second-largest exporter of agricultural produce in the world, exporting approximately €65 billion of agricultural products annually [13]. Therefore, the agricultural land must remain available for its current purposes and cannot be repurposed for the installation of solar panels to meet energy demand. Even if portions of agricultural land were considered for energy generation for GMPV, the associated costs would be tremendous. In 2023, the average price of arable land (i.e. agricultural land that is used for the production of crops for food or feed supply) in the Netherlands is €91,200/ha. By comparison, the estimated value of arable land in the European Union (EU-27) was €11,800/ha, indicating that land in the Netherlands is 7.7 times more expensive. Looking at historical data, the price of arable land in the Netherlands in 2014 was only €56,600/ha, which means that the price has increased with 61% [14]. This high increase can be attributed to the annual growth of the country's population between 0.4% and 1.05% in the last decade [15], which has reduced available land and consequently increased land prices.

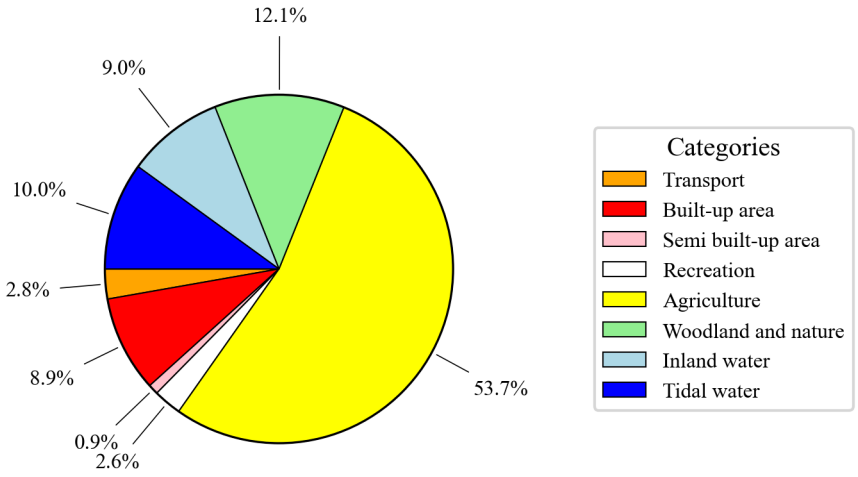

Figure 1.4: Land use distribution in the Netherlands in 2017 [12].

The second-largest land category is water, which offers potential for FPV deployment. Of this, 10% consists of Tidal water. However, due to the stronger flows and higher wave conditions, this has been excluded from the scope of the thesis. Further research on this topic is possible, but would require a different type of technology, OPV, and is therefore not considered here. The remaining 9% consists of inland water, which can be examined as a feasible option for FPV installation. Furthermore, according to Vasuki et al. [16] the Technology Readiness Levels (TRLs) of inland FPVs are higher than those of OPV, making it more profitable to install inland FPV, which have more mature technology.

Built-up and semi built-up area consists of another 10% of the land use in the Netherlands. While these areas present opportunities for RPV, rooftop spaces are increasingly utilized, with an estimated annual increase of 4 GW_p [17]. As such, rooftop solar is already considered a mature application.

The remainder of land use is attributed to recreation, transport, woodland and nature. Recreational areas are essential for the well-being of the population and should not be reduced, as it would result in highly negative social impacts. Transport infrastructure (including roads, railways, and airports) is indispensable for mobility and therefore unsuitable for solar deployment. Woodland and nature reserves must also be preserved to protect biodiversity, maintain critical ecosystem services such as clean air and water and store carbon for climate change mitigation. Furthermore, the woodland and nature reserves contribute to the well-being of the population as well.

Population growth, as was mentioned earlier, has also contributed to a rising energy demand. As a result, it is essential to use the limited available space efficiently to ensure sufficient energy production. However, because GMPV systems are not feasible due to high land prices and competing land-use demands, and because rooftops are increasingly occupied, FPV systems may offer a viable solution.

1.2.2. Higher energy efficiency

FPV systems are also more efficient (i.e. achieving maximum productivity with minimum dissipated power) than GMPV. This is because water has a cooling effect and reduces dust deposition by enabling easier cleaning of the system [18, 19]. Since the performance of solar panels is greatly influenced by environmental factors such as temperature, soiling and albedo, the potential of FPV varies from location to location. For example, locations with dry climates experience more dust accumulation and higher temperatures, resulting in a bigger difference in performance if FPV is implemented than locations with higher moisture levels and colder temperatures. More specifically, high temperatures can reduce solar PV efficiency by 0.4–0.5%/°C [20]. The water surface on which the FPV system is mounted acts as a passive cooling medium by absorbing heat from the system without requiring additional energy. Once the heat has been removed, the module temperature does not increase, allowing the system to cool down and enhance its performance. For example, a study conducted in Bangladesh from May to June revealed that the average improvement in the efficiency of FPV compared to GMPV over 2 days of tracking was 6.25% [21]. In another study [22] the efficiency of FPV was reported to be 16% higher than that of land-based solar plants. According to the Dutch company TNO [23] the best performing FPV systems have an increased efficiency of up to 3% in the Netherlands and up to 6% in Singapore, compared to the GMPV systems.

Another environmental facor that influences the performance of PV systems is soiling, which can reduce their output by up to 60%[20]. There are two techniques for the cleaning of FPV: water-based and water-free. According to Rafi Zahedi et al. [24] the water-based technique is the most effective cleaning method. Fortunately, the water surrounding the FPV system makes cleaning more accessible. In one study [25], a robot is proposed for cleaning the solar panels, in order to improve the efficiency of energy generation. The advantage of using a robot is that most floating PV systems are far from land and difficult to access.

1.3. Thesis objectives and scope

This thesis is motivated by the desire to transition to a renewable future and explore the new technology of FPV to reveal its full potential. As said before: the site's potential and the possible benefits of FPV should be examined closely, as there is no single number that applies to all locations. The main research question is as follows: **What is the potential of FPV for inland waters in the Netherlands?**
The research is divided in two main areas, with the following sub-questions:

1. What is the total area [km^2] of suitable inland water sites in the Netherlands for deploying FPV systems?
2. What is the annual energy yield [TWh] of the suitable FPV systems in the Netherlands?

This thesis focuses on two main aspects: the identification of suitable water bodies and the estimation of energy yield. Based on nine scenarios defined in this study, suitable inland water bodies for FPV deployment are identified. The second aspect concerns estimating the DC energy yield of FPV systems, which is essential for evaluating their realistic performance.

1.4. Thesis outline

The thesis structure will be as follows: Chapter 2 contains the literature review, Chapter 3 and Chapter 4 address the Research Questions 1 and 2 repsectively, Chapter 5 provides the conclusion, Chapter 6 recommends future work.

2

Literature review

This chapter presents a comprehensive review of the existing literature on Floating Photovoltaic (FPV) systems. The aim is to establish a clear understanding of the current state of research, identify key technological developments, and highlight knowledge gaps relevant to this study. Section 2.1 discusses the technological aspects of FPV systems, including the categorization of floating structures, mooring configurations, and design considerations influencing system performance and durability. Section 2.2 examines the site suitability criteria for FPV deployment, emphasizing environmental, technical, and socio-economic factors that determine the feasibility of installations. Section 2.3 reviews the energy yield assessment methods used in FPV studies. It explores the methodologies for predicting FPV energy output, the modelling of module temperature, and other factors affecting overall system performance. Finally, Section 2.4 summarizes the literature review and addresses knowledge gaps.

2.1. FPV Technologies

Section 2.1 discusses the technological aspects of FPV systems, including the categorization of floating structures, mooring configurations, and design considerations influencing system performance and durability.

2.1.1. Floating structure

The general floating structure of FPV systems can be categorized in various ways. Figure 2.1 provides an overview. The dotted line in Figure 2.1 represents a conceptual bridge connecting different classifications and their structural overlap. One way to categorize FPV structures is to distinguish between zero-air-gap and high-air-gap platforms [26]. Zero-air-gap platforms closely follow the water surface, exhibiting wave-following motion characteristics, while high-air-gap platforms elevate PV modules safely above the wave surface, preventing wave overtopping. Some researchers categorize FPV structures in three different classes [27]: Class 1 includes hybrid rafts HDPE (High-Density Polyethylene) floats with metal frame, Class 2 involves pure HDPE float modules (without a metal structure), and Class 3 contains pontoon platforms, flexible and rigid membranes, and elevated decks. Other researchers, such as Claus et al. [28], considered the same three classes, except that Class 3 excluded flexible and rigid membranes, treating them as a separate category.

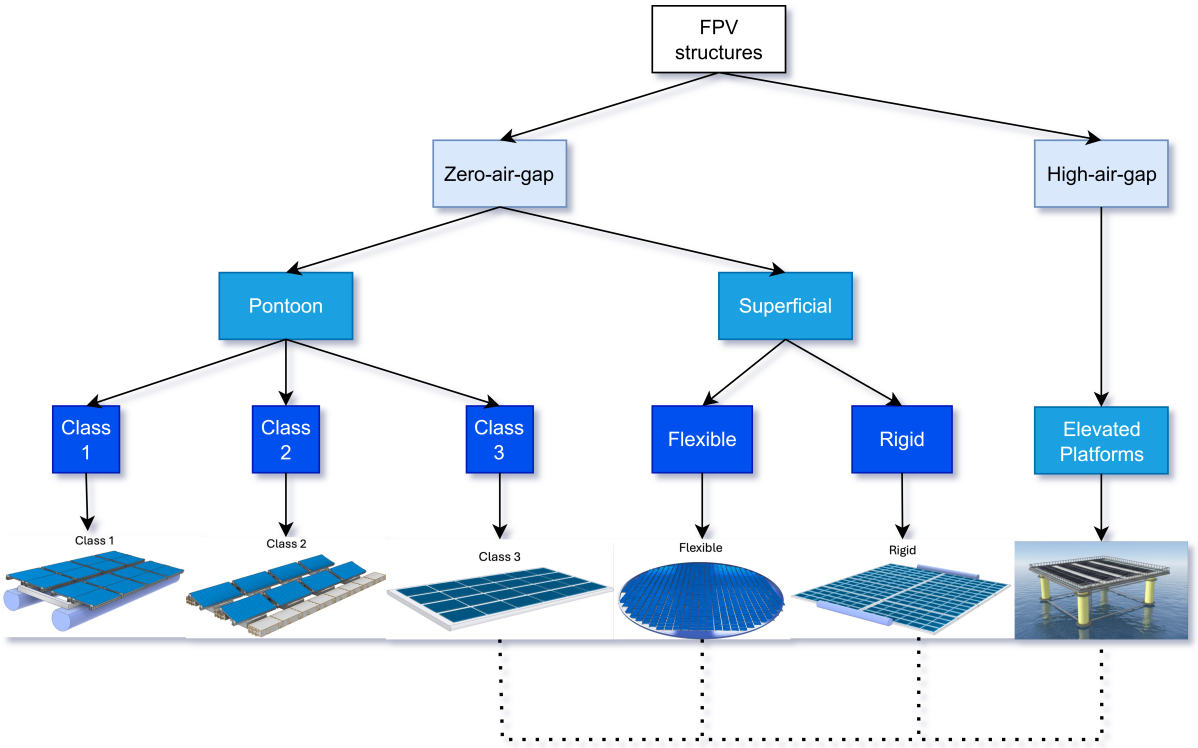

Figure 2.1: Overview of categorization of FPV structures. Pictures of FPV structures taken from [29, 30].

Another way to categorize the FPV is shown in Figure 2.2 [30]: Pure floats (Class 2), modular rafts (Class 1), membranes (Class 3), and elevated platforms (Class 3).

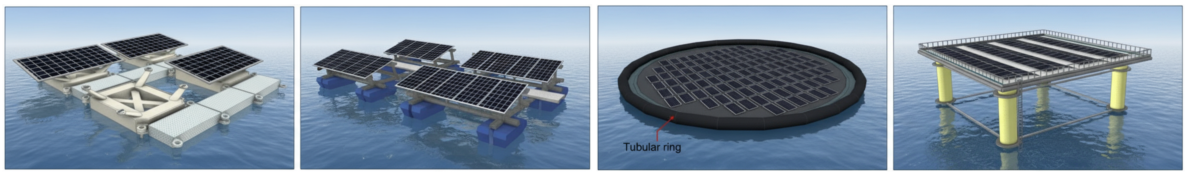

Figure 2.2: FPV buoyancy structures [30].

2.1.2. Mooring system

The floating structure is secured by mooring lines anchored to the bed of the water body. The mooring system is essential because it minimizes the movement of FPV and it manages varying water levels [31]. Mooring types can be categorized into four types: *Catenary, Compliant, Taut and Rigid* (Figure 2.3a) [28]. And anchors can be categorized into four types as well: *Dead-weight/Gravity, Drag, Pile, and Plate* (Figure 2.3b) [32].

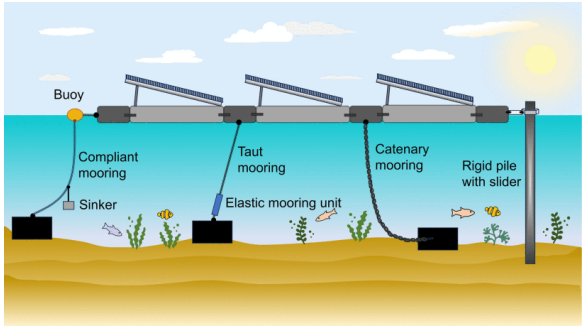

(a) Types of moorings.

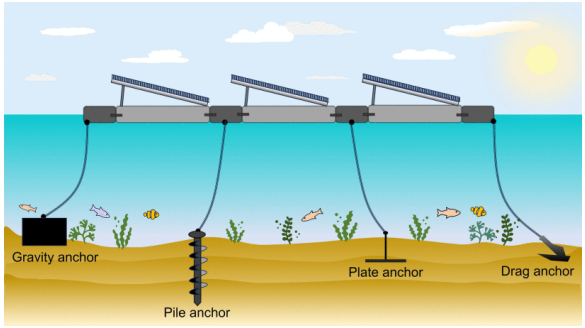

(b) Types of anchors.

Figure 2.3: Different types of mooring and anchors, taken from [30].

The mooring system is site-specific, depending on factors such as topography, soil conditions, water depth and level variation, bathymetry (the measurement of underwater depths), environmental conditions, and marine growth[33]. Therefore, a detailed site-specific analysis is essential to select the most suitable system[31]. A case study conducted by Ghigo et al. [34] analyzed three FPV sites with different characteristics in Lampedusa. Site A had an average water depth of 50 m, site B 80 m, and site C 75 m. Because site A was the shallowest, it resulted in the lowest mooring system costs. Conversely, site B, being the deepest, had the highest costs due to the greater amount of material required. The water depth plays an crucial role in determining the costs, as deeper waters require more materials (higher costs) to secure the mooring lines to the anchors.

2.1.3. Design choices for FPV

Several design choices play a crucial role in determining the energy yield of a PV system. These include the selection between bifacial and monofacial panels, the module orientation (landscape or portrait), and structural parameters such as tilt angle and mounting height. Additionally, the choice between fixed-tilt configurations and tracking systems further influences overall performance. All the design choices are discussed in the following sections.

Bifaciality

Firstly, the FPV modules can be chosen to be either monofacial or bifacial. The difference between the two is that monofacial only absorbs sunlight from the front surface, while bifacial solar panels absorb sunlight from both the front and back surfaces, as is shown in Figure 2.4. A study conducted in the United Kingdom by Araimi et al. [35] showed that the bifacial FPV outperforms monofacial FPV by 6.59%. Another study performed by Tina et al. [36] showed that bifacial gain for FPV systems varies depending on the location. For example, a more northern location with higher diffuse fraction (Germany) had a bifacial gain of 4%, while a more southern area (Italy) had a bifacial gain of 3%. Ziar et al. [37] demonstrated in a study that the bifacial gain was between 19.5% and 21.5% depending on the FPV configuration.

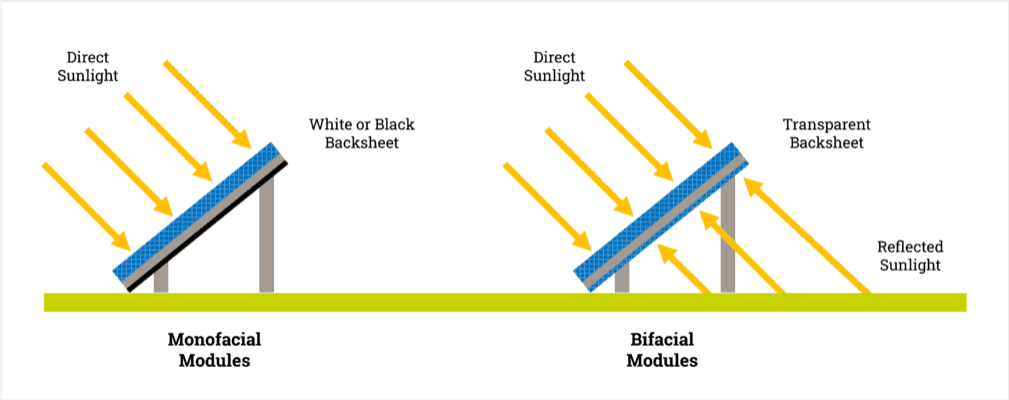

Figure 2.4: Monofacial VS bifacial solar panels [38].

PV orientation

Another design choice that influences the energy yield is the orientation, which can be either landscape or portrait. In landscape orientation, a solar panel is mounted horizontally, wider than it is tall. In portrait orientation, it is mounted vertically, taller than it is wide, as is shown in Figure 2.5. For the same PV module technology, the landscape configuration facilitates better cooling than the portrait configuration mainly due to the proximity to the water surface[39].

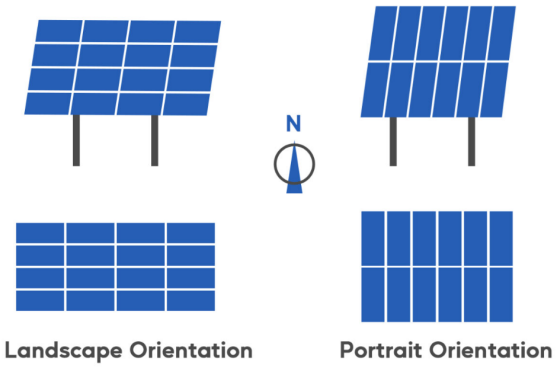

Figure 2.5: Different orientations for PV panels [40].

PV tilt angle and mounting height

Furthermore, the tilt angle and the height can influence the performance of FPV as well. The tilt angle is defined as the angle of its slope relative to the horizontal ground, denoted as β in Figure 2.6. The mounting height is measured from the point where the bottom of the floating structure touches the water surface up to the PV panel, as is shown in Figure 2.6 as height. A study conducted by Hammoumi et al. [41] in Fez examined the energy production of the FPV under different tilt angles, ranging from 0°to 30°(the optimal tilt for the location). It was observed that the optimal tilt (30°) resulted in an increase of 43.5% energy generation, compared to the 0°tilt angle. Another study [42] examined the cooling effect of FPV under different angles. Comparisons were made between FPV and GMPV under Nominal Operating Cell Temperature (NOCT) conditions. The best performance FPV was at 0°tilt angle and at a height of 1.5 meter. They concluded that the tilt angle should be less than 45°, FPV performed worse than GMPV at those tilt angles.

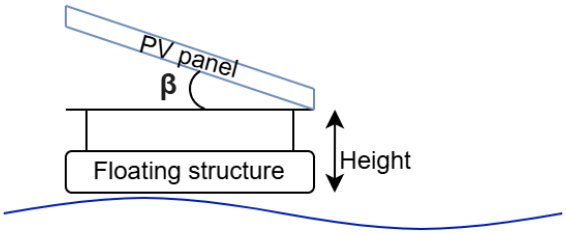

Figure 2.6: The tilt angle β and height shown in a schematic for FPV.

In contrast, another study [43] found that improved cooling performance was achieved at a tilt angle of $10°$. While Nisar et al. [44] reported that cooling effects are most effective at a tilt angle of $0°$, the FPV modules generate 10–17% more energy when installed at a $30°$ tilt. Another study [45] conducted in Indonesia evaluated three different configurations of FPV height and tilt angle. The highest performance was achieved through optimization using the PhotoVoltaic System (PVsyst) software, which determined the optimal height, azimuth, and tilt angle by systematically varying these parameters. The resulting optimal tilt angle was $\beta = 8.3°$, although the location-specific optimal value is $\beta = 10°$.

Tracking system

Consequently, the tracking system of FPV can improve the performance of FPV. Fixed solar panels are stationary, while tracked solar panels follow the sun's path in a variety of directions as is shown in Figure 2.7.

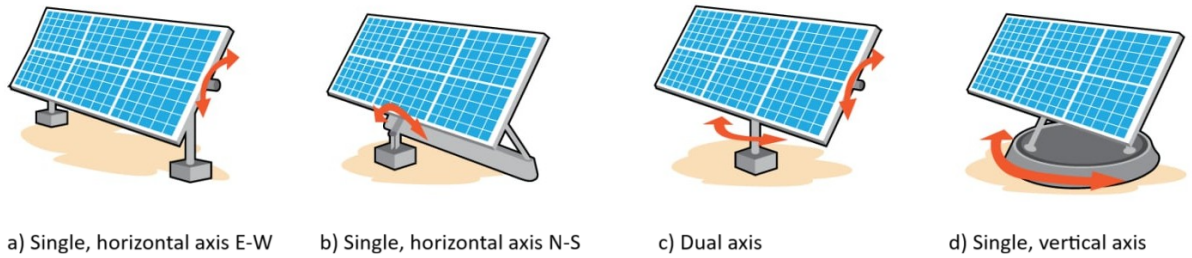

Figure 2.7: Types of tracking systems for PV, taken from [46] and enhanced.

Table 2.1 shows various studies comparing the tracking FPV system to the fixed FPV system. Tina et al. [36] compared the benefits of various tracking systems for FPV in Italy and Germany against fixed systems. They observed that the southern location (Italy) exhibited higher gains than the northern location (Germany). For example, in the single vertical-axis configuration, the tracking gain was 23.7% in Germany and 25.5% in Italy. Overall, among the configurations analyzed, the single horizontal-axis (E–W) system showed the lowest gain, followed by the single horizontal-axis (N–S), and then the single vertical-axis, while the dual-axis system achieved the highest performance. Similarly, in India (Ambazari Lake, Nagpur), Gurfude et al. [47] reported that a single horizontal-axis (N-S) tracking system increased FPV generation efficiency by 17.7%, whereas a dual-axis system increased it by 26.2% compared to a fixed system. Research in the Netherlands by Ziar et al. [37] demonstrated that a single horizontal-axis tracking system improved the FPV efficiency by 12.1% relative to a fixed system.

Table 2.1: Various studies on the gain of tracking FPV system compared to fixed FPV system.

	Germany [36] Aar Dam Lahn-Dill district	Italy [36] Anapo Dam Sicily	India [47] Ambazari lake Nagpur	The Netherlands [37] Water pond Weurt
Single, horizontal axis	7.6% (E-W) 15.9% (N-S)	9.0% (E-W) 19.0% (N-S)	17.7% (N-S)	12.1%
Single, vertical axis	23.7%	25.5%	-	-
Dual axis	37.9%	40.8%	26.2%	-

These results indicate that implementing tracking systems for FPV is beneficial. The extent of the gain depends on the type of tracking and the site's location, but in all cases, tracking consistently enhances system performance. Having discussed the FPV technologies and design choices, the next section focuses on the criteria that determine site suitability.

2.2. Site suitability criteria

A comprehensive review of 36 FPV siting studies worldwide identified a total of 118 criteria relevant for site selection [48]. While specific considerations varied across studies, common patterns emerged. The criteria were categorized into exclusion factors, which exclude the unsuitable locations from being considered, and ranking factors, which assign scores to prioritize certain variables such as solar irradiation, wind speed, water characteristics, and distance to the transmission grid. Among the exclusion criteria, techno-economic constraints accounted for 72.11%, environmental constraints for 19.23%, and social constraints for 8.65%, reflecting the relative importance of technical and economic feasibility in FPV deployment.

2.2.1. Exclusion Criteria

Techno-economic criteria included waterbody function, depth, surface area, solar resources, terrain slope, ports/shipping routes, distance to roads and grid, airports, wind speed, and oil and gas exploration areas. Environmental criteria included protected areas and buffers, and social criteria addressed historical, cultural, and tourism sites.

Within the techno-economic category, the waterbody function emerged as the most frequently considered factor. For instance, Ghose et al. [49] focused on the five largest dams in India, excluding all other

waterbody functions. In contrast, Muñoz-Cerna et al. [50] conducted a study in Spain that excluded dams and reservoirs, concentrating instead on artificial water infrastructures such as agricultural irrigation systems. Many other studies applied filters based on their targeted waterbody types.
Another common techno-economic factor was water surface area. Some studies identified waterbodies smaller than *0.004* km^2 as unsuitable [51], whereas others set higher thresholds, excluding sites smaller than *1* km^2 [52]. Water depth was also a critical parameter. For example, [51] excluded reservoir with water depths below *2 m*, while [53] excluded those shallower than *3 m*, and a study on the complementarity of offshore wind and solar in Brazil [54] excluded areas with water depths greater than *1000 m*. Overall, the waterbody must not be too shallow or excessively deep, and its surface area should be sufficiently large, though specific thresholds varied among studies.
Regarding environmental criteria, protected areas represented the most significant exclusion factor, appearing in 14 studies. Some researches also introduced minimum buffer distances from protected areas: *0.5 km* in [55] and *2 km* in [56] and [57].
Finally, social criteria concerned the presence of historical, cultural, and tourism heritage sites [58], [53]. Table 2.2 summarizes the site exclusion criteria and provides thresholds reported in various studies.

Table 2.2: Site exclusion criteria and thresholds for unsuitable areas.

Exclusion Criteria	**Unsuitable Areas / Thresholds**
Protected areas	Occupied areas [49, 51, 53–64]
Distance to protected areas	<0.5 km [55], <1 km [59], <2 km [56, 57]
Sites of Community Interest (SIC)	<2 km [56]
Residential and other built-up regions	Occupied areas [58]
Historical, cultural, and tourism heritage sites	Occupied areas [53, 58], Indigenous lands [63]
Drinking water areas	Occupied areas [53]
Distance to inhabited areas	<500 m [60]
Areas of high landscape value	Occupied areas [53]
Archaeological areas	<2 km [56]
Wind speed [1]	<7 m/s [54]
Waterbody surface boundary change	The waterbody shrinks to less than 70% of its actual capacity [65]
Waterbody function	[49–51, 55, 58, 61, 63, 66–69]
Water surface area	<0.004 km^2 [51, 55, 69], <0.3 km^2 [59], <0.5 km^2 [65], <0.9 km^2 [68], <1 km^2 [52], >7 km^2 [59]
Water depth	>100 m [59], >1000 m [54] <2 m [51, 69], <3 m [53], <5 m [67]
Daily Solar irradiation	<3.5 kWh/m^2 [53], <4 kWh/m^2 [58], <4.5 kWh/m^2 [57]
Terrain Slope	>5°[60], >3% [58], >30% [64]
Ports and Shipping Routes	<1 km buffer from sea route, >100 km from deep water ports, and > 50 km from small piers [59] Cabotage lines [54], Port areas [53]
Oil and gas exploration blocks	Occupied areas [54], <0.5 km [57]
Gross head [2]	<100 m, >800 m [60]
Volume water body [3]	<1,000,000 m^3 [60]
Military exercise areas	Occupied areas [53, 59]
Length-height ratio [4]	> 20 [60]
Extreme weather	[53]
Distance to roads and railways	<200 m [60], >50 km [62]
Distance to grid	<100 m [57], <250 m [53], >10 km [55], >80 km [69]

[1]Related to combination of solar and wind power offshore
[2]Related to hydropower: Total vertical distance between upstream reservoir and downstream waterlevel
[3]Related to hydropower
[4]Related to Pumped Hydro Energy Storage

Exclusion Criteria	Unsuitable Areas / Thresholds
Distance from shore [5]	<10 km [59], <18 km [54]
Distance from gravel grounds	<2 km [57]
Capacity factor	<0.14 [55]
Areas where Offshore Renewable Energy Projects have been installed or plan to be installed	Occupied areas [59]
Areas to be licensed for Exploration and Exploitation of Hydrocarbons	Occupied areas [59]
Aquaculture zones	Occupied areas [59]
Airports[6]	Occupied areas [58], <2.5 km [53, 57]

2.2.2. Ranking criteria

Several researchers employ multiple-criteria decision analysis (MCDA) to assign different weights to evaluation criteria, thereby reflecting their relative importance. In a review paper by Forester et al. [48] on siting considerations for FPV systems, which analyzed 36 studies, the most significant criteria used in MCDA were predominantly techno-economic factors. These included solar resources or annual sun hours (20 studies), distance to transmission lines (13 studies), wind speed (8 studies), water surface area (7 studies), water depth (6 studies), and terrain elevation (6 studies). Among these, solar radiation was identified as one of the most influential factors. Areas with higher levels of solar radiation generally received higher suitability scores than those with lower radiation. For instance, Bhanja et al. [58] found that regions with solar radiation exceeding 12 kWh/m^2/day were deemed most suitable for FPV installation. Similarly, Korkmaz et al. [72] considered three natural factors (solar irradiation, wind speed, and wind-driven water waves) when determining suitable FPV deployment sites. Their study employed a fuzzy logic model to identify areas with optimal environmental conditions for installation. As all site selection criteria are context-specific, it is essential to identify which factors are most relevant for the Netherlands to determine the most suitable areas for FPV deployment.

2.3. Energy yield assessment methods

Different methodologies have been reported in the literature to estimate the energy yield (EY) of PV and FPV systems. These approaches vary in complexity, ranging from simplified methods based on a constant performance ratio (PR) to advanced simulation tools, data-driven models, and physics-based thermal analyses. In general, three main categories can be distinguished: (i) empirical methods using performance ratios, (ii) simulation-based approaches such as PVsyst, and (iii) data-driven or machine learning models. In addition, several studies focus on improving accuracy by incorporating specific FPV factors such as thermal behavior, environmental conditions, and wave-induced effects.

2.3.1. Empirical methods

Gómez-Gil et al. [73] used weather data and a constant performance ratio (PR). The authors reported an overestimation of the energy production and recommend determining the performance ratio separately for each PV configuration to enable a reliable assessment of energy production capability.

2.3.2. Machine Learning approaches

Another study [74] proposed a hierarchical machine learning framework for forecasting the power output of FPV systems. The input variables included the meteorological variables: (1) transient horizontal irradiance (W/m^2), (2) daily horizontal irradiance (Wh/m^2), (3) ambient temperature (°C), and (4) PV module temperature (°C). In addition, electrical characteristics of the FPV system were incorporated. The results indicated that the feedforward neural network (FFN) outperformed the other machine learning models, significantly improving the accuracy of FPV power output forecasting.

[5] Related to OPV

[6] There is no minimal distance to prevent glare[70]; some precautions could be taken to prevent glare, e.g., using glass with an antireflective coating for PV modules, or moving the panels' orientation and/or altering their tilt[71]

2.3.3. Simulation based approaches

Many studies use PVsyst software to simulate the energy produced by FPV. For instance, Oliveira-Pinto et al. [10] assessed the potential of different FPV technologies by estimating the energy yield of those systems in PVsyst. Parameters such as albedo, cooling effect, mismatch losses, and soiling losses were adjusted to resemble the FPV system. Similarly, another study [75] focused specifically on calculating and adapting thermal transmittance (U-values) for PVsyst simulations. The adjusted parameter values, compared with default values, are summarized in Table 2.3. For clarity, the following terms are used in the table:

- Albedo: The proportion of incident light or radiation reflected by a surface, typically that of a planet or moon.
- U-value: Thermal transmittance, representing the rate of heat transfer through a material or building element.
- Mismatch losses: The amount of power lost in the system due to imperfect matching of components; equivalently, the additional power that could be gained if the system were perfectly matched.
- Soiling losses: The reduction in a solar panel's power output caused by the accumulation of dirt, dust, pollen, or other particles on its surface.

Table 2.3: Adjusted parameter values in [10] compared to default PVsyst.

Parameters	Default values PVsyst	Spain, UK [10]	The Netherlands [75]
Albedo [%]	20	5	-
U-value [$\frac{W}{m^2 \cdot K}$]	29 (well-ventilated), 15 (insulated)	31 (C&T) 46 (Solaris Synergy)	open FPV: $24.4 + 6.5 \cdot ws$ closed FPV: $25.2 + 3.7 \cdot ws$
Mismatch losses [%]	1	1	-
Soiling losses [%]	2	2	-

Dörenkämper et al. [76] extended the findings of [75] by comparing modeled and measured operating temperatures of FPV modules. The analysis showed that their proposed method outperforms both PVsyst and the Sandia default models, which tend to overestimate module temperature by 2.0% and 2.2% per 1 m/s increase in wind speed, respectively.

2.3.4. FPV modeling enhancements

Vasuki et al. [16] conducted a technical review on the estimation of energy yield in OPV systems, identifying several key influencing factors, including dynamic motion, long-term degradation, cooling effects, and optical effects. Many of these factors are also relevant for inland FPV systems, where thermal behavior plays a crucial role in overall performance. Accurate modeling of FPV module temperature is therefore essential for reliable energy yield estimation.

Gurfude et al. [47] proposed a modeling approach, which incorporates water temperature and wind velocity over the water surface instead of ambient conditions over land. The FPV cell temperature (°C) is calculated using Equation 2.1, where T_{water} is the water temperature, G is the daily average irradiance (W/m^2), v_w is wind velocity (m/s).

$$T_{cell} = 0.943 T_{water} + 0.0195 G - 1.528 \cdot v_w + 0.3529 \tag{2.1}$$

In addition to the effect of temperature, the performance of FPV systems is also influenced by environmental factors. Jeong et al. [77] analyzed correlations between environmental parameters and power generation. The strongest correlation was observed with irradiation (0.98), followed by module temperature (0.64) and ambient temperature (0.25). Wind-related parameters showed weak negative correlations: wind speed (–0.06) and wind direction (–0.16). The authors found a way to calculate the power output of FPV by applying linear regression formula Equation 2.2, where T_m= module Temperature [°C], G_t = the irradiance [W/m^2].

$$P_{fpv} = T_m \times (0.0024851) + G_t \times (0.0019761) + (-0.0141039) \tag{2.2}$$

Even though the wind-related parameters showed weak correlations, still they have some impact on the performance of FPV. Starting with the wind direction, which has been studied in [43] three different tilts (0°, 10°, 20°) are examined under different wind directions, see Table 2.4.

Table 2.4: Findings of [43] on wind direction impact on diverse tilt angles of FPV.

β [°]	T_{avg} [°C]	Wind 0° [°C]	Wind 45° [°C]	Wind 90° [°C]	Wind 135° [°C]	Wind 180° [°C]
0	34.75	34.84	35.09	36.27	35.21	34.84
10	34.71	34.71	35.10	36.40	35.30	35.23
20	34.95	35.04	35.04	36.39	35.30	34.90

It can be observed that the tilt angle of 0°performs best under the wind direction of 0°and 180°. The tilt angle of 10°performs best under the wind direction of 0°. The tilt angle of 20°performs best under wind direction of 180°. Looking closer at the diverse wind directions, it can be seen that for each tilt angle the highest temperatures are found for a wind direction of 90°. There are differences for each tilt angle when they perform better than the other tilt angles under a specific wind direction:

- 0°tilt performs best between 70°-180°wind direction
- 10°tilt outperforms the other tilts under 0°wind direction
- 20°tilt performs best at wind direction of 45°

Wind velocity, in contrast, is stated to have a positive impact on the performance of the FPV [43], this is different from the negative correlation stated in [77]. In Table 2.5 the measurements are shown of the temperature of FPV cell under different wind speeds. The temperature reduces with respect to higher wind speeds.

Table 2.5: Temperature of FPV cell under different wind speed conditions from [43].

Wind speed	1 m/s	2 m/s	3 m/s	4 m/s	6 m/s	8 m/s	10 m/s
T_{cell} [°C]	42.87	38.68	36.29	34.71	32.69	31.45	30.59

In [42] a similar trend was observed: the higher the wind speed, the lower the PV cell temperature. The same study also examined the influence of the temperature difference between air and water on FPV performance. When the wind temperature was 5 °C higher than the water temperature, the FPV cell temperature T_{cell} was 1.2 °C lower than that of the NOCT PV module. When the wind temperature increased to 10 °C above the water temperature, the FPV cell temperature T_{cell} was 2.8 °C lower than that of the NOCT PV module.

2.3.5. Additional FPV losses

The other factors that could impact the FPV are wave effects. Simulations showed that the average tilt for calm days (wave height of 0-1.25m) is 0.2°, for moderate ones (wave height 1.25–2.5m) 1.8°, and for rough ones (wave height >2.5m) 4.5°. In Table 2.6 the findings have been summarized. It can be observed that rough conditions perform worse than the other conditions. For the modelled region (in the North Sea, at a latitude of 53° and a longitude of 3.85°, approximately 20 km from the coast under deep-water conditions), the average tilt due to the wave effects is 1.1°, resulting in a 0.1% decrease in yearly energy yield compared to a stationary horizontal scenario.

Table 2.6: Total efficiency of FPV under wave different conditions [78].

	Stationary	Calm	Moderate	Rough
Total efficiency [%]	96 ± 0.5	96.4 ± 0.3	96.4 ± 0.4	94.1 ± 2.1

In another research [79] wave-induced losses (WIL) for FPV systems at two latitudes (0°N and 50°N) were modeled. A seasonal difference in WIL is observed for the latitude 50°N is observed. Increasing the tilt angle from 0°to 15°reduced WIL. The greatest differences were observed in December, when WIL are at their highest.

2.4. Summary and knowledge gaps

This chapter reviewed the existing literature on floating photovoltaic (FPV) systems, focusing on system design, site suitability, and energy yield modeling approaches. FPV technology can broadly be classified into zero-air-gap and high-air-gap configurations, with the former being most relevant for inland water applications. Within these systems, design choices such as mooring configuration, module type, tilt angle, and orientation influence both structural performance and energy yield. However, there is limited consensus in the literature on optimal configurations under specific environmental conditions, particularly for inland waters in temperate climates.

Site suitability assessments in existing studies typically rely on exclusion and ranking criteria, but these vary widely between studies and lack standardization for geographically constrained regions such as the Netherlands. Similarly, energy yield modeling approaches differ in their treatment of key parameters including irradiance, wind conditions, albedo, and module temperature. These parameters introduce substantial uncertainty, and their calibration is often inconsistent across studies.

Overall, the literature highlights that FPV performance is highly dependent on both site-specific conditions and modeling assumptions. However, a unified framework that integrates spatial suitability analysis with physically based energy yield modeling for Dutch inland waters is currently lacking. This gap motivates the present study, which develops a scenario-based framework to evaluate FPV potential under Dutch conditions.

3

Available area

This chapter presents the GIS-based assessment conducted to address the first research question: *"What is the total area [km^2] of suitable inland water sites in the Netherlands for deploying Floating Photovoltaic (FPV) systems?"*. The objective is to systematically identify and quantify suitable inland water bodies in the Netherlands for FPV deployment. To achieve this, a structured and reproducible spatial analysis framework was developed and implemented.
The chapter is structured into six main components. First, the analyzed scenarios are defined. Second, the data sources used in the study are described. Third, the processing software and methodological workflow are presented. Fourth, the results of the GIS-based assessment are provided, expressed as the quantified spatial potential for FPV deployment (km^2) for each scenario. Fifth, the results are discussed. Finally, the chapter concludes by addressing the research question.

3.1. Definition of the Scenarios

The preliminary step, prior to executing the main workflow, is to define the scenarios for which suitable areas for deploying FPV systems are identified. The scenarios are distinguished based on two primary parameters: panel tilt angle and distance from the shoreline, the latter defined as the inner "buffer zone." The inclusion of this buffer zone reflects common practice [62, 80–82] and serves to reduce shading impacts from surrounding vegetation.

In **Scenario 1**, the objective is to maximize energy density. The PV tilt angle is set to $0°$, and the buffer zone is 25 m [80]. This configuration enables the highest deployment density, as a horizontal tilt eliminates the need for additional spacing to avoid inter-row shading. Moreover, the 25 m buffer represents the minimum considered distance, selected to limit shading from nearby vegetation while maximizing the available surface area.

In **Scenario 2**, both parameters are moderately increased. The buffer zone is set to 50 m [82], and the tilt angle is set to $15°$, which aligns with commonly recommended values for FPV systems [83]. In the literature, lower tilt angles of around $10°$ are often suggested for better cooling performance, while a $15°$ configuration has been reported to result in lower WIL. As a result, a compromise is adopted by selecting a $15°$ tilt, as it lies between the site-specific optimal tilt and a horizontal ($0°$) configuration. This scenario reflects a compromise between spatial efficiency and energy performance.

In **Scenario 3**, the buffer zone is further extended to 100 m [62], and the tilt angle is set to $38°$, corresponding to the optimal tilt angle for solar installations in the Netherlands. This scenario prioritizes optimal panel orientation, albeit with a reduction in usable area.

For each of these three configurations, different FPV coverage percentages of the total lake area are applied: 5%, 10%, and 15%. Combining the three configurations with the three coverage levels results in a total of nine scenarios (Table 3.1). The power density is calculated based on the selection of FPV system and the defined PV tilt angle. The FPV system is selected as 4P25S configuration as described in Section A.1. A detailed description of the power density calculation is provided in Appendix A.2. The resulting power density values are subsequently used in the Processing Software to filter the suitable deployment areas.

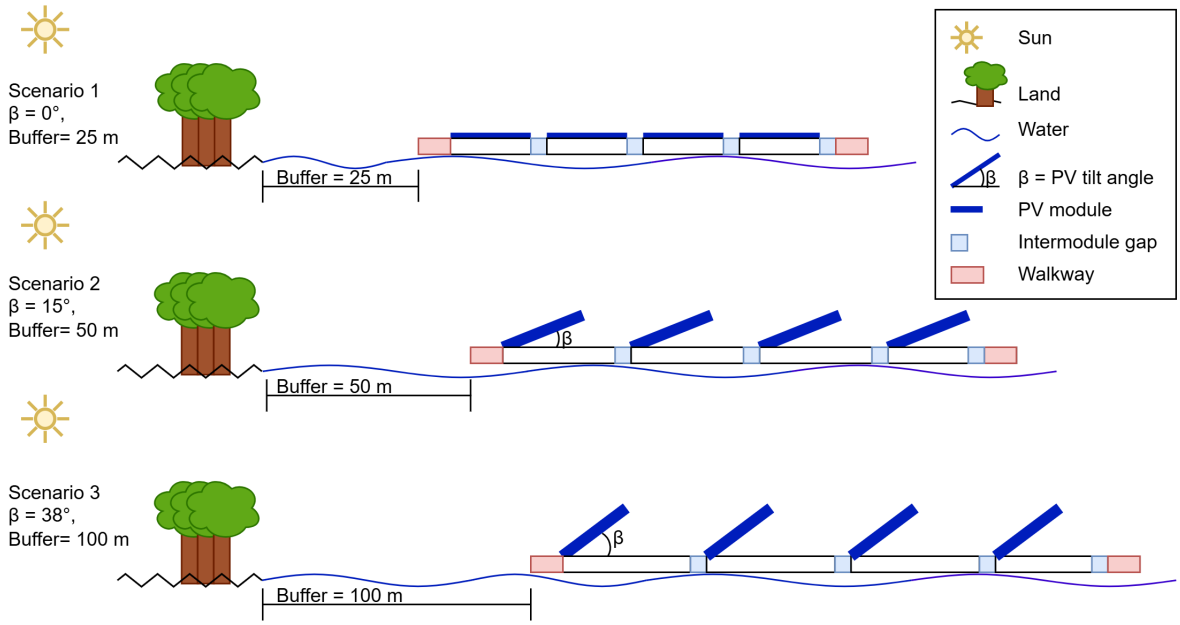

Figure 3.1: Schematic presenting the side view for Scenario 1 (0° tilt, 25 m buffer), Scenario 2 (15° tilt, 50 m buffer), Scenario 3(38° tilt, 100 m buffer)

Table 3.1: Description of the nine scenarios, combining three tilt angles and buffer zones with three FPV coverage percentages

Scenario	**Tilt angle**	**Buffer zone** [m]	**FPV coverage** [%]	**Power Density** [W/m^2]
Scenario 1.a	0°	25	5	202
Scenario 1.b	0°	25	10	202
Scenario 1.c	0°	25	15	202
Scenario 2.a	15°	50	5	117
Scenario 2.b	15°	50	10	117
Scenario 2.c	15°	50	15	117
Scenario 3.a	38°	100	5	72
Scenario 3.b	38°	100	10	72
Scenario 3.c	38°	100	15	72

3.2. Data sources

The next step involved acquiring the required data sources. In particular, national water body datasets and restricted areas needed to be compatible for GIS-based analysis. While commercial platforms such as Google Maps provide extensive geographic information, their datasets do not allow selective feature extraction or unrestricted reuse [84]. Therefore, OpenStreetMap (OSM) was selected as the primary data source, as it provides openly licensed, user-contributed geospatial data that can be queried and exported at the feature level [85]. In Overpass Turbo, OSM data was obtained through the formulation of queries to extract specific geographic features. The data could be exported in several formats, including GeoJSON, GPX, KML, and raw OSM. All formats are compatible with QGIS, which is used as the primary processing software. A comparison of the data formats, including their supported geometry types and relative file sizes for a representative query for the area of Delft is provided in Table 3.2. Given the national-scale extent of the analysis and the resulting data volume, KML is selected as the export format due to its comparatively smaller file size.

Table 3.2: Distinct data formats, query for the water body extraction for city in the Netherlands (Delft), resulting in different file sizes

Data format	Data types	File size [MB]
GeoJSON	Points, lines, polygons, multi-geometries [86]	2.5
GPX	Waypoints, tracks, routes [87]	1.315
KML	Points, lines, polygons, 3D [88]	0.867
raw OSM	Nodes, ways, relations [85]	3

National water body data and spatial layers representing restricted areas were extracted from OpenStreetMap via Overpass Turbo [89]. The criteria used to define restricted areas are outlined in Appendix A.6. The national tree height data were obtained from the RIVM dataset [90] and used to estimate potential shading lengths, which informed the shoreline buffer distance applied in the site-selection criteria. Administrative boundaries at the provincial level were obtained from the PDOK “Bestuurlijke Gebieden” dataset [91].

3.3. Processing software

After acquiring all relevant data sources, the subsequent step involved processing the data to enable efficient analysis and visualization. This is typically achieved using a Geographic Information System (GIS), such as QGIS, ArcGIS, Felt, Maptitude, Carto, MapInfo Pro, and SAGA GIS [92].

In this study, the Quantum Geographic Information System (QGIS) was used to assess the suitability of national water bodies. QGIS was selected because it is easily accessible as an open-source platform and provides excellent support for handling data obtained from Overpass Turbo. Furthermore, extensive documentation and community support are available, making it easy to apply the required methodology. In Appendix A.3 the QGIS interface is explained.

Figure 3.2 presents the workflow for obtaining the suitable areas for FPV. The python code for all the implemented steps can be found on GitLab of the TU Delft [93]. AI tools were used to assist with the preprocessing in QGIS and coding in Python. The outputs were critically reviewed and validated before inclusion.

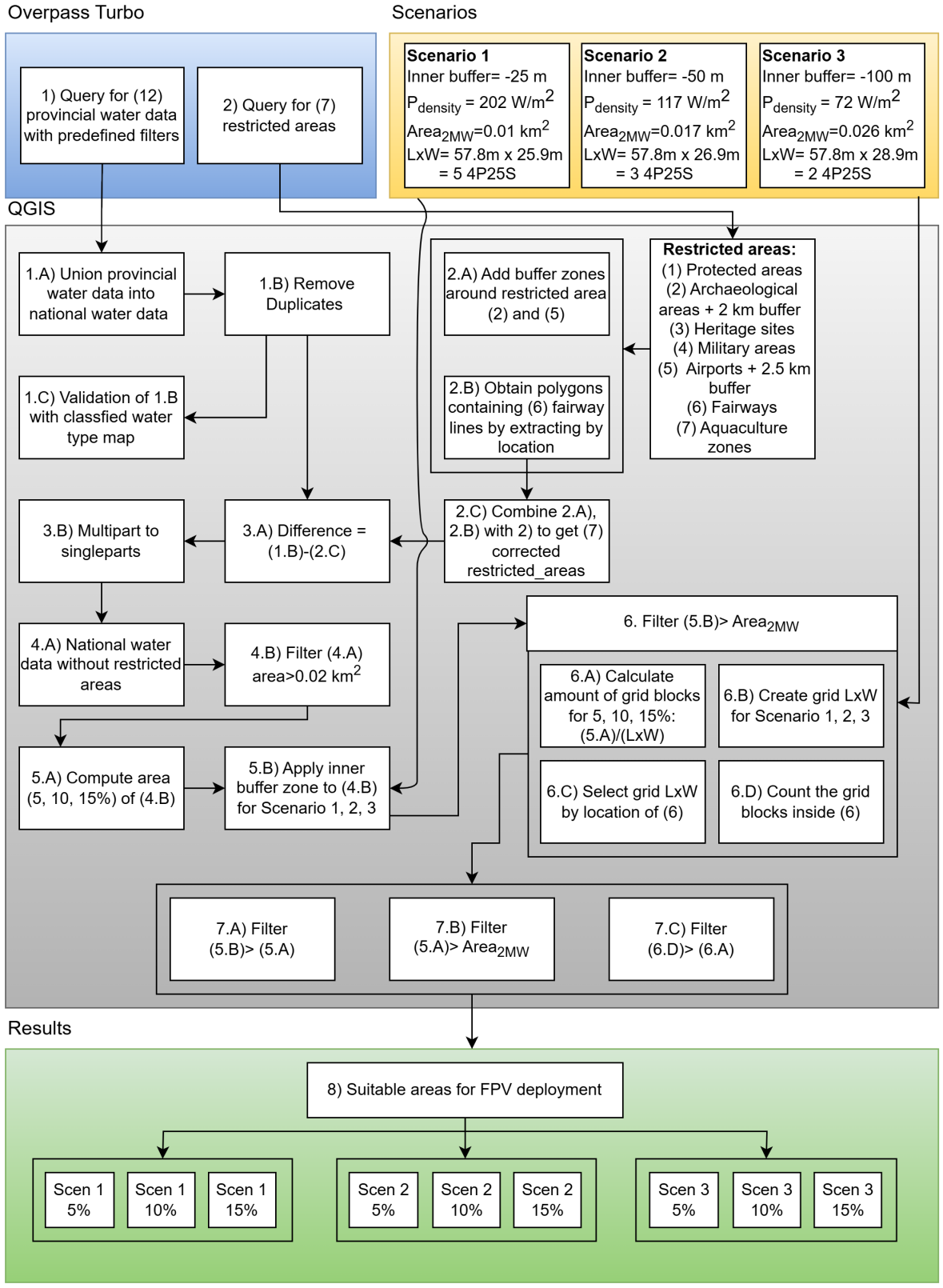

Figure 3.2: Workflow for acquiring suitable areas for FPV

Step 1: Water data

Step 1 in Figure 3.2 involves obtaining national water data from Overpass Turbo, with predefined filters applied to exclude certain water bodies. Specifically, water bodies with flow (e.g., rivers, canals, and streams), tidal areas (both intermittent and fully tidal), and waters used for transportation (e.g., shipping

lanes, harbours, and marinas) were excluded. In addition, shallow or unsuitable features such as grass-covered land areas and ditches, as well as waters designated for leisure or conservation purposes (e.g., nature reserves, playgrounds, and water parks), were removed from the dataset. For a detailed overview of the applied exclusion criteria, the Overpass Turbo query can be found in Appendix A.4.1. The data elements per province are presented in Table 3.3.

Table 3.3: Water Data by Province from Overpass Turbo Query

#	Province	Data elements
1	Groningen	13,736
2	Friesland	33,163
3	Drenthe	16,069
4	Overijssel	20,960
5	Flevoland	4,991
6	Gelderland	23,147
7	Utrecht	23,568
8	Noord-Holland	56,827
9	Zuid-Holland	56,815
10	Zeeland	8,826
11	Noord-Brabant	24,148
12	Limburg	8,526
	Total	290,776

After the data were obtained for each province, Step 1.A in Figure 3.2 was applied: the data were merged in QGIS with the Processing Toolbox *Union* function, resulting in a total of 290,776 elements. Then in Step 1.B in Figure 3.2 duplicates were removed with *Remove duplicates by geometry* resulting in a national water dataset with 290,207 elements.

To assess the reliability of the filtered OSM dataset, a spatial validation was conducted (Step 1.C in Figure 3.2) The workflow of the validation is presented in Figure A.5. The national water dataset was compared to the Watertypenkaart 2013 [94], a national surface water type classification map, that provides a detailed classification of surface water bodies and was used to verify the spatial consistency of the filtered OSM water features and to identify their corresponding water types (see Appendix **??**). The spatial overlapping reveals that although only 34.5% of the OSM features demonstrate full spatial agreement with the Watertypenkaart 2013, they accounted for 87.8% of the total OSM water area. The dataset is considered sufficiently reliable for large-scale FPV potential assessment.

Step 2: Restricted areas

Following validation, additional spatial constraints were applied to exclude legally and environmentally restricted areas (Step 2 in Figure 3.2). These included: (1) protected areas, (2) archaeological areas with a 2 km buffer zone, (3) heritage sites, (4) military areas, (5) airports with a 2.5 km buffer zone, (6) fairways, and (7) aquaculture zones. The corresponding Overpass Turbo queries are provided in Appendix A.4.2. In Step 2.A in Figure 3.2 buffer zones for archaeological areas (2.5 km) and airports (2 km) were generated using the *Processing Toolbox – Buffer function*. The restricted polygon layers were subsequently removed from the national water dataset using *Vector Overlay – Difference (multiple)*.

Since fairways were represented as line geometries rather than polygons, a different procedure was applied. In Step 2.B in Figure 3.2 the *Vector Selection – Extract by Location* tool was used to identify water bodies intersecting with fairway routes.

In Step 2.C in Figure 3.2 the restricted corrected restricted areas from Step 2.A and 2.B were combined with the other restricted areas: (1), (3), (4), (7) to obtain 7 correct restricted areas.

Step 3: Removal of restricted areas

In Step 3.A in Figure 3.2 the restricted polygon layers from Step 2.C were subsequently removed from the national water dataset in Step 1.B Figure 3.2 using *Vector Overlay – Difference (multiple)*. This resulted in 245,155 elements remained. To ensure that each water body was represented as an individual feature, multipart geometries were converted to singlepart geometries in Step 3.B using *Vector Geometry – Multipart to Singleparts*. This step increased the water data in the final dataset, resulting in 4.A) National water data without restricted areas (249,610 elements).

Step 4: Area filter

In Step 4.A the national water data without restricted areas contained 249,610 elements. The application of an area filter would decrease the size of the elements significantly, what would help to speed up the process and access the water data elements with ease. In the literature, FPV suitability assessments typically impose a minimum water body size. However, the selected thresholds vary considerably, ranging from less than 0.004 km^2 [51, 55, 69] to 0.3 km^2 [59], 0.5 km^2 [65], 0.9 km^2 [68], 1 km^2 [52], and even more than 7 km^2 [59]. This broad range demonstrates the absence of a consistent, universally applicable minimum size criterion.

Instead of defining a fixed minimum water body area, this study adopts a coverage-based economical approach. The minimum viable installed FPV capacity must be placed on 5, 10, 15% of the water body area for the different scenarios. In this study, a minimum size of $2MW_p$ is chosen and with Equation 3.1 the area required was calculated. In this equation the $x\%$ stands for the selected FPV coverage percentage: 5, 10, 15%, and the $P_{denstiy}$ stands for the power density of the different scenarios. The resulting required area for the installation of $2MW_p$ is given in Table 3.4

$$Area_{2MW_p - x\%} = \frac{2MW_p}{P_{density}} \times \frac{1}{x\%} \tag{3.1}$$

Table 3.4: Power density and required area [km^2] per scenario to achieve 2 MW$_p$ capacity at different FPV coverage levels.

		Required area [km^2]		
Scenario	**P$_{density}$ [W/m^2]**	**5%**	**10%**	**15%**
Scenario 1	202	0.20	0.10	0.07
Scenario 2	117	0.34	0.17	0.11
Scenario 3	72.4	0.55	0.28	0.18

Since all cases in Table 3.4 exceed 0.02 km^2, this value was a suitable initial filter. The area of the water bodies was computed by creating a new attribute with the Field Calculator (`Area_4.A=$area`) with the Field Calculator. Then this area was filtered in Step 4.B in Figure 3.2 with the expression: `Area_4.A>20,000[`m^2`]`. This resulted in a huge reduction of water data elements, the remaining elements were 4,765 (instead of 249,610). This reduction in the data size facilitated the further acquiring of suitable FPV areas. Table 3.5 shows the provincial distribution of the water data elements.

Table 3.5: Inland Water Bodies by Province after Step 4.B

#	Province	Data elements
1	Groningen	306
2	Friesland	530
3	Drenthe	310
4	Overijssel	413
5	Flevoland	220
6	Gelderland	366
7	Utrecht	177
8	Noord-Holland	748
9	Zuid-Holland	821
10	Zeeland	202
11	Noord-Brabant	519
12	Limburg	153
	Total	4,765

Step 5: Computing FPV coverage percentages and inner buffer zones

As was discussed in Step 4., in this study a coverage-based economical approach was applied. In Step 5.A (Figure 3.2) the coverage percentages were calculated from the remaining 4,765 elements in Step 4.B. Three coverage percentages x=5, 10, 15% were calculated in Equation 3.2.

$$A_x = x\% \cdot 100 \cdot Area\_4.B \tag{3.2}$$

In Step 5.B (Figure 3.2)) inner buffer zones were computed for the three scenarios to isolate the core study areas. Unlike a traditional expansion buffer, an inner buffer represents a reduction of spatial extent via an inward boundary offset. Using the *Processing Toolbox – Buffer function*, negative distances were applied for Scenario 1 (-25 m), Scenario 2 (-50 m), and Scenario 3 (-100 m), resulting in three distinct layers that exclude the outer perimeters of the original sites. An example of an inner buffer of -25 m for Scenario 1 `(Buffer_Scen1 (-25 m)` applied to a location in Delft (Delftse Hout) is shown in Figure 3.3 on the next page.

Step 6: Determining the number of grid blocks

The next step involves computing the number of FPV panels for each scenario. The initial step (Step 6; Figure 3.2) consisted of filtering the inner buffer zone obtained in Step 5.B to accommodate the 2 MW area (`Area_5.B > Area_2MW`). This was achieved by calculating the remaining area of the buffer zone (`Area_Buffer = $area`) and selecting the 2 MW area according to each scenario's power density (Table 3.4). Applying the formula $Area_{2MW} = \frac{2\text{ MW}}{P_{density}}$ yields different required areas per scenario: Scenario 1: 0.01 km^2; Scenario 2: 0.017 km^2; Scenario 3: 0.026 km^2. Consequently, the scenarios produced different outcomes: Scenario 1 yielded 1,540 elements, Scenario 2 yielded 642 elements, and Scenario 3 yielded 250 elements.

In Step 6.A (Figure 3.2), the number of grid blocks corresponding to the coverage percentages per scenario was calculated by dividing the coverage area by the grid block area and applying a floor function: `floor(`$\frac{Area_x}{(L\times W)_{Scenario}}$`)`. The grid blocks were based on the dimensions of the FPV system, as described in Appendix A.1; these values are summarized in Table 3.6.

Table 3.6: Dimensions of FPV system per Scenario

	Scenario 1	**Scenario 2**	**Scenario 3**
L_{panel} [m]	2.31	2.31	2.31
L_{mod} [m]	57.8	57.8	57.8
W_{panel} [m]	1.3	2.24	3.61
W_{mod} [m]	5.18	8.95	14.45
N_{4P25S} [-]	5	3	2
$L \times W$ [m^2]	57.8 x 25.9	57.8 x 26.9	57.8 x 28.9

In Step 6.B (Figure 3.2), rectangles with size $L \times W$ were generated in QGIS using the *Create Grid* tool in the Processing Toolbox. The dimensions selected correspond to those defined for each scenario. A value larger than a single block dimension was adopted, denoted as $L_{mod} \times W_{mod}$. Direct computation of this in QGIS proved infeasible due to the small magnitude of W_{mod}. Therefore, an approximation was employed using half of L_{mod}. Although this resulted in slight variations across scenarios, the values remained comparable. Specifically, Scenario 1 uses $L \times W = 57.8 \times 25.9$, resulting in five FPV blocks of 4P25S; Scenario 2 uses 57.8×26.9, resulting in three 4P25S blocks; and Scenario 3 uses 57.8×28.9, resulting in two 4P25S blocks. This process generated a grid covering the entire country.

In Step 6.C (Figure 3.2), the $L \times W$ rectangles located within the water body areas identified in Step 6 were selected using the *Select by Location* tool in the Processing Toolbox. This resulted in rectangles within the inner buffer zone (R_buffer). An example of a water body with rectangles is shown in Figure 3.3. The rectangles that didn't fit entirely inside the inner buffer zone were excluded. The selected features were then exported to a new GeoPackage file to reduce file size.

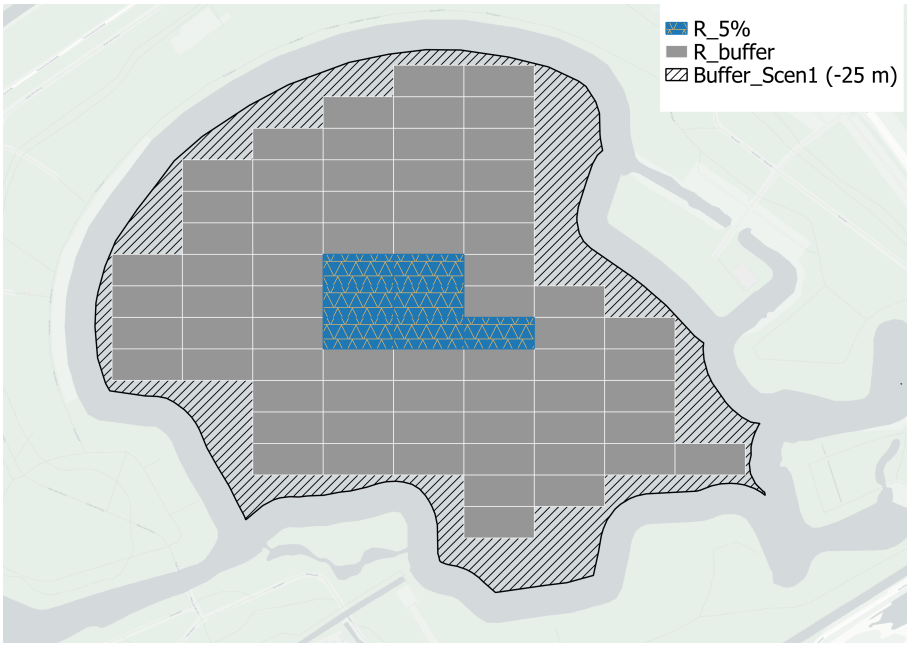

Figure 3.3: Example of the water body *Delftse Hout* suitable for Scenario 1, showing the inner buffer zone (−25 m), the rectangles fully contained within the buffer zone (R_buffer), and the number of rectangles corresponding to 5% coverage (R_5%).

In Step 6.D (Figure 3.2), the number of rectangles (R_buffer) with dimension $L \times W$ from Table 3.6 within the water bodies identified in Step 6 was determined. The *Join Attributes by Location (Summary)* tool was used to count the number of grid blocks within the water polygons. The example in Figure 3.3 has a grid block count of 75 for Scenario 1.

Step 7: Final filtering

Step 7 involves the final filtering of the water bodies. First of all, in Step 7.A (Figure 3.2 the computed area of the coverage percentage 5, 10, 15% from step 5.A, should fit within the inner buffer zone of step 5.B. `Area_5.B > Area_5.A`. Secondly, the coverage percentage areas 5, 10, 15% from step 5.A should accomodate the required area for 2 MW capacity of installed FPV. `Area_5.A > Area_2MW`, similar to the procedure of step 6. And finally, the grid blocks computed in Step 6.D should be larger than amount of grid blocks for the coverage percentages. `6.D_blocks > 6.A_blocks .`

As an illustrative example, Delftse Hout (Figure 3.3) has a total area of 0.212 km^2. The inner buffer zone (-25 m) has a total area of 0.152 km^2. A 5% coverage of the total area of the water body corresponds to 0.011 km^2, which can accommodate seven grid blocks ($\frac{0.011 \cdot 10^6}{57.8 \times 25.9} = 7$), shown as $R\_5\%$ in Figure 3.3.

This area is considered suitable because it satisfies all filtering criteria: (7.A) the area of the inner buffer zone (0.152 km^2) exceeds the 5% coverage area (0.011 km^2); (7.B) the 5% coverage area (0.011 km^2) exceeds the area required for a 2 MW installation in Scenario 1 (0.01 km^2); and (7.C) the total number of panels that can be placed within the buffer zone (75) exceeds the required seven blocks. Therefore, Delftse Hout qualifies as a suitable site for Scenario 1 with a 5% coverage percentage.

Step 8: Results

After applying the filters of Step 7, the suitable areas were determined for FPV deployment, resulting in 9 geopackage files. These files contained the 'fid' (Feature ID), 'x' (latitude) 'y' (longitude) coordinates, the area of the coverage scenario, the amount of rectangles per coverage scenario. The geopackage layer was exported in a csv file, to further process the amount of area. The allocated surface area is based on the number of rectangles for a x coverage percentage ($R_{x\%}$), and the dimensions of the rectangle $L \times W$ defined in Table 3.6 and calculated with Equation 3.4. The effective array area depends on the number of panels and the dimensions (L_{dim}=2.278 m, W_{dim}= 1.134 m) (Equation 3.5. The number of panels is calculated with the number of rectangles $R_{x\%}$ per scenario, the scenario's configuration N_{4P25S} defined in Table 3.6 and the panels (25 by 4 is 100) within the N_{4P25S} configuration(Equation 3.3). Based on the

number of panels and the peak power the installed capacity (Equation 3.6) is calculated.

$$N_{panels,x\%} = R\_x\% \times N_{4P25S} \times 100 \tag{3.3}$$

$$A_{alloc,x\%} = R\_x\% \times L \times W \tag{3.4}$$

$$A_{array,x\%} = N_{panels,x\%} \times L_{dim} \times W_{dim} \tag{3.5}$$

$$P_{installed,x\%} = N_{panels,x\%} \times P_{peak} \tag{3.6}$$

3.4. Results

The allocated surface area (A_{alloc}) and the effective array area (A_{array}) was calculated for three surface coverage percentages (5%, 10%, and 15% of suitable water bodies). The results and the total number of elements per scenario are presented in Figure 3.8. The provincial distribution of FPV area is found by using *Join attributes by location* with the provincial layer.

Table 3.7: Potential FPV water bodies and area in the Netherlands for different scenarios, where elements is the amount of water bodies found, A_{alloc} is the allocated surface area in [km^2] and A_{array} the effective array area in [km^2].

Scenario	Coverage scenario								
	5%			10%			15%		
	Elements	A_{alloc}	A_{array}	Elements	A_{alloc}	A_{array}	Elements	A_{alloc}	A_{array}
Scenario 1	288	7.1	6.1	533	17.6	15.2	645	27.7	23.9
Scenario 2	149	5.4	2.7	297	14.3	7.1	371	22.7	11.3
Scenario 3	71	3.7	1.1	141	10.0	3.1	139	13.8	4.3

For Scenario 1 (tilt angle=0°, inner buffer=-25 m), the allocated surface area ranges from 7.1 km^2 at 5% coverage to 27.7 km^2 at 15% coverage. Scenario 2 (tilt angle=15°, inner buffer=-50 m) results in slightly lower values, ranging from 5.4 km^2 to 22.7 km^2. Scenario 3 (tilt angle=38°, inner buffer= -100 m) produces the most conservative estimates, between 3.7 km^2 and 13.8 km^2. Comparing this to the total area of inland water in the Netherlands (3744 km^2, [12]), reveals that the allocated surface area (A_{alloc}) for Scenario which uses the most area (Scenario 1, 15%) is 0.74%.

The effective array area A_{array} shows even more conservative values: with Scenario 1 ranging from 6.1 to 23.9 km^2, Scenario 2 ranging from 2.7 to 11.3 km^2, and the last scenario from 1.1 to 4.3 km^2. The large decrease in the final scenario is mainly caused by the extra required shading space. On average, the effective array area compared to A_{alloc} is reduced by 13.8% in Scenario 1, 50.2% in Scenario 2, and 69.4% in Scenario 3. Figure 3.4 visualizes the FPV potential of the allocated surface area and the effective area across scenarios.

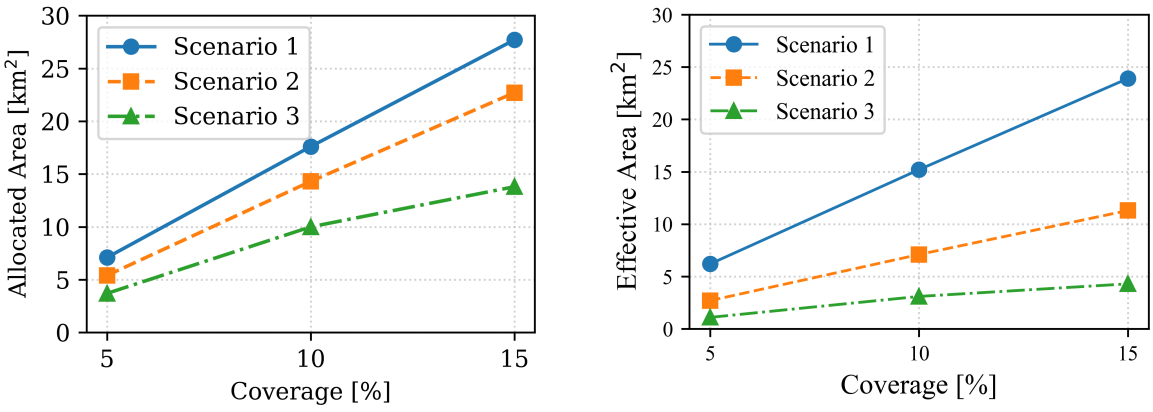

(a) The allocated surface area A_{alloc} based on the scenarios boundaries. (b) The effective array area A_{array} based on the FPV panels dimensions.

Figure 3.4: Two graph showing the allocated and effective area [km^2] for FPV deployment in the Netherlands per scenario under different coverage percentages. The effective area is decreased substantially.

It can be observed that Scenario 1 and Scenario 2 show a fairly linear increase in the allocated surface area A_{alloc} as the coverage percentage increases. Scenario 3, however, behaves differently: the increase from 5% to 10% is steeper than from 10% to 15%. This suggests that for Scenario 3 at higher coverage levels, less additional suitable area becomes available.

The FPV potential capacity is estimated in Figure 3.5. It strongly correlates to the effective array area A_{array}. The FPV capacity ranges from 0.3 to 5.6 GW_p.

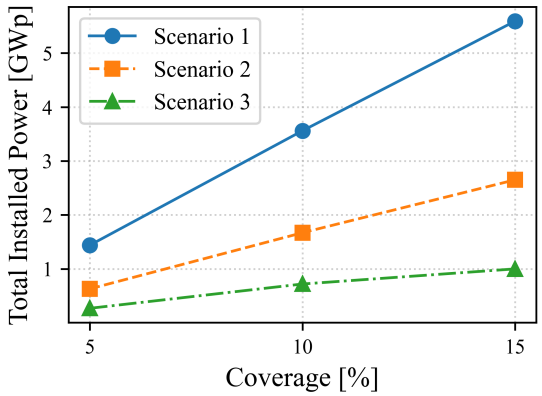

Table 3.8: FPV potential capacity for different scenarios in [GW_p].

	FPV capacity [GW_p]		
Scenario	5%	10%	15%
Scenario 1	1.4	3.6	5.6
Scenario 2	0.6	1.7	2.6
Scenario 3	0.3	0.7	1.0

Figure 3.5: FPV potential of installation capacity

The provincial distribution of the allocated surface area, A_{alloc}, reveals a distinct concentration of FPV in specific regions of the Netherlands. This trend remains consistent across all scenarios, with the exact values per province available in Appendix B.5. Figure 3.6 illustrates the provincial variation in the allocated surface area of Scenario 2 (10% coverage), showing that Zuid-Holland requires the largest FPV implementation area, accounting for 16.7% (2.4 km²) of the national total. When combined with Noord-Brabant, Gelderland, and Noord-Holland, these four provinces alone represent more than half of the total allocated surface area for the entire country.

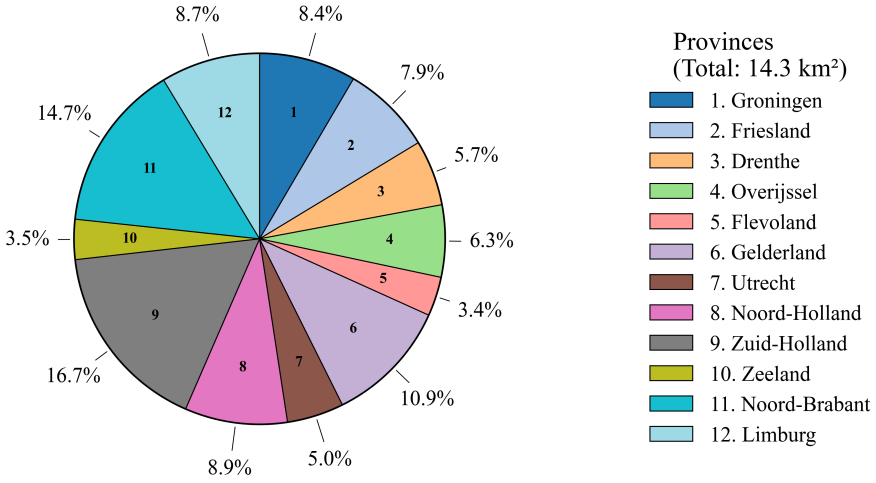

Figure 3.6: Allocated surface area A_{alloc} per province in the Netherlands for Scenario 2, 10% coverage.

3.5. Discussion

The estimated suitable area for FPV systems is subject to several spatial and technical assumptions, which introduce uncertainty into the results. In particular, the exclusion of unsuitable areas, combined with the application of a minimum area threshold, substantially reduces the available surface area, resulting in a conservative estimate of deployable capacity. While these constraints enhance the realism of the analysis, they may also exclude areas that could become viable under future policy developments or technological advancements.

The provincial distribution of the allocated surface area, A_{alloc} for Scenario 2, 10% coverage (Figure 3.6), reveals a clear spatial concentration of FPV deployment within specific regions of the Netherlands. In particular, Zuid-Holland, Noord-Brabant, Gelderland, and Noord-Holland together account for more than half of the total allocated area. This distribution is partly influenced by the initial availability of water bodies following the applied filtering steps. For instance, Zuid-Holland contains the highest number of filtered elements from Table 3.5 (821), whereas Limburg has the lowest (153). However, a higher number of water bodies does not directly translate into a larger FPV share, despite having fewer elements than Flevoland, Limburg contributes a larger proportion of FPV area (8.7% compared to 3.4%). This indicates that the suitability of water bodies depends not only on their number but also on their size and the cumulative effect of subsequent filtering criteria.

The implementation of inner buffer zones (Scenario 1: 25 m, Scenario 2: 50 m, Scenario 3: 100 m) further restricts the usable water surface. These buffers are based on common regulatory and is also aimed to reduce shading effects; however, their exact extent may vary depending on local conditions. In cases where surrounding vegetation is limited, horizon obstruction may be minimal, suggesting that the applied buffer distances could be overly conservative. Consequently, the estimated FPV potential is sensitive to the selected buffer parameters.

In addition, water bodies were classified as unsuitable if they could not accommodate a minimum FPV capacity of 2 MW_p. Allowing smaller installations would increase flexibility and enable the inclusion of areas currently excluded from the analysis. This threshold is closely linked to the assumed power density, which plays a critical role in determining capacity estimates. Variations in system design, including module type and spacing (influenced by the design solar altitude angle), can lead to significantly different power densities and, therefore, alter the minimum required deployment area. As a result, this constraint directly affects both the number of suitable water bodies and the overall FPV potential.

Furthermore, a standardized FPV configuration of 25 by 4 panels was assumed. Rectangular grid cells were generated in QGIS to accommodate this configuration, with dimensions exceeding the exact length and width to reduce computational demand. This simplification may have led to an underestimation of the achievable capacity, as smaller grid sizes could enable more efficient placement of FPV systems in areas previously classified as unsuitable.

Finally, the applied coverage percentages of water bodies strongly influence the resulting capacity estimates. Higher coverage levels allow for a greater number of FPV installations, thereby increasing the overall potential. This underscores the importance of selecting realistic and context-sensitive coverage scenarios when assessing large-scale FPV deployment.

3.6. Conclusion

Overall, the results demonstrate that the national inland water dataset was successfully refined through a series of spatial and technical filters. Unsuitable areas were excluded, a minimum area threshold capable of supporting a 2 MW_p FPV installation was applied to the FPV coverage (5, 10, 15%), inner buffer zones were incorporated, and the grid blocks per water body that represented the FPV configuration was selected to be larger than the calculated grid blocks of the FPV coverage.

As a result, the allocated surface area available for FPV deployment spans approximately 3.7 to 27.7 km^2. The effective area occupied by the panels is more conservative, at 1.1 to 23.9 km^2, corresponding to an estimated total capacity potential of 0.3–5.6 GW_p, depending on the scenario assumptions.

With these results, the first research question can be answered: the total area of suitable inland water sites in the Netherlands ranges from 7.1 to 27.7 km^2 for Scenario 1, from 5.4 to 22.7 km^2 for Scenario 2, and from 3.7 to 13.8 km^2 for Scenario 3. In the case of 27.7 km^2, this represents a small percentage of the total inland water area in the Netherlands (0.73%).

4

Energy yield

This chapter presents the modeling of the energy yield in order to address the second research question: "What is the energy yield of suitable floating photovoltaic (FPV) systems in the Netherlands [TWh]?" The main objective is to estimate the potential DC electricity generation from these systems under representative conditions. Estimating the energy yield is essential for assessing the technical potential of FPV systems in the Netherlands. For this purpose, long-term estimates based on Typical Meteorological Year (TMY) data are used to ensure representative climatic conditions.

The chapter is structured into several components. First, the analysed scenarios and underlying assumptions are defined. Second, the methodology for energy yield modeling, including the workflow, is described. Third, the results are presented and discussed. Finally, the chapter presents its conclusions, integrating the results and discussion to answer the research question.

4.1. Scenario Definition & Assumptions

The scenarios are adopted from Chapter 1. A brief summary is provided here for completeness (Table 4.1). In **Scenario 1**, the PV tilt angle is set to $0°$, and the inner buffer zone is 25 m [80]. In **Scenario 2**, the inner buffer zone is set to 50 m [82], and the tilt angle is $15°$. In **Scenario 3**, the inner buffer zone is extended to 100 m [62], and the tilt angle is set to $38°$. For every scenario, three FPV coverage percentages were obtained: 5, 10, 15%.

Table 4.1: Description of the nine scenarios, combining three tilt angles and buffer zones with three FPV coverage percentages

Scenario	**Tilt angle**	**Buffer zone** [m]	**FPV coverage** [%]	**Power Density** [W/m^2]
Scenario 1.a	$0°$	25	5	202
Scenario 1.b	$0°$	25	10	202
Scenario 1.c	$0°$	25	15	202
Scenario 2.a	$15°$	50	5	117
Scenario 2.b	$15°$	50	10	117
Scenario 2.c	$15°$	50	15	117
Scenario 3.a	$38°$	100	5	72
Scenario 3.b	$38°$	100	10	72
Scenario 3.c	$38°$	100	15	72

Additional Modeling Considerations

A solar altitude analysis was conducted to evaluate the potential shading impact of surrounding trees on FPV systems (Appendix B.1). If the FPV system is assumed to be located at the edge of the inner buffer zone, the corresponding maximum solar altitude angles for Scenario 1, Scenario 2, and Scenario 3 are $11.56°$, $6.27°$, and $3.31°$, respectively.

For Scenario 1, a refined analysis was performed to account for different FPV coverage scenarios, assuming that the system is positioned further away from the edge of the inner buffer zone. This resulted in average solar altitude angles ranging from $1.4°$ to $2.6°$. For Scenarios 2 and 3, the solar altitude angles

due to the shading impact are below the design solar altitude angle of $14.4°$ used in the power density analysis (Appendix A.2). Therefore, additional shading analysis was not considered necessary.

Since the solar altitude angles of Scenario 1 are small (below $3°$) and the exact spatial distribution of trees relative to the FPV system is uncertain, shading losses for Scenario 1 were considered negligible and therefore not included in the final analysis. However, for Scenario 2 and 3, shading losses were implemented for solar altitude angles below the design angle of $14.4°$. A limitation of this approach is the assumption of the FPV shape. Future work should consider the actual geometry of the water bodies to further refine the shading assessment.

Excluded Effects

This study limits the scope of albedo modeling, excludes wave-induced losses (WIL) and soiling. While using white pontoons (50% albedo) is known to yield higher bifacial gains than water (5–10% albedo)[95], a conservative water-only approach was taken here to maintain a realistic energy yield under uncertain interaction parameters. Finally, this study uses a constant rather than a varying albedo, acknowledging that this simplification may introduce a slight variance (approx. 1.03%) in reported system performance[96].

WIL have been reported to vary with wave height, wave period, latitude, and seasonal conditions. A model to estimate WIL was proposed in [79] (see Appendix B.2); however, this model is based on a limited dataset of only four days and assumes specific wave height and period conditions. Reliable data for these parameters in Dutch inland waters were not available. The KNMI provides wave data primarily for large inland water bodies, such as the IJsselmeer, and offshore locations, which fall outside the scope of this study. In addition, Vasuki et al. [16] demonstrated that WIL exhibit dynamic behavior on timescales of seconds rather than as steady-state losses. Given these limitations, wave-induced losses are assumed to be negligible for calm inland water bodies and are therefore set to zero.

Regarding soiling, the aquatic environment reduces dust accumulation, yet other factors persist. Bird droppings, in particular, remain a critical issue and are frequently cited as the most significant source of power loss. In hot and dry regions, deposits of 10 g and 50 g have been shown to result in power losses ranging from 31.25% to 86.53% [97]. While such losses are expected to be less severe in countries with maritime climate such as the Netherlands, it could still result in significant power losses. To mitigate soiling, maintenance walkways were incorporated into the system design in this study, facilitating the cleaning of PV panels. A recommended next step is to investigate soiling rates and evaluate the effectiveness of the selected operation and maintenance (O&M) strategy. With this information, a more accurate soiling model could be implemented; however, due to the current lack of data, soiling effects are neglected in this study.

4.2. Energy yield modeling

In the literature, several methodologies have been used to model PV energy yield. Software tools such as PVsyst have been widely applied, as demonstrated by [10] and [98]. However, a key limitation of PVsyst is that it is not open-source, which restricts transparency and flexibility in modifying underlying models. Furthermore, PVsyst relies on simplified lookup tables that approximate module behavior under different conditions. While this approach is computationally efficient, it may limit the physical fidelity of the simulations.

In contrast, the PVMD Toolbox [99] was selected in this study due to its physics-based modeling approach. Its use of ray tracing and spectral decomposition enables a more realistic representation of energy yield. Additionally, it allows flexible parameter adaptation and the incorporation of detailed, realistic input data. The DC energy yield was determined through five main components: (1) cell, (2) module, (3) weather, (4) thermal, and (5) electrical models, as is shown in Figure 4.1. The python code for all the implemented steps can be found on GitLab of the TU Delft [93].

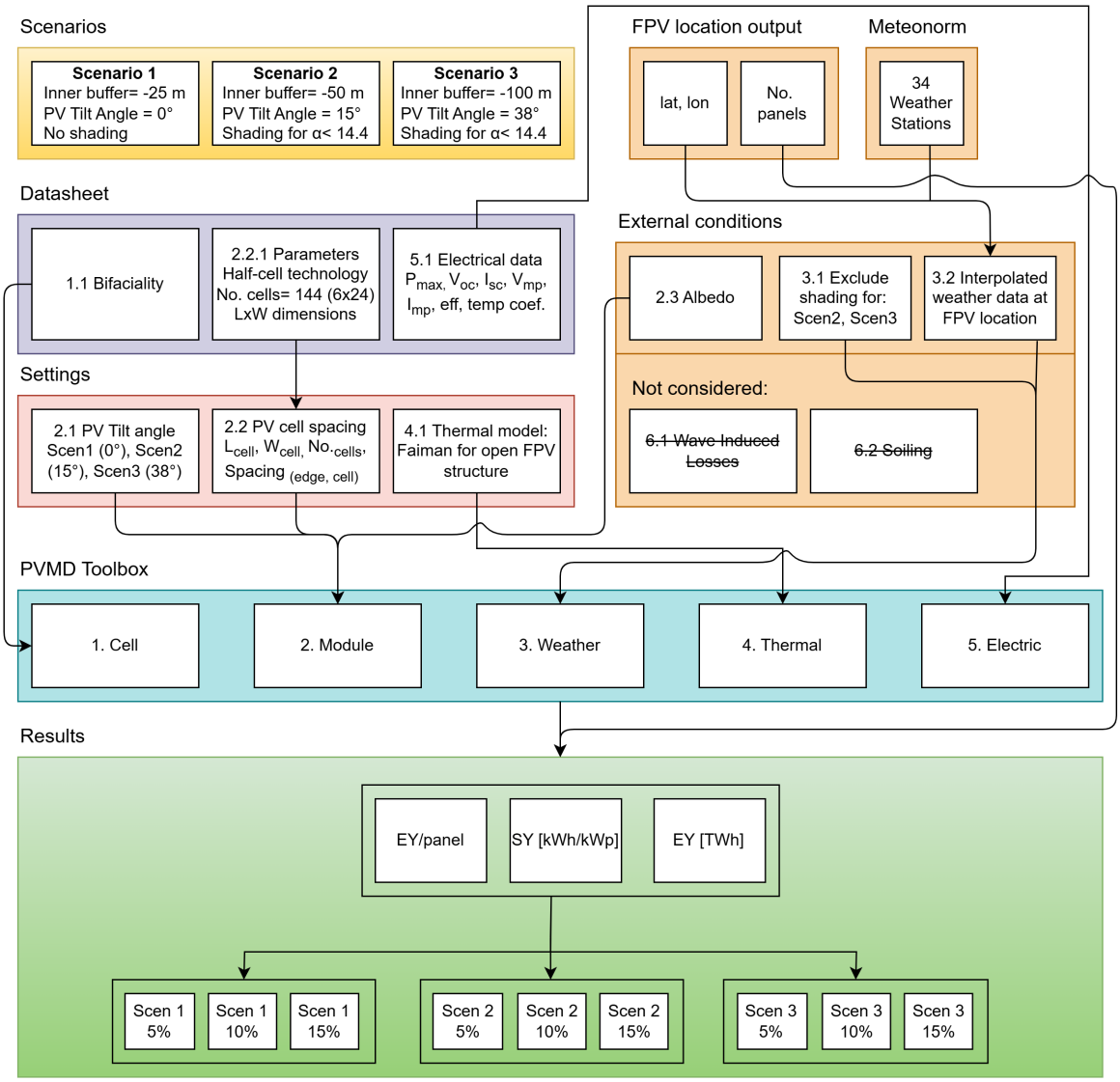

Figure 4.1: Flowchart of obtaining the energy yield

1. Cell

The first component of the PVMD Toolbox is the *Cell* module. The floating PV system considered in this study is based on the JAM72D40-605MB module by JA Solar (see Appendix A.7). This module is an n-type, double-glass bifacial design. To represent its optical behavior, a silicon heterojunction (SHJ) bifacial optical file is developed. This file characterizes the irradiance response of both the front and rear sides of the cell. The bifaciality factor (1.1, see Figure 4.1) is incorporated to account for enhanced rear-side irradiance contributions, enabling a more accurate representation of bifacial energy yield.

2. Module

The *Module* component requires several key input parameters: the PV tilt angle, PV cell spacing, and the Albedo. First, the PV tilt angle (2.1 in Figure 4.1) was defined for three scenarios: $0°$ (Scenario 1), $15°$ (Scenario 2), and $38°$ (Scenario 3). The panel orientation was set to face south (0° in the PVMD Toolbox convention). For the PV cell spacing (2.2 in Figure 4.1), the geometric layout of the module was specified, including cell dimensions, inter-cell spacing, and edge margins. These inputs were derived from estimating the dimensions from the module datasheet (2.2.1 Parameters in Figure 4.1). The datasheet indicates the use of half-cell technology. Therefore, the original full-cell dimensions were adjusted accordingly. The cell width was estimated to be 0.182 m, which is consistent with an M10 wafer [100]. Due to the half-cell configuration, the effective cell length is 0.091 m. The module layout consists of 24 columns and 6 rows of cells, resulting in a total of 144 half-cells. The space between the cells is

set to 0.3 cm, edge space to 1 cm (default settings for PVMD).

The last required input was the albedo (2.3 in Figure 4.1). The surface albedo has a significant influence on bifacial modules and correct modeling is crucial for a realistic energy yield output. In the PVMD Toolbox, a default albedo value of 20% is assumed. However, inland water surfaces typically exhibit lower albedo values, ranging from 6–10% [101]. For this study, an albedo value of 10.3% was assumed, this was the average daytime albedo for the location of De Bilt adapting a model based on [102, 103], further described in Appendix B.3. It was not possible to model the seasonal and daily variations since the PVMD Toolbox does not support time-varying albedo inputs.

The PVMD Toolbox generates a sensitivity map from Ray-tracing simulations. See Figure 4.2 for the sensitivity map of Scenario 1.

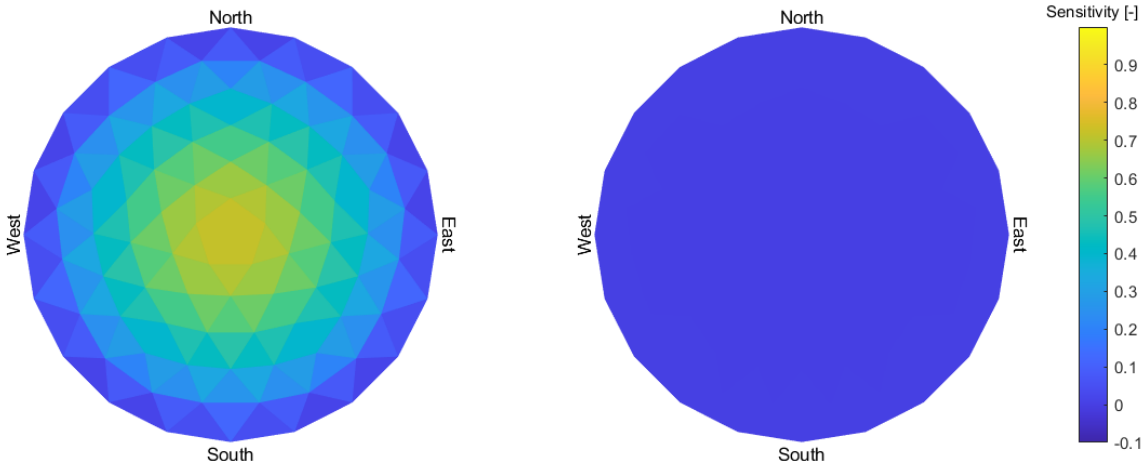

(a) Front side

(b) Rear side

Figure 4.2: Sensitivity map of Scenario 1 (0° tilt angle).

A recommended next step is to evaluate whether the modeled daytime albedo accurately represents inland water conditions in the Netherlands, to quantify the extent of temporal variation, and to explore potential methods for incorporating time-dependent albedo into the PVMD Toolbox.

3. Weather

For the *Weather* component, the meteorological variables described in Table 4.2 were required as an input for the PVMD Toolbox.

Table 4.2: Description of meteorological variables required for the PVMD toolbox

Col.	Symbol	Description	Unit
1	y	Year	–
2	m	Month	–
3	dm	Day of month	–
4	h	Hour (local time)	–
5	A_z	Solar azimuth angle	°
6	h_s	Solar altitude angle	°
7	G_{DNI}	Direct Normal Irradiance (DNI)	$\mathrm{W\,m^{-2}}$
8	G_{DHI}	Diffuse Horizontal Irradiance (DHI)	$\mathrm{W\,m^{-2}}$
9	T_a	Ambient air temperature (at 2 m height)	°C
10	v_w	Wind speed	$\mathrm{m\,s^{-1}}$
11	G_{GHI}	Global Horizontal Irradiance (GHI)	$\mathrm{W\,m^{-2}}$

Two meteorological data sources were evaluated to obtain the required inputs for Table 4.2: (1) KNMI weather station data, (2) Meteonorm version 7.2. In Appendix B.4.1 an extensive comparison

was performed. It was revealed that although the distribution of weather stations was more favorable in the KNMI dataset, two key drawbacks were identified: not all stations provided the required inputs for the PVMD Toolbox, and the KNMI data were available only in Actual Meteorological Years (AMY). Meteonorm version 7.2, by contrast, provided all required inputs for the PVMD Toolbox and supplied data in Typical Meteorological Years (TMY). TMY data are preferred in this study, as they enable the estimation of long-term average energy yields of floating photovoltaic (FPV) systems. Therefore, Meteonorm data were selected.

Because the selected FPV sites are geographically dispersed, additional modeling was required for several variables. The variables (1) y, (2) m, (3) dm, and (4) h were used directly from the dataset without modification. Variables (5) A_z and (6) h_s were derived using `pvlib` calculations (Appendix B.4.2). Variable (7) G_{DNI} was corrected and then interpolated with the inverse distance weighting (IDW) interpolation, as were variables (8) G_{DHI}, (9) T_a, (10) v_w, and (11) G_{GHI} (see Appendix B.4.3). Leave-one-out cross-validation (LOOCV) was performed, and the root mean square error (RMSE) statistics for these variables are presented in Table B.6. In the Appendix, Figure B.4 and Figure B.6 illustrate the performance of the station with an RMSE closest to the mean RMSE.

Table 4.3: RMSE statistics for LOOCV for 36 datapoints for the variables using pvlib and IDW interpolation

Statistic	A_z [°]	h_s [°]	G_{GHI}[W/m^2]	$G_{DNI-cor}$ [W/m^2]	T_a [°C]	v_w [m/s]	G_{GHI} [W/m^2]
Mean RMSE	0.3109	0.1827	277.30	73.24	3.39	0.75	172.85

The final modification in the *Weather part* concerns the treatment of horizon effects. Horizon reconstruction was not applied; instead, depending on the scenario, irradiation data were set to zero for solar altitude angles below $14.4°$. As defined in Section 4.1, Scenario 1 was not capped, whereas Scenarios 2 and 3 were subject to this limitation. The Simple Model of the Atmospheric Radiative Transfer of Sunshine (SMARTS) model, which assumes clear-sky conditions, was selected for this study because the Meteonorm irradiation data already account for cloud effects.

4. Thermal

Within `ThermalPart`, the thermal behavior is modeled using the Faiman model (Equation 4.1). For floating PV systems with an open structure in the Netherlands, literature reports coefficients of $U_0 = 24.4$ and $U_1 = 6.5$ [23]. As no alternative thermal models for comparable FPV configurations were identified, this model was adopted. The absorptance is set to $\alpha_0 = 0.9$, which corresponds to the default value in PVMD and is representative of crystalline silicon modules.

$$T_m = T_a + \frac{\alpha_0 \cdot G_{poa}}{U_0 + U_1 \cdot v_w} \tag{4.1}$$

5. Electric

Within `ElectricalPart`, electrical parameters such as V_{OC}, V_{mpp}, I_{sc}, and I_{mpp}, as well as the temperature coefficients, were obtained from the datasheet. As these values already account for metallization effects, additional modeling of busbar metallization losses was not included. The `Butterfly` module configuration with three bypass diodes was selected. This configuration yields a nominal power output of $P_{STC} = 605$ W, which is consistent with the datasheet specification.

Simulations

The simulations in the PVMD Toolbox were performed using the Delft Blue supercomputer [104]. The `Electric.OUTPUT` variable was stored for analysis, providing the energy yield of a single module, denoted as EY_{sim}. The total energy yield for a water body was then calculated using Equation 4.2. Subsequently, Equation 4.3 was applied to determine the total scenario yield, and Equation 4.4 to compute the specific yield.

$$EY_{water\_body} = EY_{sim} \cdot N_{panels} \tag{4.2}$$

$$EY_{Scenario} = \sum EY_{water\_body}[TWh] \tag{4.3}$$

$$SY_{Scenario} = \sum \frac{EY_{water\_body}}{P_{water\_body}}[kWh/kW_p] \tag{4.4}$$

The water bodies were linked to their corresponding element IDs and associated FIDs (feature IDs from QGIS). The element ID was primarily used to link the QGIS output to the PVMD Toolbox. The outputs generated by the PVMD Toolbox were labeled using the corresponding element IDs, allowing them to be directly associated with the original elements for further analysis. To analyze the spatial variability of suitable floating photovoltaic (FPV) locations, the CSV layer was first added to QGIS and connected to the original dataset using the corresponding FID. In the Properties panel under Joins, a join was performed based on matching FIDs, which allowed the specific yield values to be added as a new column in the attribute table. Subsequently, an IDW interpolation was carried out, using the provincial boundary layer as an overlay, with a pixel resolution of 10,000 by 10,000.

4.3. Results

The energy yield (EY) and specific yield (SY) for the nine scenarios are summarized in Table 4.4. It can be observed that, although the total energy yield is highest for Scenario 1, its specific yield is significantly lower compared to the other scenarios.

Table 4.4: Energy yield of FPV system for distinct scenarios, where EY is the total energy yield in TWh, SY is the specific yield in kWh/kWp, with SY_μ representing the mean value, and SY Range the range across water bodies.

Scenario	Coverage scenario								
	5%			10%			15%		
	EY	SY_μ	SY Range	EY	SY_μ	SY Range	EY	SY_μ	SY Range
Scenario 1	1.3	859	814-924	3.1	859	814-930	4.8	858	814-929
Scenario 2	0.6	918	866-992	1.5	914	866-992	2.4	914	866-992
Scenario 3	0.3	1047	1005-1124	0.8	1042	981-1124	1.0	1041	981-1124

Figure 4.3a presents the total energy yield per scenario. Scenario 1 (blue line) results in the highest energy output, ranging from approximately 1.3 TWh to 4.9 TWh. Scenario 2 (orange line) has an energy yield output ranging from 0.6 TWh to 2.5 TWh. In contrast, Scenario 3 (green line) requires larger spacing between panels, resulting in fewer installed panels and therefore lower total yield, ranging from approximately 0.3 TWh to 1.0 TWh. Figure 4.3b shows that the mean specific yield remains nearly constant for each scenario and is not influenced by the percentage. Scenario 1 yields approximately 860 kWh/kW$_p$, Scenario 2 around 915 kWh/kW$_p$, and Scenario 3 about 1045 kWh/kW$_p$.

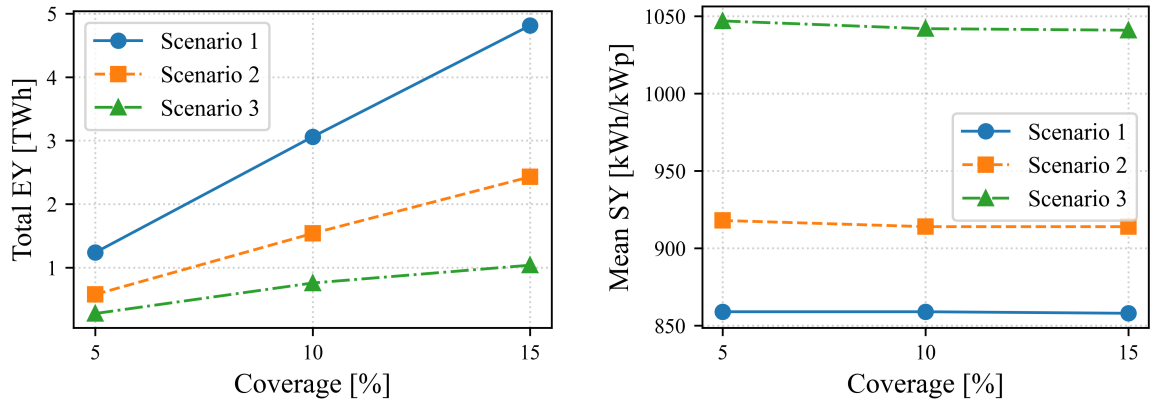

(a) Total energy yield per scenario

(b) Specific yield per scenario

Figure 4.3: Energy yield results

In Appendix B.6 the spatial variation across the country for the three Scenarios are visualized for a range from 810-1130 kWh/kWp, showing that Scenario 3 performs best. Using a smaller range of Scenario 2, 15% coverage (866-992 kWh/kWp) reveals the spatial variability of the Specific yield better, see Figure 4.4. The best results in mean Specific yield is found to be 968.2 in the province Zeeland, And the lowest SY_μ is found in the province Groningen of 892.9.

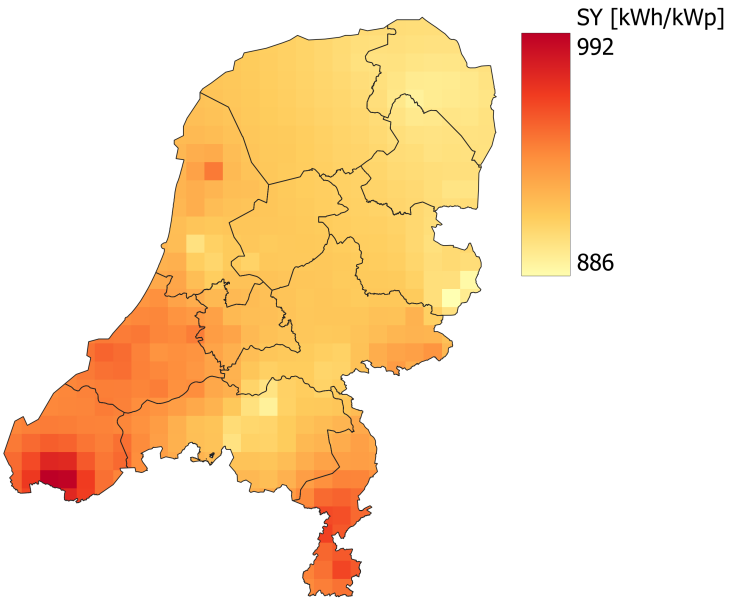

Figure 4.4: Spatial variability for Specific yield for Scenario 2 at 15 % FPV coverage

The monthly variation in specific yield for a single water body, illustrated in Figure 4.5, provides more insights into performance trends. Scenarios 2 and 3 exhibit better specific yields despite the irradiation losses below the 14.4° solar altitude threshold. It was observed that, except the winter months: Scenario 3 achieves the highest monthly specific yield for most of the year, Scenario 2 demonstrates a moderate increase in yield, while Scenario 1 consistently produces the lowest monthly specific yield.

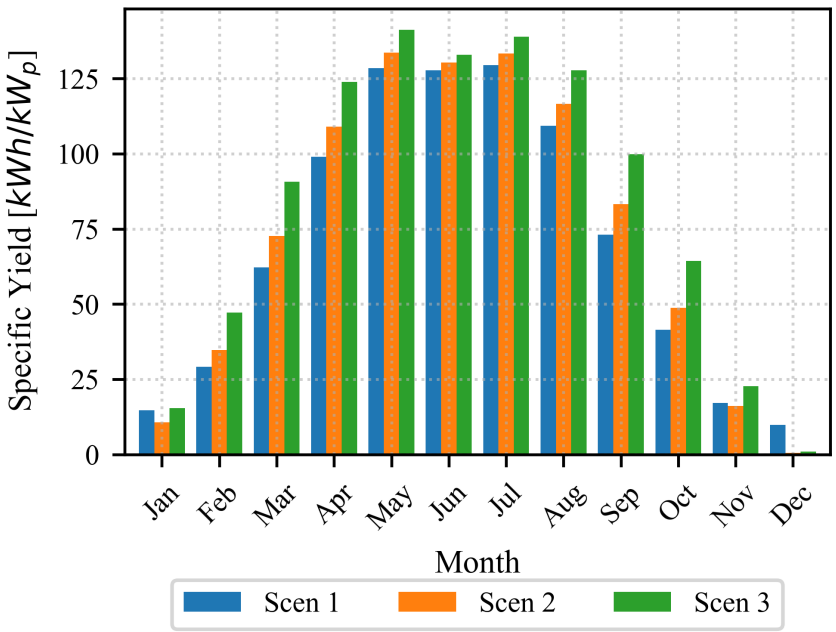

Figure 4.5: Monthly specific yield for three scenarios for the water body denoted as “element 10” [53.17, 6.57] (Groningen)

The generated energy yield distribution per province is illustrated for Scenario 2, 10% coverage in Figure 4.6. The provinces with the lowest share in the generated energy are: 5. Flevoland (3.4%) and 10. Zeeland (3.7%). The provinces with the highest share in the generated energy are: 9. Zuid-Holland (17.1%), 11. Limburg (14.6%) and 6. Gelderland (10.8%). These provinces correspond to the allocated

surface area A_{alloc} (Figure 3.6).

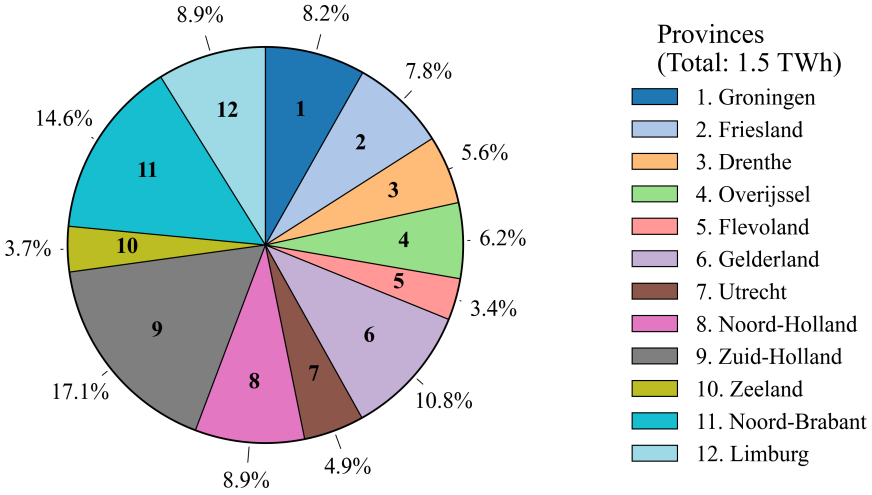

Figure 4.6: Total energy yield EY per province in the Netherlands for Scenario 2, 10% coverage.

4.4. Discussion

The estimated energy yield of floating photovoltaic (FPV) systems is strongly influenced by the suitability of the areas identified in Research Question 1. If these areas are suboptimal, the resulting FPV energy yield will decrease. In addition to site selection, the assumed system conditions play a critical role in determining overall performance.

Several simplifying assumptions were made in this study. For instance, wave induced losses and soiling effects were excluded, and the albedo was assumed to be a constant value of 10.3%. In reality, wave-induced losses and soiling would reduce the energy yield, whereas albedo may increase it. Specifically, albedo could be higher due to pontoon reflectivity and may vary depending on water conditions. When accounting for temporal variation, albedo tends to be lower in summer than in winter, which may lead to higher bifacial gain and energy yield during winter months and slightly reduced performance in summer.

Horizon obstruction was not evaluated for the selected sites, although it may influence the shading factor in Scenarios 1, 2, and 3. Scenario 1 assumes no shading losses due to surrounding vegetation, whereas Scenarios 2 and 3 account only for losses related to the design sun altitude angle. A different choice of sun altitude angle would alter shading losses and, consequently, the estimated energy yield.

Additional uncertainties arise from the use of Meteonorm weather data. The selected weather stations may be located far from the sites, making the interpolation process highly influential. The inverse distance weighting (IDW) interpolation method used in this study exhibited root mean square error (RMSE) values during leave-one-out cross-validation (LOOCV), indicating potential inaccuracies. Site-specific measurements would improve the reliability of FPV system modeling.

For the thermal analysis, the Faiman model for open-structure systems reported in the literature was applied [76]. If the actual thermal behavior of the FPV system deviates from this model, the resulting energy yield estimates may differ. Therefore, experimental validation of the thermal model is recommended.

The electrical performance is fully dependent on the selected FPV module and its datasheet specifications. Variations in module characteristics may lead to different energy yield outcomes.

Overall, the simulated specific yield ranges from 860 kWh/kWp (Scenario 1) to 1,045 kWh/kWp (Scenario 3). Direct comparison with historical data is challenging. For example, annual specific yields reported in 2017 ranged from 800 to 940 kWh/kWp [105], whereas higher values of 880–1,020 kWh/kWp were observed in 2016. These differences reflect interannual variability in solar resources, which is smoothed when using Typical Meteorological Year (TMY) data. Similarly, the Global Solar Atlas [106], which also relies on TMY data, estimates a higher range of 996.5–1,117 kWh/kWp. Based on these estimates, only Scenario 3 demonstrates a well-performing mean specific yield (1,045 kWh/kWp), whereas Scenarios 1 (860 kWh/kWp) and 2 (915 kWh/kWp) fall below the benchmark defined by the Global Solar Atlas. Nevertheless, uncertainty in annual specific yield persists, complicating direct comparisons.

The total FPV energy yield is estimated to range from 0.3 TWh to 4.8 TWh. According to the IEA [107], total PV electricity generation is 21.8 TWh in 2024. The total electricity generation is 123.8 TWh in the Netherlands in 2024, from which 4.2 TWh is exported. This results in 119.6 TWh produced for the country itself. The population in 2024 was 18.05 million inhabitants, and the electricity demand was 6.33 MWh/capita, this results in an distrubted efficiency $\eta_{distributed}$ of 95.5%, Equation 4.5.

$$\eta_{distributed} = \frac{E_{demand-NL}}{E_{generated-NL}} = \frac{6.33 * 18.05 * 10^6}{119.6 * 10^6} = 95.5\% \tag{4.5}$$

To estimate the FPV contribution for the current year (2026), the generated DC energy yield is converted to AC energy yield by applying the performance ratio (PR) in Equation 4.6. Assuming a PR of 0.786 [108], and the Scenario 1, 15% DC energy yield of 4.8 TWh, this corresponds to 3.8 TWh of AC yield. Assuming a population of 18.4 million [15] and an electricity consumption of 6.33 MWh per capita [107], the FPV share is calculated in Equation 4.7 is 3.1%.

$$EY_{AC} = EY_{DC} \times PR \tag{4.6}$$

$$Share_{FPV}[\%] = \frac{EY_{AC} \times \eta_{distributed}}{E_{demand-NL-2026}} = \frac{3.8 \times 95.5\%}{6.33 \times 18.4} = 3.1\% \tag{4.7}$$

Finally, regional differences in energy yield are evident. Provinces such as Noord-Holland, Zuid-Holland, and Utrecht have the highest population densities [109]. In Scenario 2, with 10% coverage, these provinces contribute approximately 30.6% of the total generated energy, highlighting spatial variability in FPV potential. The implementation of FPV systems near areas of high electricity demand (i.e., densely populated regions) is preferable, as it reduces transmission losses.

4.5. Conclusion

Overall, the results demonstrate that the energy yield was successfully calculated for the suitable water body areas from Research Question 1. Based on the defined scenarios, the Datasheet of the selected FPV module, the selected external conditions and the applied interpolation technique IDW (inverse distance weighting) to coordinates of the suitable FPV locations, the PVMD Toolbox was run for the five modules to estimate the DC energy yield.

As a result, the total FPV energy yield spans approximately 0.3 to 4.8 TWh. The mean FPV specific yield is for Scenario 1, 2 and 3, 859, 915, 1045 respecitvely. The spatial variability accross the country varies for the specific yield: in the southern provinces: Zeeland and Limburg the highest SY is found, in the northern province Groningen the lowest SY is found.

With these results, the second research question can be answered: the total energy yield of suitable FPV systems in the Netherlands ranges from 1.3 to 4.8 TWh for Scenario 1, from 0.6 to 2.4 TWh for Scenario 2, and from 0.3 to 1.0 TWh for Scenario 3.

5

Conclusion

This research assessed the potential of floating photovoltaic (FPV) systems on inland waters in the Netherlands through a scenario-based analysis of key system design parameters, including tilt angle, distance from shore, and surface coverage. By integrating spatial analysis with energy yield modelling, the study evaluated both the technical feasibility and the potential contribution of FPV to the national energy system.

The results show that the available inland water dataset can be effectively refined into suitable deployment areas through the application of spatial and technical constraints, including exclusion zones, minimum capacity requirements, and system configuration parameters. Depending on the scenario assumptions, the allocated surface area for FPV deployment ranges from 3.7 to 27.7 km^2, of which 1.1 to 23.9 km^2 is effectively occupied by PV modules. This corresponds to an estimated installed capacity of 0.3 to 5.6 GW_p. Although this represents only a small fraction (approximately 0.7%) of the total inland water area in the Netherlands, it demonstrates that a measurable spatial potential for FPV exists within existing constraints.

The corresponding annual energy yield is estimated to range from 0.3 to 4.8 TWh. The results indicate a strong dependence of total energy production on spatial availability, with scenarios that maximize deployable area achieving the highest total output. At the same time, a clear trade-off is observed between total energy yield and specific yield: lower tilt angles enable higher installation density and overall production, whereas steeper tilt angles result in higher specific yields but reduced spatial potential. Regional differences in solar resource availability further influence system performance, with higher specific yields observed in the southern regions of the country compared to the north. From a national perspective, the contribution of FPV remains modest but relevant. The most favorable scenario could supply 3.1% of the current electricity demand in the Netherlands.

In conclusion, FPV systems present a promising opportunity for renewable energy generation in the Netherlands. Even under conservative coverage assumptions, they can make a relevant contribution to national electricity production. However, the optimal design depends on the chosen objective: prioritizing specific yield improves cost efficiency through reduced installed capacity requirements, whereas prioritizing total energy yield maximizes overall electricity generation.

6

Recommendations

As the research questions of this thesis have been successfully addressed, several directions for future work can be identified to improve model accuracy and broaden the applicability of the results.

A first important step is the validation of spatial and environmental assumptions through on-site assessments. For individual water bodies, the influence of surrounding vegetation on solar availability should be evaluated, and site-specific horizon reconstruction could improve the accuracy of solar resource estimation. In addition, direct field measurements of key parameters, such as surface albedo, would help verify whether the assumed values are representative of inland water conditions.

Further improvement is also possible in the modelling of meteorological inputs. The interpolation of variables such as Direct Normal Irradiance (DNI), Diffuse Horizontal Irradiance (DHI), Global Horizontal Irradiance (GHI), ambient temperature, and wind speed introduces uncertainty. Comparing interpolated datasets with measurements from ground-based weather stations would allow for a more robust quantification of model accuracy, for example through Root Mean Square Error (RMSE) analysis.

Several physical processes excluded from this study also warrant further investigation. Temporal variations in albedo, bifacial gain effects caused by pontoon structures, and the applicability of the open FPV configuration within the Faiman thermal model may all influence energy yield estimates. In addition, wave-induced losses represent a potentially relevant factor that should be quantified. Ultimately, experimental validation using operational FPV systems would provide valuable data to calibrate model parameters and improve predictive reliability.

Beyond technical validation, future research could incorporate an economic assessment of the different scenarios to evaluate cost-effectiveness under varying design objectives and policy priorities. This would allow for a more comprehensive comparison of FPV configurations in terms of both energy output and financial performance.

Finally, the methodology developed in this thesis could be extended to other geographical contexts. In countries with greater topographical variation, elevation effects may significantly influence site suitability and solar exposure. Furthermore, in regions with hydropower infrastructure, hybrid FPV systems on reservoirs and dams may offer additional opportunities for renewable energy integration.

Bibliography

[1] Halyna Dorozhynska. *Ai generated floating solar panel on lake. Generative AI.* URL: https://www.vecteezy.com/photo/40690997-ai-generated-floating-solar-panel-on-lake-generative-ai.

[2] Government of the Netherlands. *Mitigating climate change*. URL: https://www.government.nl/topics/climate-change/mitigating-climate-change.

[3] *Energietransitie in Nederland: maatregelen en innovaties*. URL: https://www.tno.nl/nl/over-tno/organisatie/units/energietransitie/energietransitie-nederland.

[4] Lucía Fernández. *Photovoltaic capacity connected and cumulated in the Netherlands 2013-2024*. May 2025. URL: https://www-statista-com.tudelft.idm.oclc.org/statistics/497475/connected-and-cumulated-photovoltaic-capacity-in-the-netherlands/.

[5] Inam-Ur-Raheem Khoja et al. "A Comparative Review: Floating Photovoltaic, Agrivoltaics, and Ground-Mounted PV Systems". In: *IEEE Access* 13 (2025), pp. 45853–45873. ISSN: 2169-3536. DOI: 10.1109/ACCESS.2025.3547438.

[6] Alok Sahu, Neha Yadav, and K. Sudhakar. *Floating photovoltaic power plant: A review*. Dec. 2016. DOI: 10.1016/j.rser.2016.08.051.

[7] *One in three Dutch homes now have solar panels, but growth slows*. Jan. 2024. URL: https://www.dutchnews.nl/2024/01/one-in-three-dutch-homes-now-have-solar-panels-but-growth-slows/.

[8] Mehmet Korkmaz. "Study Area Map of the Netherlands." Unpublished map provided in person. 2026.

[9] Zainab Akhtar, Mahendra Lalwani, and K.V.S. Rao. "Estimation of energy potential and evaporation in 20 lakes with FPV in Rajasthan India". In: *Renewable Energy* 256 (Jan. 2026), p. 124297. ISSN: 09601481. DOI: 10.1016/j.renene.2025.124297.

[10] Sara Oliveira-Pinto and Jasper Stokkermans. "Assessment of the potential of different floating solar technologies – Overview and analysis of different case studies". In: *Energy Conversion and Management* 211 (May 2020), p. 112747. ISSN: 01968904. DOI: 10.1016/j.enconman.2020.112747.

[11] Josefine Selj et al. *Floating Photovoltaic Power Plants: A Review of Energy Yield, Reliability, and Maintenance*. Tech. rep. Institute for Energy Technology, Instituto Potosino de Investigacion Cientifica y Tecnologica, National University of Singapore, Apr. 2025, p. 66. URL: www.iea-pvps.org.

[12] Statline. *Land use; all categories, municipalities*. Apr. 2023. URL: https://opendata.cbs.nl/statline/#/CBS/en/dataset/70262ENG/table?dl=5EFAE&ts=1759234284357.

[13] Government of the Netherlands. *Agriculture and horticulture*. URL: https://www.government.nl/topics/agriculture/agriculture-and-horticulture.

[14] Eurostat. *Agricultural land prices by region*. May 2025. URL: https://ec.europa.eu/eurostat/databrowser/view/apri_lprc/default/table?lang=en.

[15] Worldometer. *Population of the Netherlands (2025 and historical)*. 2025.

[16] Sathya Shanka Vasuki et al. *A technical review on the energy yield estimation of offshore floating photovoltaic systems*. July 2025. DOI: 10.1016/j.rser.2025.115596.

[17] Statistics Netherlands (CBS). *Power from solar panels increased slightly in 2023*. June 2024. URL: https://www.cbs.nl/en-gb/news/2024/25/power-from-solar-panels-increased-slightly-in-2023.

[18] Parisa Ranjbaran et al. "A review on floating photovoltaic (FPV) power generation units". In: *Renewable and Sustainable Energy Reviews* 110 (Aug. 2019), pp. 332–347. ISSN: 13640321. DOI: 10.1016/j.rser.2019.05.015.

[19] R. Cazzaniga et al. “Floating photovoltaic plants: Performance analysis and design solutions”. In: *Renewable and Sustainable Energy Reviews* 81 (Jan. 2018), pp. 1730–1741. ISSN: 13640321. DOI: 10.1016/j.rser.2017.05.269.

[20] Olusola Bamisile et al. “The environmental factors affecting solar photovoltaic output”. In: *Renewable and Sustainable Energy Reviews* 208 (Feb. 2025), p. 115073. ISSN: 13640321. DOI: 10.1016/j.rser.2024.115073.

[21] Miah Himan et al. “Assessing cooling effects on floating solar PV and performance comparison with ground-based PV systems”. In: 2025, p. 030003. DOI: 10.1063/5.0262242.

[22] Sampurna Panda et al. “Analyzing and evaluating floating PV systems in relation to traditional PV systems”. In: *Materials Today: Proceedings* 103 (2024), pp. 162–167. ISSN: 22147853. DOI: 10.1016/j.matpr.2023.08.244.

[23] M.S. Dorenkamper et al. *The cooling effect of floating PV in two different climate zones: A comparison of field test data from the Netherlands and Singapore*. 2021. URL: https://resolver.tno.nl/uuid:db195a46-6040-4c39-9e8d-5123085211cd.

[24] Rafi Zahedi et al. *Cleaning of floating photovoltaic systems: A critical review on approaches from technical and economic perspectives*. Apr. 2021. DOI: 10.3390/en14072018.

[25] Jaswanth Yerramsetti, Dhatri Sri Paritala, and Ramesh Jayaraman. “Design and Implementation of Automatic Robot for Floating Solar Panel Cleaning System using AI Technique”. In: *2021 International Conference on Computer Communication and Informatics, ICCCI 2021*. Institute of Electrical and Electronics Engineers Inc., Jan. 2021. ISBN: 9781728158754. DOI: 10.1109/ICCCI50826.2021.9402482.

[26] Ruijia Jin et al. “An overview for offshore floating photovoltaic structures and their fluid dynamic issues”. In: *Physics of Fluids* 37 (6 June 2025). ISSN: 1070-6631. DOI: 10.1063/5.0272574.

[27] Raniero Cazzaniga. “Floating PV structures”. In: *Floating PV Plants*. Elsevier, Jan. 2020, pp. 33–45. ISBN: 9780128170618. DOI: 10.1016/B978-0-12-817061-8.00004-X.

[28] R. Claus and M. López. “Key issues in the design of floating photovoltaic structures for the marine environment”. In: *Renewable and Sustainable Energy Reviews* 164 (Aug. 2022), p. 112502. ISSN: 13640321. DOI: 10.1016/j.rser.2022.112502.

[29] Luofeng Huang et al. “Developing reliable floating solar systems on seas: A review”. In: *Ocean Engineering* 322 (Apr. 2025), p. 120525. ISSN: 00298018. DOI: 10.1016/j.oceaneng.2025.120525.

[30] Harsha Lakmal Walpita et al. “Operation and Maintenance of Floating PV Systems: A Review”. In: *IEEE Journal of Photovoltaics* 15 (3 May 2025), pp. 400–415. ISSN: 2156-3381. DOI: 10.1109/JPHOTOV.2025.3548322.

[31] Rahul Kanotra and Ravi Shankar. “Floating Solar Photovoltaic Mooring System Design and Analysis”. In: *OCEANS 2022 - Chennai*. IEEE, Feb. 2022, pp. 1–9. ISBN: 978-1-6654-1821-8. DOI: 10.1109/OCEANSChennai45887.2022.9775352.

[32] Wei Shi et al. “Review on the development of marine floating photovoltaic systems”. In: *Ocean Engineering* 286 (Oct. 2023), p. 115560. ISSN: 00298018. DOI: 10.1016/j.oceaneng.2023.115560.

[33] GL DNV. *DNV-RP-0584: Design, development and operation of floating solar photovoltaic systems*. 2021.

[34] Alberto Ghigo et al. “Design and Analysis of a Floating Photovoltaic System for Offshore Installation: The Case Study of Lampedusa”. In: *Energies* 15 (23 Nov. 2022), p. 8804. ISSN: 1996-1073. DOI: 10.3390/en15238804.

[35] Mohammed Al Araimi, Mohamed Al Mandhari, and Aritra Ghosh. “Comparative analysis of bifacial and monofacial FPV system in the UK”. In: *Solar Compass* 13 (Mar. 2025), p. 100106. ISSN: 27729400. DOI: 10.1016/j.solcom.2025.100106.

[36] Giuseppe Marco Tina and Fausto Bontempo Scavo. “Energy performance analysis of tracking floating photovoltaic systems”. In: *Heliyon* 8 (8 Aug. 2022). Comparison between tracking and non-tracking for 2 locations: italy and germany., e10088. ISSN: 24058440. DOI: 10.1016/j.heliyon.2022.e10088.

[37] Hesan Ziar et al. “Innovative floating bifacial photovoltaic solutions for inland water areas”. In: *Progress in Photovoltaics: Research and Applications* 29 (7 July 2021), pp. 725–743. ISSN: 1062-7995. DOI: 10.1002/pip.3367.

[38] Sustainergy Solar. *Advanced Technical Features of Bifacial Solar Panels*. 2024. URL: https://www.linkedin.com/pulse/advanced-technical-features-bifacial-solar-panels-sustainergy-solar-bkccf/.

[39] Giuseppe Marco Tina et al. “Thermal comparison of floating bifacial and monofacial photovoltaic modules considering two laying configurations”. In: *Applied Energy* 389 (July 2025), p. 125732. ISSN: 03062619. DOI: 10.1016/j.apenergy.2025.125732.

[40] Brian. *Photovoltaic Module Installation: Horizontal vs. Vertical*. Maysun Solar. 2023. URL: https://www.maysunsolar.com/photovoltaic-module-installation-horizontal-vs-vertical/ (visited on 10/21/2025).

[41] Aboubakr El Hammoumi et al. “Design and construction of a test bench to investigate the potential of floating PV systems”. In: *Journal of Cleaner Production* 278 (Jan. 2021), p. 123917. ISSN: 09596526. DOI: 10.1016/j.jclepro.2020.123917.

[42] Ramanan C.J. et al. “Design study on the parameters influencing the performance of floating solar PV”. In: *Renewable Energy* 223 (Mar. 2024), p. 120064. ISSN: 09601481. DOI: 10.1016/j.renene.2024.120064.

[43] Gofran Chowdhury, Mohamed Haggag, and Jef Poortmans. “How cool is floating PV? A state-of-the-art review of floating PV’s potential gain and computational fluid dynamics modeling to find its root cause”. In: *EPJ Photovoltaics* 14 (Aug. 2023), p. 24. ISSN: 2105-0716. DOI: 10.1051/epjpv/2023015.

[44] Hamza Nisar et al. “Thermal and electrical performance of solar floating PV system compared to on-ground PV system-an experimental investigation”. In: *Solar Energy* 241 (July 2022), pp. 231–247. ISSN: 0038092X. DOI: 10.1016/j.solener.2022.05.062.

[45] A. A. Widayat et al. “Comparison and Optimization of Floating Bifacial and Monofacial Solar PV System in a Tropical Region”. In: *2020 9th International Conference on Power Science and Engineering (ICPSE)*. IEEE, Oct. 2020, pp. 66–70. ISBN: 978-1-7281-8453-1. DOI: 10.1109/ICPSE51196.2020.9354374.

[46] Niclas. *Tilted Single Axis Tracker*. URL: https://sinovoltaics.com/learning-center/csp/tilted-single-axis-tracker/.

[47] Swati S Gurfude and P S Kulkarni. “Energy Yield of Tracking Type Floating Solar PV Plant”. In: *2019 National Power Electronics Conference (NPEC)*. IEEE, Dec. 2019, pp. 1–6. ISBN: 978-1-7281-4428-3. DOI: 10.1109/NPEC47332.2019.9034846.

[48] Emma Forester et al. *Siting considerations for floating solar photovoltaic energy: A systematic review*. Apr. 2025. DOI: 10.1016/j.rser.2025.115360.

[49] Dipanjan Ghose, Sudeep Pradhan, and Shabbiruddin. “Floating solar plants – Exploring a new dimension of energy generation: A case study”. In: *Energy Sources, Part A: Recovery, Utilization, and Environmental Effects* 47 (1 June 2021), pp. 10396–10426. ISSN: 1556-7036. DOI: 10.1080/15567036.2021.1965266.

[50] Emilio Muñoz-Cerón et al. “Floating photovoltaics systems on water irrigation ponds: Technical potential and multi-benefits analysis”. In: *Energy* 271 (May 2023), p. 127039. ISSN: 03605442. DOI: 10.1016/j.energy.2023.127039.

[51] Mohit Acharya and Sarvesh Devraj. “Floating solar photovoltaic (FSPV): a third pillar to solar PV sector”. In: *New Delhi, India: The Energy and Resources Institute* (2019).

[52] Qianfeng Ji et al. “Potential assessment of floating photovoltaic solar power in China and its environmental effect”. In: *Clean Technologies and Environmental Policy* 25 (7 Sept. 2023), pp. 2263–2285. ISSN: 1618-954X. DOI: 10.1007/s10098-023-02503-5.

[53] Fengjia Guo et al. “Locations appraisal framework for floating photovoltaic power plants based on relative-entropy measure and improved hesitant fuzzy linguistic DEMATEL-PROMETHEE method”. In: *Ocean & Coastal Management* 215 (Dec. 2021), p. 105948. ISSN: 09645691. DOI: 10.1016/j.ocecoaman.2021.105948.

[54] Marcolino Matheus de Souza Nascimento et al. “Offshore wind and solar complementarity in Brazil: A theoretical and technical potential assessment”. In: *Energy Conversion and Management* 270 (Oct. 2022), p. 116194. ISSN: 01968904. DOI: 10.1016/j.enconman.2022.116194.

[55] Kumbuso Joshua Nyoni et al. “Hydro–Connected Floating PV Renewable Energy System and Onshore Wind Potential in Zambia”. In: *Energies* 14 (17 Aug. 2021), p. 5330. ISSN: 1996-1073. DOI: 10.3390/en14175330.

[56] Salvatore Di Grazia and Giuseppe Marco Tina. “Optimal site selection for floating photovoltaic systems based on Geographic Information Systems (GIS) and Multi-Criteria Decision Analysis (MCDA): a case study”. In: *International Journal of Sustainable Energy* 43 (1 Dec. 2024). ISSN: 1478-6451. DOI: 10.1080/14786451.2023.2167999.

[57] Abbas Einali et al. “Prioritize renewable energy resources in main Iranian ports area using AHP method”. In: *International Journal Of Coastal, Offshore And Environmental Engineering (ijcoe)* 7.4 (2022), pp. 7–16.

[58] R. Bhanja and K. Roychowdhury. “A MULTI-CRITERIA GIS BASED ANALYTICAL HIERARCHICAL APPROACH FOR SOLAR PHOTOVOLTAIC FARM SITE SELECTION IN THE KOLKATA METROPOLITAN AREA, INDIA”. In: *The International Archives of the Photogrammetry, Remote Sensing and Spatial Information Sciences* XLVIII-4/W5-2022 (Oct. 2022), pp. 31–36. ISSN: 2194-9034. DOI: 10.5194/isprs-archives-XLVIII-4-W5-2022-31-2022.

[59] Dimitra G. Vagiona et al. “Site Selection of Offshore Solar Farm Deployment in the Aegean Sea, Greece”. In: *Journal of Marine Science and Engineering* 10 (2 Feb. 2022), p. 224. ISSN: 2077-1312. DOI: 10.3390/jmse10020224.

[60] Fatima zahra Ouchani et al. “Geographic Information System-based Multi-Criteria Decision-Making analysis for assessing prospective locations of Pumped Hydro Energy Storage plants in Morocco: Towards efficient management of variable renewables”. In: *Journal of Energy Storage* 55 (Nov. 2022), p. 105751. ISSN: 2352152X. DOI: 10.1016/j.est.2022.105751.

[61] Madison K. Hoffacker, Michael F. Allen, and Rebecca R. Hernandez. “Land-Sparing Opportunities for Solar Energy Development in Agricultural Landscapes: A Case Study of the Great Central Valley, CA, United States”. In: *Environmental Science & Technology* 51 (24 Dec. 2017), pp. 14472–14482. ISSN: 0013-936X. DOI: 10.1021/acs.est.7b05110.

[62] Prateek Joshi, Evan Rosenlieb, and Sika Gadzanku. “Enabling Floating Solar Photovoltaic (FPV) Deployment: FPV Technical Potential Assessment for Southeast Asia”. In: (2023). DOI: 10.2172/1974575. URL: https://doi.org/10.2172/1974575.

[63] Mariana Padilha Campos Lopes et al. “Technical potential of floating photovoltaic systems on artificial water bodies in Brazil”. In: *Renewable Energy* 181 (Jan. 2022), pp. 1023–1033. ISSN: 09601481. DOI: 10.1016/j.renene.2021.09.104.

[64] Yanwei Sun et al. “Measuring dynamics of solar energy resource quality: Methodology and policy implications for reducing regional energy inequality”. In: *Renewable Energy* 197 (Sept. 2022), pp. 138–150. ISSN: 09601481. DOI: 10.1016/j.renene.2022.07.122.

[65] Abhishek Pandey et al. “Location Intelligence in Amalgamation of Floating Solar PV & Electric Vehicle”. In: *IGARSS 2022 - 2022 IEEE International Geoscience and Remote Sensing Symposium*. IEEE, July 2022, pp. 2888–2891. ISBN: 978-1-6654-2792-0. DOI: 10.1109/IGARSS46834.2022.9883342.

[66] “Unlocking the floating photovoltaic potential of Türkiye’s hydroelectric power plants”. In: *Renewable Energy* 199 (2022), pp. 1495–1509. ISSN: 0960-1481. DOI: https://doi.org/10.1016/j.renene.2022.09.096. URL: https://www.sciencedirect.com/science/article/pii/S0960148122014550.

[67] Sung-Min Kim, Myeongchan Oh, and Hyeong-Dong Park. “Analysis and Prioritization of the Floating Photovoltaic System Potential for Reservoirs in Korea”. In: *Applied Sciences* 9 (3 Jan. 2019), p. 395. ISSN: 2076-3417. DOI: 10.3390/app9030395.

[68] Harish Puppala et al. “Hybrid multi-criteria framework to determine the hierarchy of hydropower reservoirs in India for floatovoltaic installation”. In: *International Journal of Thermofluids* 16 (Nov. 2022), p. 100229. ISSN: 26662027. DOI: 10.1016/j.ijft.2022.100229.

[69] Robert S. Spencer et al. “Floating Photovoltaic Systems: Assessing the Technical Potential of Photovoltaic Systems on Man-Made Water Bodies in the Continental United States”. In: *Environmental Science & Technology* 53 (3 Feb. 2019), pp. 1680–1689. ISSN: 0013-936X. DOI: 10.1021/acs.est.8b04735.

[70] *Solar Photovoltaic Glint and Glare Study*. Tech. rep. Technical report prepared for Beane Solar Farm Project. Accessed October 2025. Pager Power Ltd., 2024. URL: https://www.beane-solarfarm.co.uk/media/rithq505/11964a-solar-photovaltaic-glint-and-glare-study-17-10-2024.pdf.

[71] World Bank Group. *Where sun meets water: floating solar market report*. World Bank, 2019.

[72] M. S. Korkmaz and A. D. Sahin. “Developing a micrositing methodology for floating photovoltaic power plants”. In: *International Journal of Environmental Science and Technology* 20 (7 July 2023), pp. 7621–7644. ISSN: 1735-1472. DOI: 10.1007/s13762-023-04961-2.

[73] Francisco Javier Gómez-Gil, Xiaoting Wang, and Allen Barnett. “Energy production of photovoltaic systems: Fixed, tracking, and concentrating”. In: *Renewable and Sustainable Energy Reviews* 16 (1 Jan. 2012), pp. 306–313. ISSN: 13640321. DOI: 10.1016/j.rser.2011.07.156.

[74] Mohd Herwan Sulaiman et al. “Hierarchical power output prediction for floating photovoltaic systems”. In: *Energy* 323 (May 2025), p. 135883. ISSN: 03605442. DOI: 10.1016/j.energy.2025.135883.

[75] Maarten Dörenkämper et al. “The cooling effect of floating PV in two different climate zones: A comparison of field test data from the Netherlands and Singapore”. In: *Solar Energy* 219 (May 2021), pp. 15–23. ISSN: 0038092X. DOI: 10.1016/j.solener.2021.03.051.

[76] Maarten Dörenkämper et al. “Modeled and Measured Operating Temperatures of Floating PV Modules: A Comparison”. In: *Energies* 16 (20 Oct. 2023), p. 7153. ISSN: 1996-1073. DOI: 10.3390/en16207153.

[77] Han Sang Jeong et al. “A Study on the Power Generation Prediction Model Considering Environmental Characteristics of Floating Photovoltaic System”. In: *Applied Sciences* 10 (13 June 2020), p. 4526. ISSN: 2076-3417. DOI: 10.3390/app10134526.

[78] A. Alcañiz et al. “Offshore floating PV–DC and AC yield analysis considering wave effects”. In: *Energy Conversion and Management* 300 (Jan. 2024), p. 117897. ISSN: 01968904. DOI: 10.1016/j.enconman.2023.117897.

[79] Vilde Stueland Nysted et al. “Modelling wave-induced losses for floating photovoltaics: Impact of design parameters and environmental conditions”. In: *Solar Energy* 293 (June 2025), p. 113439. ISSN: 0038092X. DOI: 10.1016/j.solener.2025.113439.

[80] Patrick Jowett. *Türkiye publishes rules for Floating solar*. 2025. URL: https://www.pv-magazine.com/2025/12/12/turkiye-publishes-rules-for-floating-solar/.

[81] *What exactly is floating pv?* 2025. URL: https://energiewende.bundeswirtschaftsministerium.de/EWD/Redaktion/EN/Newsletter/2025/10/Meldung/direkt-account.html.

[82] Terence Fong and Mark Eisenegger. “Floating Photovoltaic System on Kranji Reservoir – Environmental Impact Assessment (EIA)”. In: Volume 1 (May 2024).

[83] Nisha Kaur et al. “Floating solar sustainability on land and ocean: A strategic assessment using SWOT-TWOS-PESTLE analysis”. In: *Science and Technology for Energy Transition* 80 (Feb. 2025), p. 27. ISSN: 2804-7699. DOI: 10.2516/stet/2024114.

[84] Cloudfresh. *Google’s Maps data: How does it work?* Nov. 16, 2022. URL: https://cloudfresh.com/en/blog/google-s-maps-data-how-does-it-work/ (visited on 12/08/2025).

[85] URL: https://wiki.openstreetmap.org/wiki/Map_features.

[86] H. Butler et al. *RFC 7946: The GEOJSON format*. 2016. URL: https://datatracker.ietf.org/doc/html/rfc7946.

[87] URL: https://www.topografix.com/gpx/1/1/.

[88] Timothy Wilson. *OGC 07-147r2 Open Geospatial Consortium Inc. Reference number of this OGC® project document: OGC 07-147r2 OGC® KML*. Tech. rep. 2008. URL: http://www.opengeospatial.org/legal/..

[89] OpenStreetMap contributors. *Planet dump retrieved from https://planet.osm.org*. https://www.openstreetmap.org. 2017.

[90] *Nationaal georegister: boomhoogte in Nederland*. 2024. URL: https://nationaalgeoregister.nl/geonetwork/srv/dut/catalog.search#/metadata/3659cae2-29bf-49af-bd8d-737a0bb3dd42.

[91] *Bestuurlijke gebieden*. 2025. URL: https://service.pdok.nl/kadaster/bestuurlijkegebieden/atom/v1_0/index.xml.

[92] Mamata Akella. *The 7 best GIS software tools for accurate and efficient mapping*. 2025. URL: https://felt.com/blog/the-7-top-gis-software-compared.

[93] *GitLab TU Delft*. URL: https://gitlab.tudelft.nl/rsantbergen/msc_eline_fpvpotential.

[94] Het Kennis en Exploitatiecentrum voor Officiële Overheidspublicaties. *Basiskaart Aquatisch: DE Watertypenkaart 2013*. 2024. URL: https://data.overheid.nl/dataset/13653-basiskaart-aquatisch--de-watertypenkaart-2013.

[95] Golam Rabbani Rimon, M. Sojib Ahmed, and M. Ryyan Khan. "Albedo and Temperature Aware Analysis of Bifacial vs Monofacial Floating Photovoltaics in Bangladesh". In: *2022 12th International Conference on Electrical and Computer Engineering (ICECE)*. IEEE, Dec. 2022, pp. 13–15. ISBN: 979-8-3503-9879-3. DOI: 10.1109/ICECE57408.2022.10088821.

[96] Sara Golroodbari and Wilfried van Sark. "On the effect of dynamic albedo on performance modelling of offshore floating photovoltaic systems". In: *Solar Energy Advances* 2 (2022), p. 100016. ISSN: 2667-1131. DOI: https://doi.org/10.1016/j.seja.2022.100016. URL: https://www.sciencedirect.com/science/article/pii/S2667113122000043.

[97] Saboor Shaik et al. "Experimental analysis on the impacts of soil deposition and bird droppings on the thermal performance of photovoltaic panels". In: *Case Studies in Thermal Engineering* 48 (Aug. 2023), p. 103128. ISSN: 2214157X. DOI: 10.1016/j.csite.2023.103128.

[98] Sohabul Alam et al. "Design and Feasibility Analysis of 1 MWp Floating Solar Park in Bhatiari Lake Using PVsyst Software". In: *2024 6th International Conference on Sustainable Technologies for Industry 5.0 (STI)*. IEEE, Dec. 2024, pp. 1–6. ISBN: 979-8-3315-3195-9. DOI: 10.1109/STI64222.2024.10951069.

[99] M.R. Vogt et al. "Introducing a comprehensive physics-based modelling framework for tandem and other PV systems". In: *Solar Energy Materials and Solar Cells* 247 (2022), p. 111944. ISSN: 0927-0248. DOI: https://doi.org/10.1016/j.solmat.2022.111944. URL: https://www.sciencedirect.com/science/article/pii/S0927024822003622.

[100] Patrizia Bolognesi. *Trends of solar silicon wafer size and thickness for different cell technologies*. 2025. URL: https://www.diamonds4if.eu/news/trends-of-solar-silicon-wafer-size-and-thickness-for-different-cell-technologies/.

[101] Timothy Bralower and David Bice. *Albedo*. URL: https://courses.ems.psu.edu/earth103/node/1002.

[102] T. C. Hsiao. "Plant-atmosphere interactions, evapotranspiration and irrigation scheduling". In: *Acta Horticulturae* (278 June 1990), pp. 55–66. ISSN: 0567-7572. DOI: 10.17660/ActaHortic.1990.278.3.

[103] URL: https://pvlib-python.readthedocs.io/en/latest/reference/generated/pvlib.albedo.inland_water_dvoracek.html.

[104] Delft High Performance Computing Centre (DHPC). *DelftBlue Supercomputer (Phase 2)*. https://www.tudelft.nl/dhpc/ark:/44463/DelftBluePhase2. 2024.

[105] Statistics Netherlands. *An innovative way to estimate solar energy yields*. 2024. URL: https://www.cbs.nl/en-gb/about-us/innovation/project/an-innovative-way-to-estimate-solar-energy-yields.

[106] World Bank Group. *Global Solar Atlas*. Accessed: 24 October 2025. 2025. URL: https://globalsolaratlas.info/map.

[107] *Sources of electricity generation, the Netherlands*. 2024. URL: https://www.iea.org/countries/the-netherlands/electricity.

[108] Klaus-Dieter Jäger et al. *Solar Energy: Fundamentals, Technology and Systems*. UIT Cambridge, 2016.

[109] Centraal Bureau voor de Statistiek. *Dashboard Bevolking*. 2026. URL: https://www.cbs.nl/nl-nl/visualisaties/dashboard-bevolking.

[110] *Nationaal kouderecord bestaat 80 jaar*. 2022. URL: https://www.knmi.nl/over-het-knmi/nieuws/nationaal-kouderecord-bestaat-80-jaar.

[111] JinkoSolar. *JinkoSolar Global Installation Manual*. Revision 20240814_A1. Jinko Solar Co., Ltd. 2024. URL: https://www.jinkosolar.com/uploads/JinkoSolar%20Global%20Installation%20Manual_20240814_A1.pdf.

[112] 2024. URL: https://www.solid-c.de/en/maintenance-walkways/.

[113] Centraal Bureau voor de Statistiek (CBS). *Bevolking; kerncijfers volgens stedelijke agglomeratie, regio — CBS StatLine, dataset 70072ned*. Accessed: 2025-10-27. CBS. 2025. URL: https://opendata.cbs.nl/#/CBS/nl/dataset/70072ned/table?dl=B01D1 (visited on 10/27/2025).

[114] *Netherlands — Annual Wind Speed*. Accessed: 27 October 2025. n.d. URL: https://www.currentresults.com/Weather/Netherlands/wind-speed-annual.php.

[115] *Netherlands country overview*. 2020. URL: https://climateknowledgeportal.worldbank.org/country/netherlands.

[116] GoDigit. *Airports in Netherlands*. Accessed: 27 October 2025. n.d. URL: https://www.godigit.com/international-travel-insurance/airports/airports-in-netherlands.

[117] URL: https://www.knmi.nl/kennis-en-datacentrum/uitleg/automatische-weerstations.

[118] 2023. URL: https://mn8.meteonorm.com/assets/downloads/mn82_theory.pdf.

[119] Wouter Knap. “Basic measurements of radiation at station Cabauw (2005-11)”. In: In: Knap, W (2022): Basic and other measurements of radiation at station Cabauw (2005-02 et seq). PANGAEA, 2008. DOI: 10.1594/PANGAEA.695947. URL: https://doi.org/10.1594/PANGAEA.695947.

A

Appendix GIS-based assessment

A.1. Selection of FPV system

The FPV panel is selected as JAM72D40-605W bifacial module (JA Solar) for this study. The 4P25S (4 Parallel, 25 Series) configuration was selected for this study (Figure A.1). The W_{mod} contains 4 panels in parallel ($W_{mod} = 4 \times W_{panel}$), while the L_{mod} 25 in series ($L_{mod} = 25 \times L_{panel}$). To limit system complexity, a fixed-tilt, south-oriented configuration (shown in Figure A.1: Side view W_{mod}) was adopted instead of tracking systems. A landscape-oriented configuration was adopted, as it provides improved performance [39].

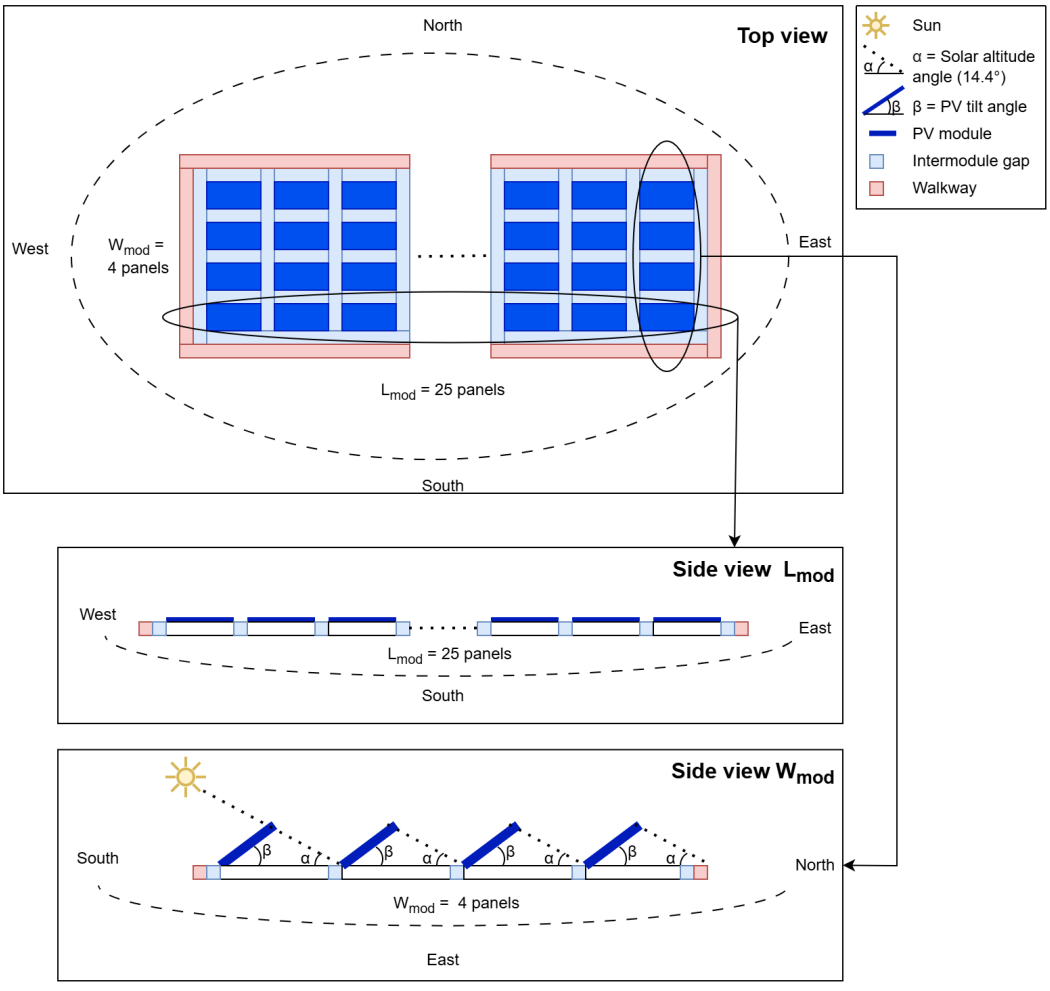

Figure A.1: 4P25S configuration: system top and side views

The 4P25S configuration was found by obtaining the number of modules per string N_{string} to be under the inverter voltage constraint Equation A.1.

$$V_{max} = N_{string} \times V_{oc} \times [1 + (\beta_{VOC} \times (T_{min} - 25°\text{C}))] \tag{A.1}$$

Using a maximum inverter voltage of 1500 V, $V_{oc} = 53$ V, $\beta_{VOC} = -0.25\%/°\text{C}$ (Datasheet in Appendix), and for the minimum temperature the coldest recorded temperature of $-27.4°\text{C}$ [110] was used, the maximum string length was determined as $N_{string} = 25$. This amount of modules per string even allowed a lower temperature of $-27.83°\text{C}$.

A.2. Power Density calculation

Power density depends on module spacing, which is governed by tilt angle and shading constraints. Module spacing consists of a 0.01 m intermodule gap (W_{gap1}) and a 0.6 m walkway intended for maintenance (W_{gap2}), as is illustrated in Figure A.1. The intermodule gap was set to 0.01 m to facilitate the ventilation and heat dissipation of the module based on [111], while the maintenance gaps were required to be a minimum of 0.05 m [112]. As a result, the panel length remains constant at 2.312 m (Equation A.2), with $L_{dimension} = 2.278$, whereas the panel width (Equation A.3) varies depending on the shading gap. The tilt width and shading width where defined as: $W_{tilt} = W_{dimension} \times cos(tilt)$, $W_{shading} = W_{dimension} \times \frac{sin(tilt)}{tan(\alpha)}$.When the shading gap is sufficiently large to accommodate both the maintenance and intermodule gaps, the additional spacing is incorporated within the shading gap itself. As illustrated in Figure A.2, Scenarios 2 and 3 efficiently utilize the shading gap, whereas Scenario 1 does not.

$$L_{panel} = L_{dimension} + W_{gap1} + \frac{W_{gap2}}{25} \tag{A.2}$$

$$W_{panel}(\alpha_{cap}) = \begin{cases} W_{tilt} + W_{shading} & \text{if } W_{shading} > 0.61 \\ W_{tilt} + W_{shading} + W_{gap1} + \frac{W_{gap2}}{4} & \text{otherwise} \end{cases} \tag{A.3}$$

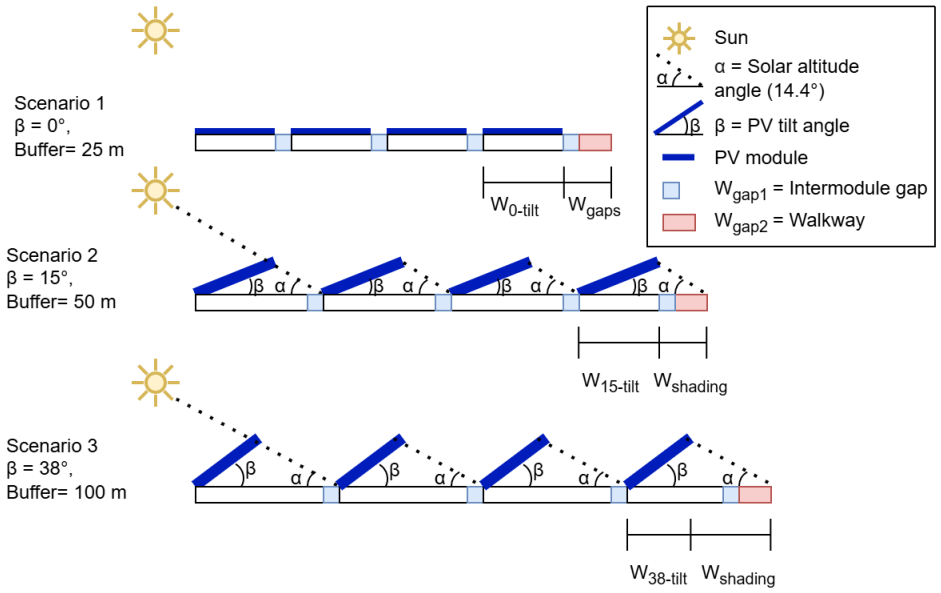

Figure A.2: Side view of $W_{mod}(\alpha_{cap})$ per scenario, showing that Scenario 2, 3 shading gap utitizes maintenance gap and intermodule spacing effectively

Selection of Design Solar Altitude

To balance irradiance losses and power density, a sensitivity analysis was performed using Meteonorm data from De Bilt. The POA irradiance was calculated with an albedo of 10.3%. Figure A.3 illustrates the trade-off between annual POA irradiance and power density for varying solar altitude thresholds. The

left graph shows that reducing the design sun altitude, results in higher irradiance POA outputs, while the right graph shows that the power density reduces significantly. A design solar altitude of $14.4°$ (solar noon at winter solstice) was selected, as it provides a reasonable compromise between energy yield ($\approx 980 kWh/m^2$) and spatial efficiency ($\approx 117 W/m^2$ for Scenario 2) (Table A.1).

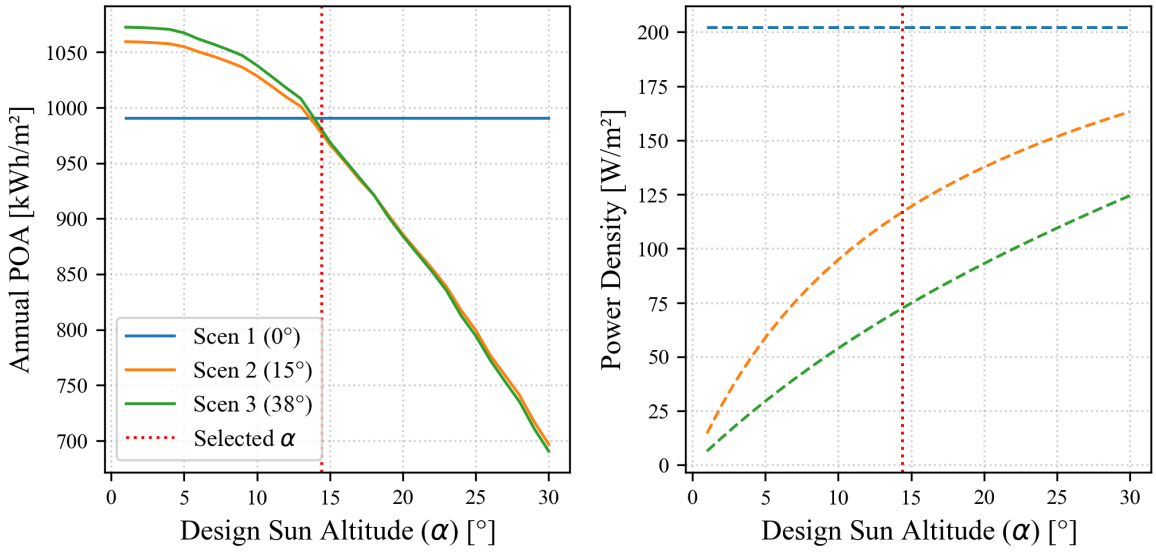

Figure A.3: Trade-off between POA irradiance losses and power density for weather station De Bilt

Table A.1: Simulated scenarios with selected sun altitude of $14.4°$

Scenario	Tilt angle	Cap 14.4°	Annual POA [kWh/m²]	POA loss [%]	Power Density [W/m²]
Scenario 1	0°	No	989.90	0	202.22
Scenario 2	15°	Yes	978.69	7.54	116.90
Scenario 3	38°	Yes	982.44	8.22	72.43

A.3. QGIS interface

The QGIS interface is shown in Figure A.4.

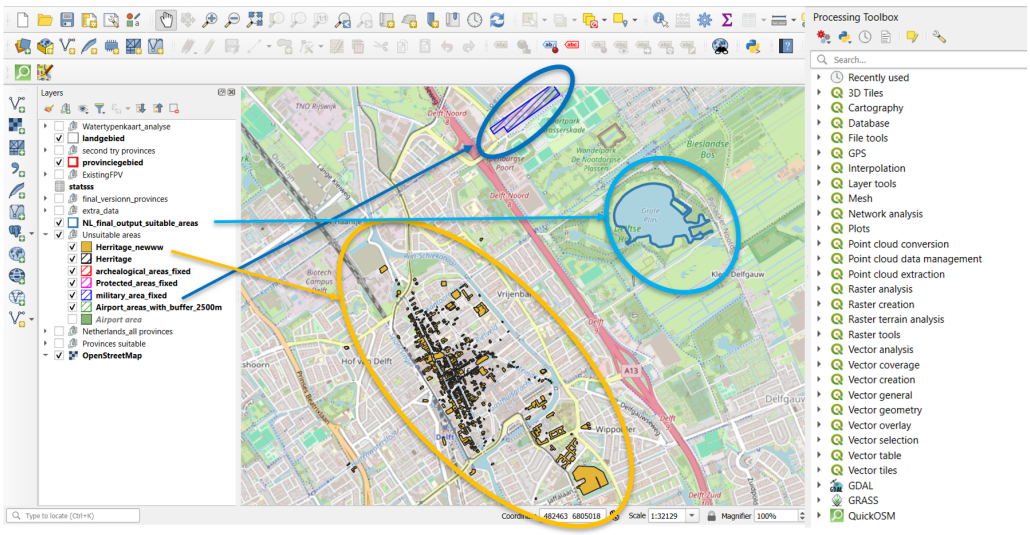

Figure A.4: Example of QGIS interface

The main components of the interface include the Layers Panel on the left-hand side, where individual layers can be activated or deactivated to display them on the map. Some layers are highlighted to indicate specific areas, such as military zones, heritage sites, and suitable areas. On the right-hand side, the Processing Toolbox is displayed. This toolbox contains numerous tools for spatial analysis and data processing, such as Vector Geometry (buffer), Vector Overlay (enabling Difference function to remove unsuitable areas from the data set).

An essential step in the workflow is importing the data using the Data Source Manager. This tool allows the user to select the appropriate data format, such as vector data, GeoPackage data, or raster data. For the KML data obtained from Overpass Turbo, the vector data import option is used. Then, the imported KML data is converted to GeoPackage format using the Fix Geometries function available in the Processing Toolbox. Converting the data to GeoPackage format ensures correct geometry handling and improves the reliability of further spatial analysis.

A.4. Overpass Query

A.4.1. Water data

The query for Overpass Turbo for each province to obtain water bodies.

```
[out:json][timeout:60];
// example for province Zeeland, this name is changed for the other 11 provinces to their corresponding name
area["name"="Zeeland"]["boundary"="administrative"]["admin_level"="4"]->.searchArea;
// find natural=water
// excluding certain cases: flow, boats, unsuitable waters...
nwr["natural"="water"]
  ["seamark_type"!~"^(harbour|harbour_basin)$"]
  ["seamark_harbour_category"!="marina"]
  ["harbour"!="yes"]
  ["landcover"!="grass"]
  ["wetland"!="wet_meadow"]
  ["water"!~"^(river|canal|stream|oxbow|ditch|lock|fish_pass|wastewater|
  harbour|moat|stream_pool_reflecting_pool|swale|sewage)$"]
  ["waterway"!~"^(river|riverbank|stream|tidal_channel|canal|drain|ditch|
  pressurised|fairway|boatyard|dam|weir|waterfall|lock_gate|turning_point|
  water_point|fuel|soakhole)$"]
  ["boat"!="yes"]
  ["ship"!="yes"]
  ["landuse"!~"^(aquaculture|farmland|grass|harbour|port|industrial|military)$"]
  ["amenity"!="boat_storage"]
  ["tidal"!~"^(yes|intermittent)$"]
  ["leisure"!~"^(harbour|nature_reserve|marina|paddling_pool|playground|water_park)$"]
  (area.searchArea);
out geom;
```

A.4.2. Unsuitable Areas

Obtain unsuitable areas:

1. Military areas
2. Protected areas
3. Airports
4. Herritage sites
5. Archaeological sites
6. Fairway
7. Aquaculture zones

```
// Military areas in the Netherlands
[out:json][timeout:60];
// define country by ISO code
area["ISO3166-1"="NL"]->.netherlands;
// find nodes / ways / relations tagged as military landuse or military bases
(
  node["landuse"="military"](area.netherlands);
  way["landuse"="military"](area.netherlands);
  relation["landuse"="military"](area.netherlands);

  node["military"="base"](area.netherlands);
  way["military"="base"](area.netherlands);
  relation["military"="base"](area.netherlands);
```

```
  node["military"="range"](area.netherlands);
  way["military"="range"](area.netherlands);
  relation["military"="range"](area.netherlands);
);
out geom;


// Protected areas
[out:json][timeout:60];
// define country by ISO code
area["ISO3166-1"="NL"]->.netherlands;
// gather results
nwr["boundary"="protected_area"](area.netherlands);
// print results
out geom;


// Airport
[out:json][timeout:60];
// define country by ISO code
area["ISO3166-1"="NL"]->.netherlands;
// gather results
nwr["aeroway"="aerodrome"](area.netherlands);
// print results
out geom;


//Heritage
[out:json][timeout:60];
// define country by ISO code
area["ISO3166-1"="NL"]->.netherlands;
// gather results
nwr["heritage"=2](area.netherlands);
// print results
out geom;


// Archaeological sites
[out:json][timeout:60];
// define country by ISO code
area["ISO3166-1"="NL"]->.netherlands;
// gather results
nwr["historic"="archaeological_site"](area.netherlands);
// print results
out geom;


        /*Fairway
*/
[out:json][timeout:60];
// define country by ISO code
area["ISO3166-1"="NL"]->.netherlands;
// gather results
nwr["waterway"="fairway"](area.netherlands);
// print results
out geom;



// aquaculturezones in the Netherlands
[out:json][timeout:60];
// define country by ISO code
area["ISO3166-1"="NL"]->.netherlands;


nwr["landuse"="aquaculture"](area.netherlands);

// return full geometry
out geom;
```

A.5. Step 1. C Validation

A spatial overlap analysis was performed using the *Vector Analysis: Overlap Analysis* tool in QGIS. The filtered OSM dataset was used as the input layer and the Watertypenkaart 2013 as the overlay layer. During this step, one OSM feature of the National Water Data contained an invalid geometry and was removed, resulting in 290,206 elements used for analysis.

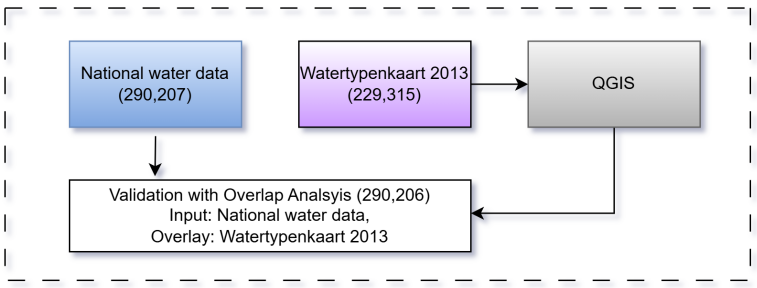

Figure A.5: Workflow validation OSM data

The tool calculated, for each OSM feature, the percentage of its area intersecting with the classified water map (Equation A.4). The overlap ratio ranges from 0–100%, where 0% indicates no spatial intersection and 100% indicates complete spatial agreement.

$$Overlap\_ratio = \frac{Area\_of\_intersection}{Total\_area\_of\_OSM\_water\_body} \cdot 100 \tag{A.4}$$

To assess the statistical distribution of spatial agreement, overlap ratios were grouped in 10% intervals using attribute filtering (e.g., *("watertypenkaart_pc" > 10) AND ("watertypenkaart_pc" <= 20)*). A histogram was used to evaluate the frequency distribution of overlap ratios, while a cumulative distribution function (CDF) was used to assess cumulative proportions.

Based on the distribution characteristics, overlap ratios were classified into three agreement categories:

Category	Overlap ratio (PC)
Full	90–100%
Partial	50–90%
None	<50%

An example of water bodies with different overlap ratios is presented in Figure A.6. The calculated overlap ratios for the seven identified features are:(1) 79.8%, (2) 81.8%, (3) 96.0%, (4) 85.0%, (5) 0%, (6) 97.2%, and (7) 31.6%. Based on the defined thresholds, water bodies 3 and 6 fall into the Full agreement category (90–100%), water bodies 1, 2, and 4 into the Partial category (50–90%), and water bodies 5 and 7 into the None category (<50%).

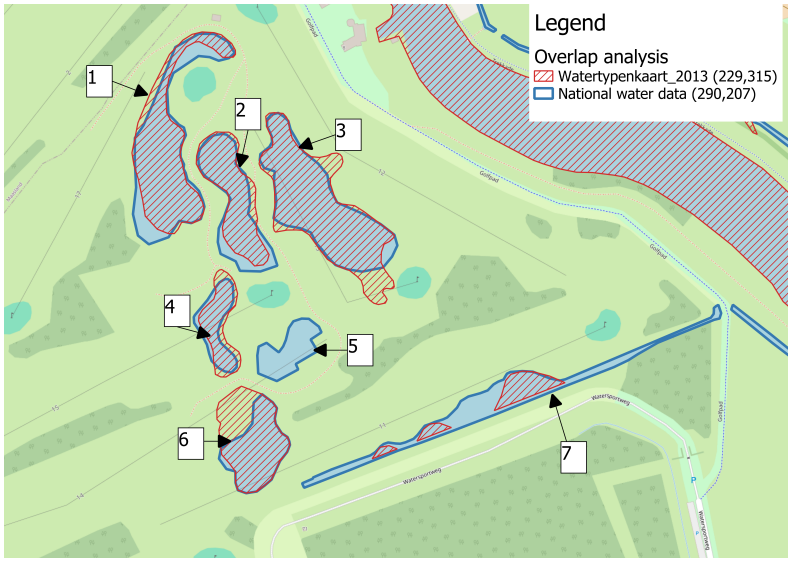

Figure A.6: Example of the spatial overlap analysis near Vlaardingen, Zuid-Holland (51.94°N, 4.32°E). Seven OSM water bodies are displayed with overlap ratios of (1) 79.8%, (2) 81.8%, (3) 96.0%, (4) 85.0%, (5) 0%, (6) 97.2%, and (7) 31.6%, illustrating the Full (90–100%), Partial (50–90%), and None (<50%) agreement categories.

To assess the spatial consistency of the filtered OSM water dataset, it was compared with the Watertypenkaart 2013. The distribution of overlap ratios between the filtered OSM water dataset and the Watertypenkaart 2013 is presented in Figure A.7. The histogram (Figure A.7a) reveals a pronounced bimodal pattern. Approximately 50% of the features fall within the 0–10% overlap range, indicating little to no spatial correspondence with the classified water map. The cumulative distribution function (CDF) (Figure A.7b) confirms that half of all features exhibit minimal overlap. In contrast, a substantial proportion of features (approximately 35%) show very high spatial agreement (90–100%). Features with intermediate overlap (10–90%) are comparatively rare, accounting for roughly 15% of the dataset.

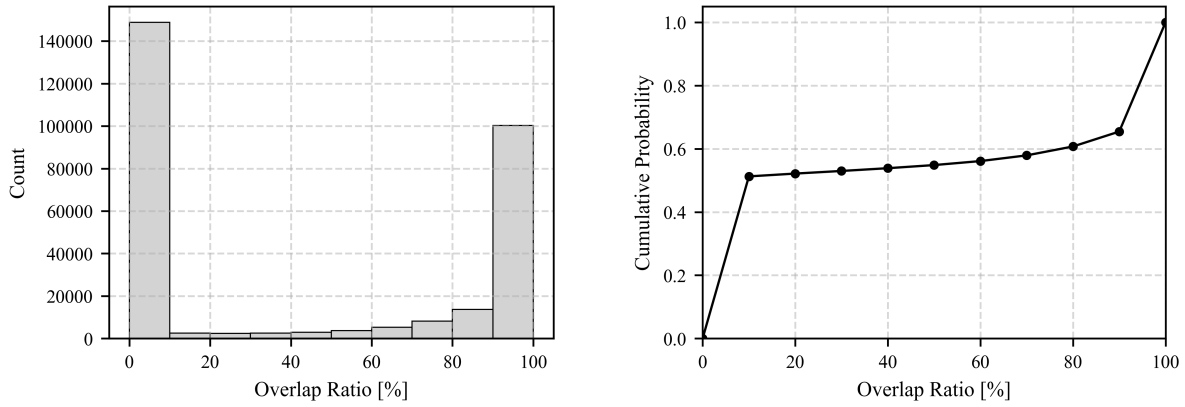

(a) Histogram of overlap ratio

(b) Cumulative distribution function (CDF)

Figure A.7: Distribution of feature-level overlap ratios between filtered OSM water and classified water map.

To further quantify spatial agreement, overlap ratios were grouped into three categories: full (90–100%), partial (50–90%), and none (<50%) coverage (Table A.2). More than half of the OSM features (54.9%) fall into the ”none” category, while 34.5% demonstrate full spatial agreement. Only 10.6% of features exhibit partial overlap. However, when considering total area instead of feature count, a different pattern emerges. Although only one-third of the features fall into the full-overlap category, these account for 87.8% of the total OSM water area. In contrast, the large number of low-overlap features contributes only 271.23 km^2. This indicates that spatial inconsistencies are primarily associated with small water bodies, while the majority of the total water surface area shows strong agreement between datasets. Therefore, the dataset is considered sufficiently reliable for large-scale FPV potential assessment.

Table A.2: Distribution of overlap ratio categories

Category	Overlap ratio (PC)	Count	%	Total area OSM [km^2]	%
Full	90–100%	100,262	34.5	3106.58	87.8
Partial	50–90%	30,755	10.6	159.7	4.5
None	<50%	159,189	54.9	271.23	7.7
Total		290,206	100	3537.51	100

A.6. Site Selection Criteria

Establishing which site selection criteria are relevant for the Netherlands is essential for the identification of the national restricted areas. Table A.3 presents long-term averages of the country’s terrain and climatic parameters, which serve as a basis for defining the site-selection criteria relevant to FPV deployment in the Netherlands.

Table A.3: Long-term averages of terrain and climatic factors of the Netherlands

Variable	Unit	Range	National Average	Source
Daily GHI	[kWh/(m^2*day)]	2.75–3.04	2.86	[106]
Mean Temperature	[°C]	9.8–11.1	10.5	[106]
Terrain elevation	[m]	–8–286	11	[106]
Municipality population density	[inhabitants/km^2]	23–6,868	544	[15, 113]
Wind speed per region	[km/h]	N: 14.4–21.2 E: 12.2–15.1 S: 11.2–15.1 W: 13–23	–	[114]

The values in Table A.3 indicate that the Netherlands is characterized by limited spatial variability in solar irradiation, low and relatively uniform terrain elevation, and moderate climatic conditions [115]. Global horizontal irradiation (GHI) varies only marginally across the country, while elevation and terrain slope are negligible factors due to the predominantly flat landscape. As a result, commonly used ranking criteria such as solar irradiation, elevation, and slope are unlikely to significantly differentiate FPV suitability at the national scale. Consequently, FPV site selection in the Netherlands is primarily governed by the availability of water bodies and by legal or functional restrictions. Exclusion criteria therefore play a dominant role, as they eliminate areas that are unsuitable for FPV deployment, such as protected areas as Natura 2000 zones or water bodies with intensive navigation functions. Ranking criteria, in contrast, would only marginally affect site prioritization under these conditions and are therefore not emphasized in this study.

Based on the literature review, exclusion criteria related to protected areas, heritage sites, military zones, archeological zones, airport zones, aquaculture zones and shipping routes are applied through the exclusion of the occupied areas. For airport zones, a 2.5 km safety buffer is applied to mitigate potential glare impacts on aviation operations [116]. Similarly, for archaeological zones a buffer zone of 2 km is employed. Furthermore, a distance of 50 m from the shoreline buffer zone is implemented. In Table A.4 an overview is given of the literature review's exclusion criteria and their implementation in this study.

Table A.4: Site selection criteria for floating photovoltaic (FPV) deployment based on literature review

Criterion	Implementation in this study	Applied buffer
Legal and Regulatory Constraints		
Protected areas	Implemented (excluded)	None
Archaeological areas	Implemented (excluded)	2 km
Historical, cultural, and heritage sites	Implemented (excluded)	None
Military exercise areas	Implemented (excluded)	None
Airports	Implemented (excluded)	2.5 km
Land and Water Use Constraints		
Ports and shipping routes	Implemented (excluded)	None
Aquaculture zones	Implemented (excluded)	None
Water body function (sea areas, shipping routes)	Implemented (excluded)	None
Water body surface boundary change	Implemented (intermittent water bodies excluded)	None
Environmental and Physical Constraints		
Distance from shoreline	Implemented	Depends on Scenario
Water depth	Indirectly addressed via shoreline buffer	Not applicable

Continued on next page

Table A.4 – continued from previous page

Criterion	Implementation in this study	Applied buffer
Wind speed	Not implemented (insufficient relevance at national scale)	–
Terrain slope	Not implemented (floating systems)	–
Extreme weather	Not implemented (difficult to assess spatially)	–
Technical and Energy-related Criteria		
Water surface area	Implemented through coverage scenarios (5, 10, 15%)	–
Daily solar irradiation	Not implemented (limited spatial variability in the Netherlands)	–
Capacity factor	Not implemented (derived in later analysis)	–
Socio-economic and Infrastructure Criteria		
Distance to residential areas	Not implemented	–
Distance to roads and railways	Not implemented	–
Distance to grid connection	Not implemented	–
Excluded or Non-relevant Criteria		
Sites of Community Interest (SIC)	Not implemented (overlaps with protected areas)	–
Drinking water protection areas	Not implemented	–
Areas of high landscape value	Not implemented	–
Oil and gas exploration blocks	Not implemented	–
Areas licensed for hydrocarbon exploration	Not implemented	–
Offshore renewable energy project zones	Not implemented	–
Gross head	Not relevant for FPV	–
Water body volume	Not relevant for FPV	–
Length–height ratio	Not relevant for FPV	–
Distance from gravel grounds	Not implemented	–

A.7. Datasheet selected FPV module

See next page.

Harvest the Sunshine

605W

JA SOLAR

JAM72D40 MB

Black Frame
n-type Double Glass Bifacial Modules

Premium Cells

n-Bycium+ 16BB

MBB Half-Cell Technology

26%

Up To

Cell Conversion Efficiency

Premium Modules

- Higher power generation better LCOE
- n-type with very Lower LID
- Better Temperature Coefficient
- Better low irradiance response

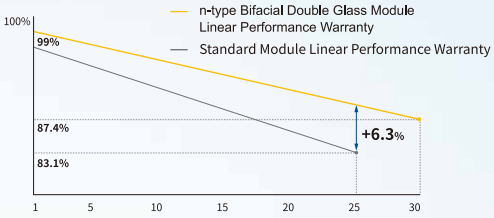

1% 1st-year Degradation

0.4% Annual Degradation Over 30 years

12 12-year product warranty

30 30-year linear power output warranty

Comprehensive Certificates

- IEC 61215, IEC 61730, UL 61215, UL 61730
- ISO 9001: 2015 Quality management systems
- ISO 14001: 2015 Environmental management systems
- ISO 45001: 2018 Occupational health and safety management systems
- IEC 62941: 2019 Terrestrial photovoltaic (PV) modules - Quality system for PV module manufacturing

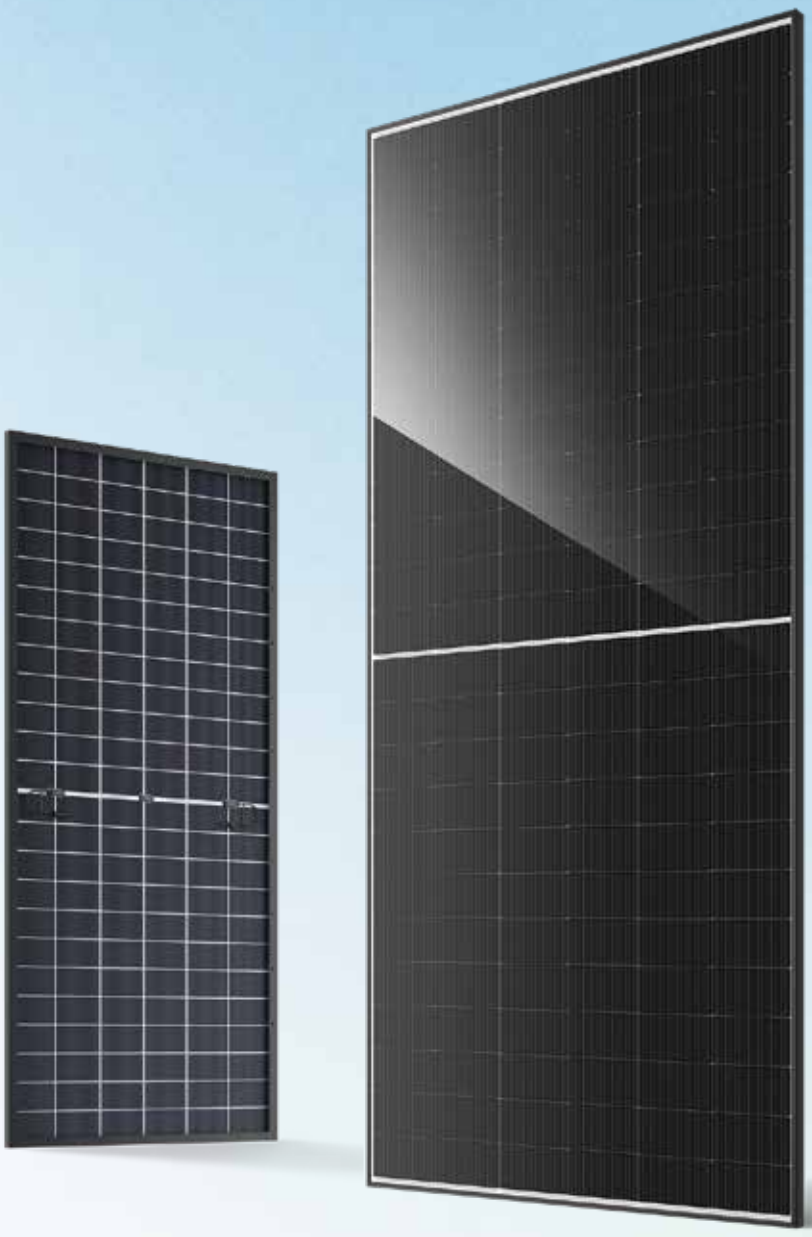

DEEP BLUE 4.0 Pro | OCEANBLUE

JAM72D40 MB n-type Double Glass Bifacial Modules

DEEP BLUE 4.0 Pro | OCEANBLUE

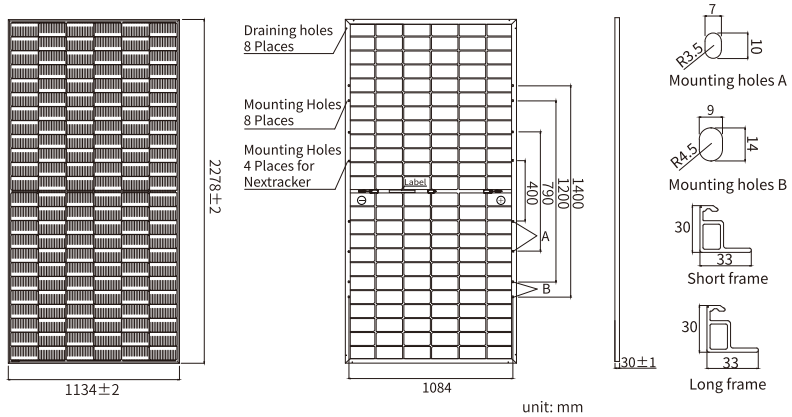

MECHANICAL PARAMETERS

Cell	Mono
Weight	32.2kg
Dimensions	2278±2mm×1134±2mm×30±1mm
Cable Cross Section Size	4mm²(IEC), 12 AWG(UL)
No. of cells	144(6×24)
Junction Box	IP68, 3diodes
Connector	QC 4.10-351/ MC4-EVO2A
Cable Length (Including Connector)	Portrait: 300mm(+) /400mm(-) Landscape: 1300mm(+)/1300mm(-)
Front Glass/Back Glass	2.0mm/2.0mm
Frame	Polyurethane Frame
Packaging Configuration	36pcs/Pallet, 720pcs/40HQ Container

Remark: customized frame color and cable length available upon request

ELECTRICAL PARAMETERS AT STC

TYPE	JAM72D40 -580/MB	JAM72D40 -585/MB	JAM72D40 -590/MB	JAM72D40 -595/MB	JAM72D40 -600/MB	JAM72D40 -605/MB
Rated Maximum Power(Pmax) [W]	580	585	590	595	600	605
Open Circuit Voltage (Voc) [V]	51.95	52.16	52.37	52.58	52.79	53.00
Maximum Power Voltage(Vmp) [V]	44.02	44.22	44.43	44.64	44.85	45.05
Short Circuit Current(Isc) [A]	13.84	13.89	13.94	13.99	14.04	14.09
Maximum Power Current(Imp) [A]	13.17	13.23	13.28	13.33	13.38	13.43
Module Efficiency [%]	22.5	22.6	22.8	23.0	23.2	23.4
Power Tolerance	0~+3%					
Temperature Coefficient of Isc(α_Isc)	+0.045%/°C					
Temperature Coefficient of Voc (β_Voc)	-0.250%/°C					
Temperature Coefficient of Pmax(γ_Pmp)	-0.290%/°C					
STC	Irradiance 1000W/m², cell temperature 25°C, AM1.5G					

Remark: Electrical data in this catalog do not refer to a single module and they are not part of the offer.
They only serve for comparison among different module types.

CHARACTERISTICS

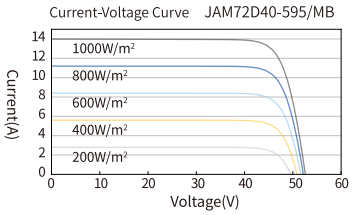

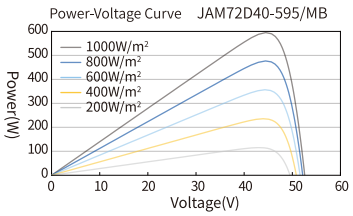

ELECTRICAL CHARACTERISTICS WITH 10% SOLAR IRRADIATION RATIO

TYPE	JAM72D40 -580/MB	JAM72D40 -585/MB	JAM72D40 -590/MB	JAM72D40 -595/MB	JAM72D40 -600/MB	JAM72D40 -605/MB
Rated Max Power(Pmax) [W]	626	632	637	643	648	653
Open Circuit Voltage(Voc) [V]	51.95	52.16	52.37	52.58	52.79	53.00
Max Power Voltage(Vmp) [V]	44.02	44.22	44.43	44.64	44.85	45.05
Short Circuit Current(Isc) [A]	14.95	15.00	15.06	15.11	15.16	15.22
Max Power Current(Imp) [A]	14.23	14.29	14.34	14.40	14.45	14.50
Irradiation Ratio (rear/front)	10%					

* For Nextracker installations, maximum static load please take compatibility approve letter between JA Solar and Nextracker for reference.

OPERATING CONDITIONS

Maximum System Voltage	1500V DC
Operating Temperature	-40°C~+85°C
Maximum Series Fuse Rating	30A
Maximum Static Load, Front*	5400Pa(112 lb/ft²)
Maximum Static Load, Back*	2400Pa(50 lb/ft²)
NOCT	45±2°C
Bifaciality	80%±5%
Safety Class	Class II
Fire Performance	UL Type 29/Class C

JA SOLAR

Headquarters No. 8 Building, Nuode Center, No.1 Courtyard, East Auto Museum Road, Fengtai District, Beijing
Tel: +86 10 6361 1888 Fax: +86 10 6361 1999
E-mail: sales@jasolar.com marketing@jasolar.com www.jasolar.com

Version No. : Global-EN-20241106A

B

Appendix Energy yield

B.1. Shading impact analysis

The solar altitude analysis to determine the impact of the shading of the surrounded trees is explained in this section. The first step was to perform the tree height analysis of the 9 Scenarios in QGIS. To look at all the water bodies at once, the resulting elements of the scenarios of research question 1 were merged into a single dataset with *Union* tool. The following layers: *Scenario 1, 5% (289), Scenario 1, 10% (534), Scenario 1, 15% (645), Scenario 2, 5% (149), Scenario 2, 10% (297), Scenario 2, 15% (371), Scenario 3, 5% (71), Scenario 3, 10% (141), Scenario 3, 15% (139)* were resulted in a unioned layer of 1636 elements. After applying the *Extract by Location* tool using the original water body layer (290,207 elements), 665 elements remained.

A multi-ring buffer was then generated around these elements with distances of 8 m, 16 m, and 24 m. This resulted in three buffer zones, for which the mean distances from the lake were 4 m, 12 m, and 20 m, respectively. Using tree height data from RIVM [90], zonal statistics were applied to each buffer layer. The corresponding average tree heights were found to be 5.93 m, 6.48 m, and 6.63 m.

The solar altitude angle (α) was calculated as a function of tree height and horizontal distance between the trees and the FPV system using Equation B.1. In this equation, the distance represents the sum of the mean buffer distance and the additional offset distance defined for each scenario. The offset distance was defined as the inner buffer distance: 25 m for Scenario 1, 50 m for Scenario 2, and 100 m for Scenario 3.

$$\alpha = \tan^{-1}\left(\frac{\text{Tree Height}}{\text{Distance}}\right) \tag{B.1}$$

The resulting solar altitude angles are presented in Table B.1.

Table B.1: Solar altitude angles based on tree height and distance for different scenarios

Distance mean [m]	Tree height mean [m]	Solar altitude angle [°]		
		Scenario 1 (-25 m)	Scenario 2 (-50 m)	Scenario 3 (-100 m)
4	5.93	11.56	6.27	3.26
12	6.48	9.93	5.97	3.31
20	6.63	8.38	5.41	3.16

For Scenarios 2 and 3, panel tilt angles are incorporated into the system design. These configurations require increased spacing between panel rows, as discussed in Appendix A.2. A trade-off between power density and shading losses resulted in a selected design solar altitude of 14.4°. Since this value exceeds all calculated solar altitude angles in Table B.1, shading from surrounding trees is considered to be implicitly accounted for.

In contrast, Scenario 1 assumes a PV tilt angle of 0°, which is not influenced by the design solar altitude angle, but by the external shading. The initial analysis Table B.1 assumes that the FPV system is located at the edge of the inner buffer zone. However, the system may be positioned farther away from the shoreline, reducing shading effects. Therefore, a second analysis was performed with the inclusion of the positioning of FPV system, to assess the shading impact. The influence of FPV coverage

was evaluated for 5%, 10%, and 15% scenarios. Assuming a square-shaped installation area, the characteristic distance was approximated as $\sqrt{\text{area}}/2$. The effective distance was then calculated using Equation B.2:

$$\text{Distance} = \text{Mean Distance} + \left(\frac{\sqrt{\text{area}_{100\%}}}{2} - \frac{\sqrt{\text{area}_{\text{FPV}-x\%}}}{2} \right) \tag{B.2}$$

Applying this refined distance in Equation B.1 resulted in the average shading angles for Scenario 1, as presented in Table B.2.

Table B.2: Average shading angles for Scenario 1 under different FPV coverage percentages

Coverage	0–8 m	8–16 m	16–24 m	Overall Avg
5%	1.39	1.47	1.45	1.44
10%	2.06	2.14	2.09	2.10
15%	2.57	2.63	2.54	2.58

The refined shading angles are significantly smaller than those obtained from the initial analysis, ranging between approximately 1.4° and 2.6°. This reduction is explained by the increased effective distance between the trees and the FPV system applied in the second approach.

B.2. Wave Induced Losses modelling

The dependence of the Fourier coefficients on the tilt angle was captured using exponential decay functions, and all model parameters were estimated simultaneously using nonlinear least-squares regression. The resulting formulation, given in Equation B.3, expresses WIL as a function of the month of the year t, the tilt angle β, and the angular frequency $\omega = \frac{2\pi}{12}$. The Python code used to estimate the coefficients is provided in GitLab [93].

$$y(t,\beta) = (8.53e^{-0.036\beta}) + (7.15e^{-0.073\beta})\cos(\omega t) + (2.275e^{-0.089\beta})\cos(2\omega t) \tag{B.3}$$

Figure B.1 illustrates the seasonal variation in WIL obtained from this model, demonstrating a good fit to the reported data.

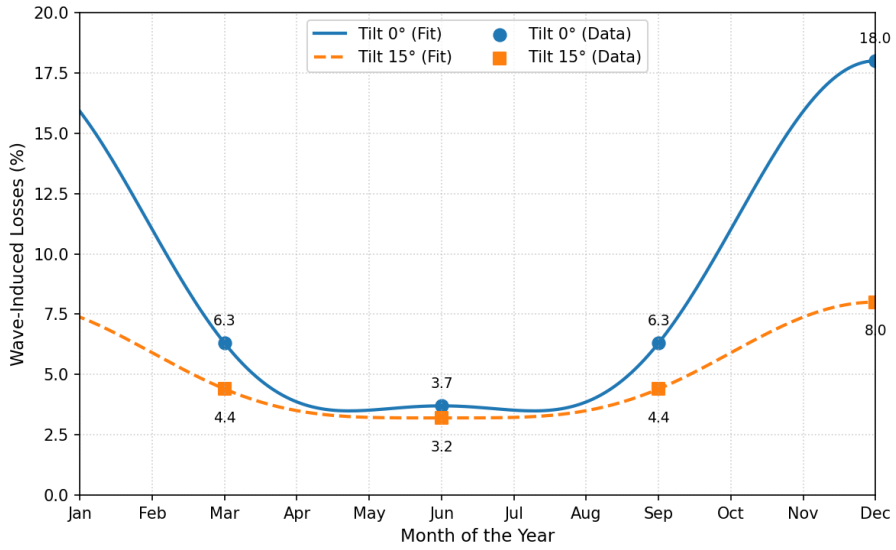

Figure B.1: Wave-induced losses estimated from the data of [79] using a fitted Fourier series for two tilt angles.

Subsequently, WIL were incorporated into the hourly yield calculation, as shown in Equation B.4:

$$P_{actual}(h) = P_{potential}(h) \times \left(1 - \frac{y(t,\beta)}{100}\right) \tag{B.4}$$

B.3. Selection of surface albedo

According to [102, 103] the albedo can be modeled dynamically as a function of solar altitude (α), wave roughness coefficient (r), and color coefficient (c), as shown in Equation B.5 [102, 103], to capture the daily and seasonal variations.

$$\rho = c^{(r \cdot \sin(\alpha)+1)} \tag{B.5}$$

Selecting the conditions of inland waters with clear water without waves ($c = 0.13$, $r = 0.29$) Equation B.5. The average daytime albedo (excluding solar altitude angles of 0) was modeled for the weather stations. As shown in Table B.3, the average daytime albedo across the weather stations ranges between 10.3% and 10.4%. Figure B.2 illustrates the seasonal variation of the average daytime albedo at De Bilt weather station. The Python code used to model the albedo is provided in GitLab [93].

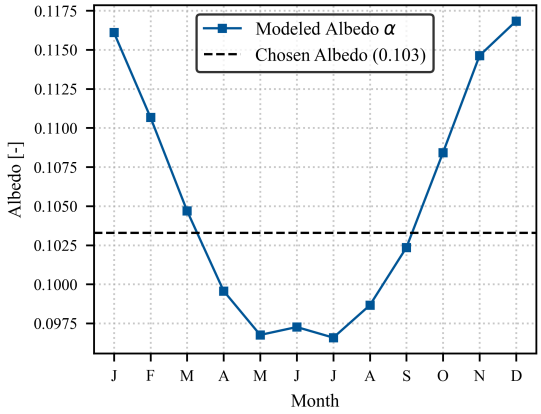

Figure B.2: Daytime Albedo Variation (De Bilt)

Table B.3: Average Daytime Albedo for Weather Stations

Statistic	Station	Albedo [-]
Minimum	Maastricht	0.103
Mean	-	0.103
Maximum	Groningen	0.104
Selected	De Bilt	0.103

Despite the seasonal and daily variability, a constant albedo value was selected because the PVMD Toolbox does not support time-varying albedo inputs. The sensitivity map of the PV module generated within the PVMD Toolbox uses a constant albedo value. Making adjustments to perform this computation for every hour of the year would be computationally intensive. The average daytime albedo at De Bilt was chosen, as it is representative of the values observed across all stations. This value (10.3%) is also consistent with the approximately 10% albedo reported by [101].

B.4. Meteorological data

B.4.1. Selection of meteorological data source

Two meteorological data sources were evaluated for this study:(1) Koninklijk Nederlands Meteorologisch Instituut (KNMI) weather station data (Figure B.3a), (2) Meteonorm version 7.2 (Figure B.3b). The datasets differ in spatial coverage, completeness of irradiance components, and preprocessing requirements.

The **KNMI** operates 37 land stations and 14 offshore stations across the Netherlands [117]. Measurements are recorded at 10-minute intervals and include temperature, relative humidity, wind speed, pressure, precipitation, visibility, cloud cover, and global radiation. Despite the relatively dense station network, several limitations exist:

1. The data of KNMI weather stations is presented in Actual Meteorological Years (AMY).
2. Direct Normal Irradiance (DNI) and Diffuse Horizontal Irradiance (DHI) are not measured directly.

Therefore, additional modeling is required to derive missing irradiance components.

As an alternative, **Meteonorm version 7.2** was evaluated. Meteonorm provides all required parameters directly, including DNI and DHI. Meteonorm generates hourly Typical Meteorological Years (TMY) based on long-term monthly averages using stochastic models. The database integrates approximately 8,325 weather stations worldwide, supplemented with satellite-derived data. In the Netherlands, a total of 34 meteorological locations were used, including both physical weather stations and interpolated city locations, as well as one station situated near the German border (see Table B.4, next page). The

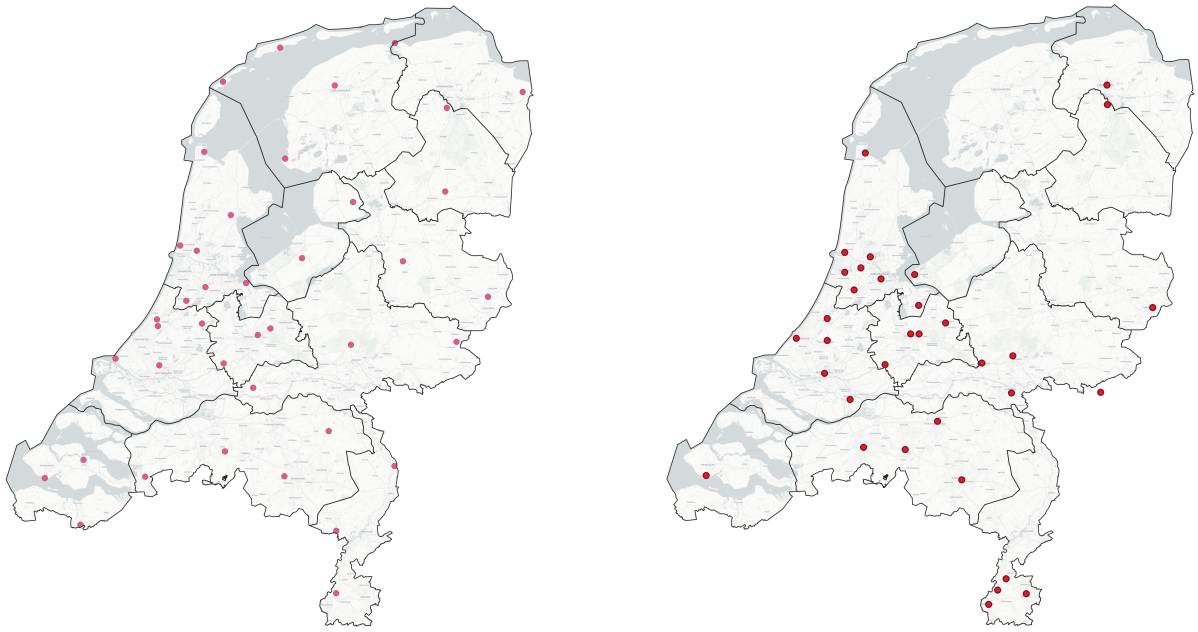

(a) KNMI stations distribution

(b) Meteonorm locations distribution

Figure B.3: Comparison between the distribution of the meteorological data locations

reported uncertainty of solar radiation data in Europe is approximately 3–5% [118]. Compared to KNMI (Figure B.3), the spatial distribution of Meteonorm data points within the Netherlands is more dense and more concentrated around urban areas.

Chosen Dataset

Meteonorm was selected as the primary dataset for this study. The main reason is that the objective of this research is to estimate the long-term average energy yield of floating photovoltaic (FPV) systems. For this purpose, a Typical Meteorological Year (TMY) is more appropriate than an Actual Meteorological Year (AMY), as it avoids bias due to anomalous weather conditions in individual years.

To evaluate the performance of the Meteonorm dataset, measurements from the Baseline Surface Radiation Network (BSRN) station in Cabauw [119] were used as reference. The minute-resolution dataset from November 2005 was aggregated to hourly values. Short-wave downward radiation (SWD) was assumed to represent GHI, direct radiation (DIR) as DNI, and diffuse radiation (DIF) as DHI. Since inconsistencies were observed when verifying the irradiance balance equation, an adjusted GHI was also calculated from DIR and DIF. Both reference GHI values were considered in the comparison. For Meteonorm, only the DNI correction was required. Table B.5 summarizes the comparison.

Table B.5: Comparison of GHI, DNI, and DHI from different datasets with respect to reference. Values are shown as $value \pm error$ (kWh/m² or %).

Dataset	GHI [kWh/m² ± %]	DHI [kWh/m² ± %]	DNI [kWh/m² ± %]	Mean error [%]
Reference	27.128, 26.475 ± -	16.887 ± -	35.942 ± -	-
Meteonorm 7.2	24.935 ± -8.62, -6.15	17.102 ± 2.09	30.537 ± -14.91	-7.15, -6.3

The results show that Meteonorm exhibits deviations of 7% compared to the Cabauw reference. This was expected since the Meteonorm provided TMY data that does not reproduce specific historical months accurately. Still the error is accepted in this study.

Table B.4: Geographical coordinates of the 34 Meteonorm meteorological stations

Location	Latitude (°N)	Longitude (°E)
Almere	52.37	5.15
Amersfoort	52.15	5.38
Amsterdam	52.35	4.90
Arnhem	52.00	5.88
Bocholt*	51.83	6.53
Breda	51.58	4.77
Cabauw	51.96	4.93
De Bilt	52.10	5.18
De Kooy	52.92	4.78
Dordrecht	51.80	4.67
Eindhoven	51.43	5.50
Enschede	52.22	6.92
Geleen Sittard	50.97	5.83
Groningen Eelde	53.13	6.58
Groningen	53.22	6.58
Haarlemmermeer	52.30	4.70
Haarlem	52.38	4.63
Heerlen Kerkrade	50.90	5.98
Hilversum	52.23	5.18
Leiden	52.17	4.50
Maastricht	50.85	5.70
Nijmegen	51.83	5.87
Rotterdam	51.92	4.48
's-Gravenhage	52.08	4.27
's-Hertogenbosch	51.70	5.32
Tilburg	51.57	5.08
Utrecht	52.10	5.12
Velsen Beverwijk	52.47	4.63
Vlissingen	51.45	3.60
Wageningen	51.97	5.65
Zaanstad	52.45	4.82
Zaanstreek	52.40	4.75
Zoetermeer	52.07	4.50
Zuid-Limburg Beek	50.92	5.77

* Bocholt is located in Germany.

B.4.2. Adjustments for solar azimuth and solar altitude variables

The solar azimuth angle (A_z) and solar altitude angle (h_s) are obtained using `pvlib` calculations. The values obtained from the weather stations were compared with the calculated values, revealing some discrepancies. Therefore, adjustments were introduced to ensure consistency between the `pvlib` outputs and the Meteonorm data.

First, for the solar azimuth angle, Meteonorm defines $0°$ as South with a range of $[-180°, 180°]$, whereas `pvlib` defines $0°$ as North with a range of $[0°, 360°]$. To reconcile this difference, Equation B.6 was applied.

$$A_z = A_z(\texttt{pvlib}) - 180 \tag{B.6}$$

However, this transformation resulted in a discontinuity: the first hour yielded positive values, while the subsequent hour yielded negative values. To avoid this artificial jump, the first-hour values were adjusted to negative values to align with the Meteonorm convention. A second adjustment concerns the solar altitude angle. `pvlib` computes the solar elevation relative to the horizon, resulting in negative values during nighttime. In contrast, Meteonorm assigns a value of zero during these periods. Therefore, the solar altitude angle is clipped at zero to ensure consistency.

To evaluate the effectiveness of these adjustments, a leave-one-out cross-validation (LOOCV) approach was applied to 34 weather stations, using 36 solar-noon data points distributed throughout the year. The solar azimuth and altitude angles were calculated for each station and compared with the original values. In Table B.6 the mean, minimum and maximum RMSE statistics are shown for the variables. The RMSE values are quite low.

Table B.6: RMSE statistics across 34 weather stations for solar azimuth angle (A_z) and solar altitude angle (h_s)

Statistic	A_z (°)	h_s (°)
Mean	0.3109	0.1827
Minimum	0.3075	0.1809
Maximum	0.3143	0.1840

The RMSE of the station closest to the average value is presented in Figure B.4. It can be seen that the adjustments in `pvlib` result in a reliable model.

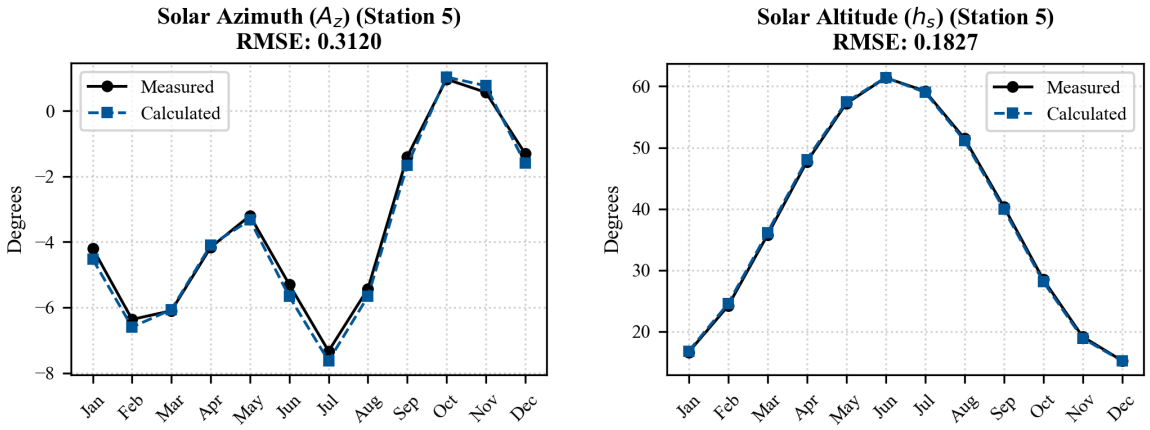

(a) Solar azimuth angle (A_z) estimation

(b) Solar altitude angle (h_s) estimation

Figure B.4: Estimation of calculated variables after `pvlib` adjustments for LOOCV method at 36 days

B.4.3. Spatial interpolation

Before spatial interpolation was applied, the DNI correction was first required (Equation B.7)

$$DNI_{corrected} = \frac{DNI}{\sin(h_s)} \tag{B.7}$$

The very low angles with h_s equal to 0, resulted in invalid values when this was tested on the Meteonorm station de Bilt. Therefore the code has been changed to be equal to 0 below solar altitude angles below 2 degrees. Additionally the corrected DNI was limited to a maximum of 1500 W/m^2. This value was chosen because it is a probable limit. DNI is rarely that value.

To spatially align the other meteorological variables (DNI, DHI, T_a, v_w, GHI) from Meteonorm stations with the floating photovoltaic (FPV) sites, several interpolation techniques were evaluated. These methods estimate meteorological variables at FPV locations based on observations from surrounding weather stations. The following approaches were considered: (1) Baseline, (2) Inverse Distance Weighting (IDW), (3) Radial Basis Function (RBF), and (4) Kriging.

The Baseline method combines linear interpolation with nearest-neighbor matching. When FPV locations lie between two meteorological data points along a defined spatial dimension, linear interpolation is applied. In cases where interpolation is not feasible due to insufficient nearby stations, the value from the nearest meteorological location is assigned to the FPV site.

The second method is the Inverse Distance Weighting (IDW) interpolation technique. IDW is a deterministic method that estimates unknown values by computing a weighted average of surrounding observations, where the weights are inversely proportional to the distance between the interpolation point

and the observation points. Consequently, closer stations exert a stronger influence on the estimated values. In this study, the variables DNI, DHI, GHI, T_a were given a weight of 2, while v_w was given a weight of 3. This distinction was made because the wind speed was most affected by local factors, and weather stations more distant have a lower impact.
Radial Basis Function (RBF) interpolation is another deterministic technique that constructs a smooth surface passing through known data points. It estimates unknown values as a weighted sum of radial basis functions centered at each observation point. Thin Plate Spline was implemented in this study.
Kriging is a geostatistical interpolation technique that incorporates both the distance between data points and the spatial correlation structure of the dataset. In this study, coordinating scaling with 111 was applied to obtain reasonable results, a jitter was introduced, to prevent errors when near stations had similar values, and when the Kriging doesn't work at all, the fallback is to the nearest-neighbor matching.

To evaluate the performance of the interpolation methods, Leave-One-Out Cross-Validation (LOOCV) was applied to 34 weather stations for 36 solar-noon data points, in the exact same way as for the variables A_z, h_s. Table B.7 presents the RMSE values for every variable. As shown in Figure B.5, Kriging (orange bars) and IDW (blue bars) outperform the other interpolation methods across the evaluated variables. Although Kriging yielded the lowest RMSE for four variables (GHI, DNI, DHI, T_a) and IDW performs best for wind speed, Kriging was not selected for implementation due to its high computational cost. Specifically, the method was deemed infeasible for large-scale FPV applications. Consequently, IDW, as the second-best-performing method for most variables and the best-performing method for wind speed, was selected as the interpolation technique for all variables.

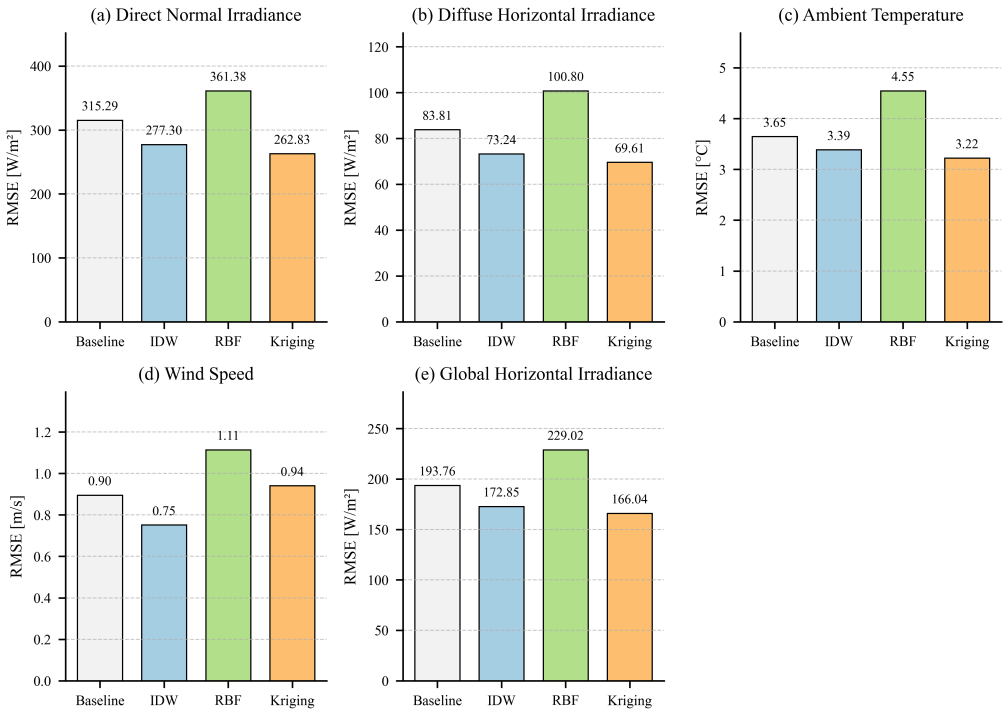

Figure B.5: RMSE comparison for the four interpolation methods across the five evaluated variables

Table B.7: Comparison of interpolation method performance using RMSE for each variable

		Interpolation Method (RMSE)				
Variable	**Unit**	**Baseline**	**IDW**	**RBF**	**Kriging**	**Best**
DNI	W/m^2	315.92	277.30	361.38	262.83	Kriging
DHI	W/m^2	83.81	73.24	100.8	69.61	Kriging
T_a	°C	3.65	3.39	4.55	3.22	Kriging
v_w	m/s	0.90	0.75	1.11	0.94	IDW
GHI	W/m^2	193.76	172.85	229.02	166.04	Kriging

To illustrate the performance of the selected interpolation method, the station with an RMSE closest to the average RMSE of the IDW method was identified and analyzed, see Figure B.6. The variable DNI

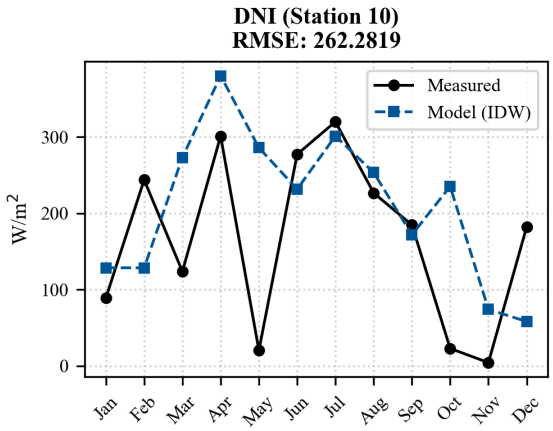

(a) Variable DNI

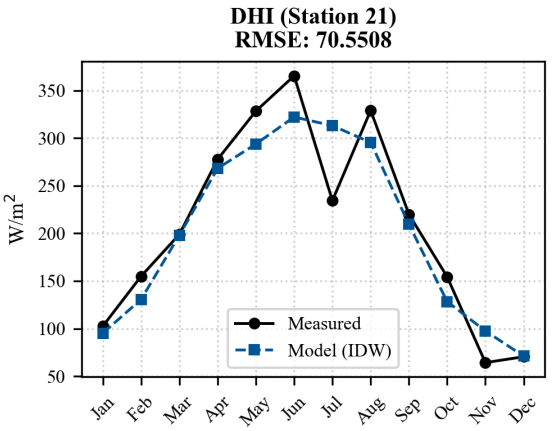

(b) Variable DHI

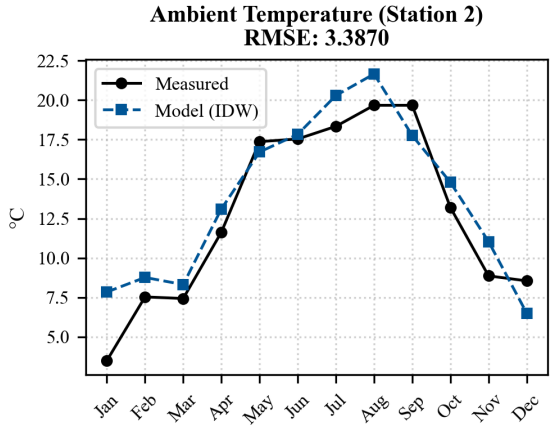

(c) Variable T_a

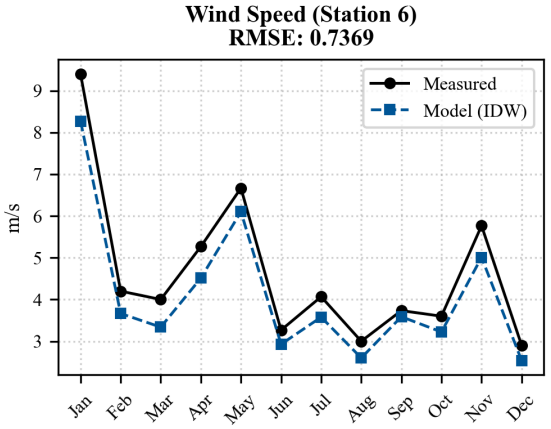

(d) Variable v_w

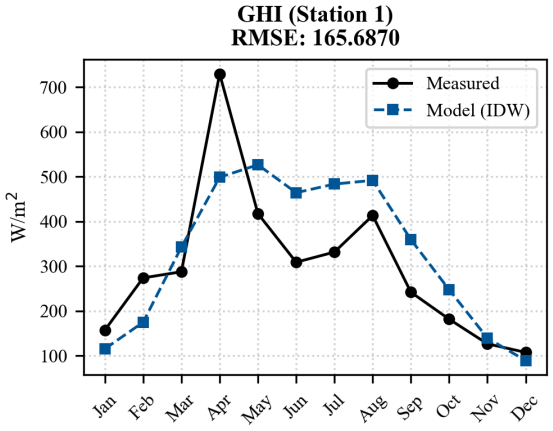

(e) Variable GHI

Figure B.6: Interpolation technique (IDW) performance for 5 variables

(Figure B.6a) and GHI (Figure B.6e) show the largest differences between the measured and estimated values. The variable DNI was corrected with the $\sin(hs)$ term. It might result in some discrephancies. The variable GHI shows the largest difference in the month April, when the GHI has a peak. The measured values are quite spikey, while the model with IDW is more consistent and smooth. Maybe this is

why the differences occur. The variables DHI (Figure B.6b), T_a (Figure B.6c, v_w (Figure B.6d) show a closer resemblence and quite reliable models. A recommendation is to test the variables for the whole year to how large the error is. instead of 36 data points. To further evaluate the reliability of the interpolated values, a comparison was conducted between the ranges of the variables. The annual global horizontal irradiance (GHI) was assessed, the mean values of the variables T_a and v_w were evaluated and the GHI mismatch was further assessed using Equation B.8.

$$GHI = DNI_{cor} \times \sin(h_s) + DHI \tag{B.8}$$

The annual GHI and the mean values of T_a and v_w for the interpolated dataset are all within the range of the available weather station measurements. The GHI mismatch exhibits the largest variation with the interpolated values ranging between 0.5% and -0.4%. Despite this being the largest observed deviation, the magnitude remains very small. Therefore, it is concluded that all variables provide a reliable output for further analysis.

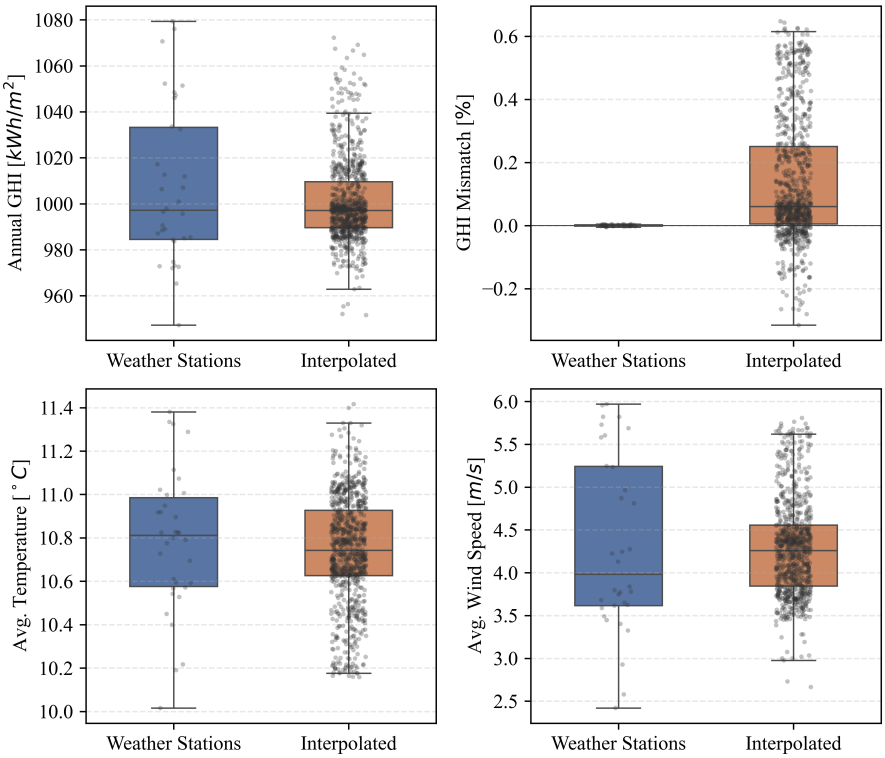

Figure B.7: Ranges of Interpolated elements vs weather stations

B.5. Provincial results

The provincial results for the allocated area (A_{alloc}), total energy yield (EY), and the mean specifc yield (SY_{μ}) are displayed in Table B.8 for Scenario 1 (0° tilt angle, 25 m buffer), Table B.9, for Scenario 2 (15° tilt angle, 50 m buffer), Table B.10 for Scenario 3 (38° tilt angle, 100 m buffer). Each scenario displays the FPV coverage 5%, 10%, 15%. The total is summed up for A_{alloc} and EY, while the national average is taken for SY_{μ}.

Table B.8: Provincial division of potential FPV for Scenario 1, where A_{alloc} is the allocated area in km^2, EY is the energy yield in GWh, SY_{μ} is the mean specific yield in kWh/kWp

Scenario 1	5%			10%			15%		
Province	A_{alloc}	EY	SY_{μ}	A_{alloc}	EY	SY_{μ}	A_{alloc}	EY	SY_{μ}
1. Groningen	0.6	98.5	841.5	1.3	225.8	841.3	2.1	359.6	841.3
2. Friesland	0.6	97.2	850.6	1.6	269.6	849.8	2.4	419.0	849.4
3. Drenthe	0.4	71.4	843.3	1.1	190.4	842.8	1.8	299.5	842.9
4. Overijssel	0.4	72.0	843.0	1.0	166.5	843.7	1.6	274.2	845.3
5. Flevoland	0.2	41.4	850.8	0.6	96.0	850.8	0.9	150.8	850.9
6. Gelderland	0.7	127.5	850.8	1.9	318.4	853.2	3.0	523.1	852.7
7. Utrecht	0.3	58.2	868.4	0.8	142.9	864.9	1.2	214.3	862.1
8. Noord-Holland	0.6	108.0	861.8	1.7	302.9	858.5	2.7	473.8	858.2
9. Zuid-Holland	1.2	222.1	879.3	2.8	489.2	880.1	4.2	755.0	880.4
10. Zeeland	0.3	50.3	900.3	0.6	117.9	906.1	1.0	177.8	905.1
11. Noord-Brabant	1.0	177.0	853.3	2.6	444.6	850.6	4.1	708.7	850.6
12. Limburg	0.7	117.1	879.0	1.6	291.7	882.5	2.6	455.5	881.5
Total	7.1	1240.6	859.0	17.6	3055.9	859.0	27.7	4811.2	858.0

Table B.9: Provincial division of potential FPV for Scenario 2, where A_{alloc} is the allocated area in km^2, EY is the energy yield in GWh, SY_{μ} is the mean specific yield in kWh/kWp

Scenario 2	5%			10%			15%		
Province	A_{alloc}	EY	SY_{μ}	A_{alloc}	EY	SY_{μ}	A_{alloc}	EY	SY_{μ}
1. Groningen	0.5	48.5	894.0	1.2	125.9	893.2	1.9	199.8	892.9
2. Friesland	0.2	26.0	902.7	1.1	119.4	903.9	1.9	197.3	904.4
3. Drenthe	0.2	22.9	895.1	0.8	85.9	897.3	1.2	129.3	897.7
4. Overijssel	0.3	32.2	900.2	0.9	94.8	899.5	1.3	138.9	900.8
5. Flevoland	0.2	20.3	907.3	0.5	52.2	907.1	0.8	81.2	907.1
6. Gelderland	0.5	56.0	908.3	1.6	165.2	909.5	2.6	273.4	911.7
7. Utrecht	0.3	31.6	923.8	0.7	75.8	921.1	1.0	110.5	921.9
8. Noord-Holland	0.5	49.9	919.4	1.3	137.3	915.6	2.0	217.0	910.9
9. Zuid-Holland	1.1	117.2	940.3	2.4	262.1	940.2	3.7	406.4	940.9
10. Zeeland	0.2	23.4	961.9	0.5	56.8	968.9	0.6	71.2	968.6
11. Noord-Brabant	0.8	89.2	911.4	2.1	224.5	909.3	3.5	373.3	908.8
12. Limburg	0.5	59.5	939.0	1.2	136.3	939.8	2.1	231.4	943.1
Total	5.3	576.7	918.0	14.3	1536.2	914.0	22.6	2429.7	914.0

Table B.10: Provincial division of potential FPV for Scenario 3, where A_{alloc} is the allocated area in km^2, EY is the energy yield in GWh, SY_μ is the mean specific yield in kWh/kWp

Scenario 3	5%			10%			15%		
Province	A_{alloc}	EY	SY_μ	A_{alloc}	EY	SY_μ	A_{alloc}	EY	SY_μ
1. Groningen	0.4	26.8	1013.6	1.0	73.3	1016.6	1.3	92.4	1018.7
2. Friesland	0.1	6.3	1029.4	0.4	32.9	1032.1	0.7	55.1	1031.2
3. Drenthe	0.1	9.5	1023.5	0.5	34.2	1020.5	0.6	41.4	1023.2
4. Overijssel	0.1	7.7	1033.2	0.7	50.1	1024.3	1.1	80.6	1024.6
5. Flevoland	0.2	12.6	1034.5	0.3	25.4	1034.5	0.4	31.8	1034.5
6. Gelderland	0.3	24.4	1028.6	0.9	70.1	1035.9	1.3	94.2	1035.0
7. Utrecht	0.2	17.3	1044.3	0.6	44.9	1051.3	0.9	64.9	1053.7
8. Noord-Holland	0.2	16.4	1040.7	0.6	48.6	1040.3	1.0	73.4	1040.3
9. Zuid-Holland	0.9	72.3	1067.0	1.9	150.6	1065.2	2.5	190.1	1066.4
10. Zeeland	0.1	6.4	1123.7	0.3	26.4	1099.6	0.5	36.5	1103.9
11. Noord-Brabant	0.6	48.5	1041.5	1.6	123.7	1033.3	2.5	185.3	1032.9
12. Limburg	0.4	33.1	1071.3	1.0	76.1	1067.6	1.3	97.7	1068.0
Total	3.6	281.3	1047.0	9.8	756.3	1042.0	14.1	1043.4	1041.0

B.6. Spatial distribution of Specific Yield

Figure B.8 (next page) visualizes the spatial variation of the Specific Yield across the three scenarios for the 15% coverage for the range between 810-1130 kWh/kWp.

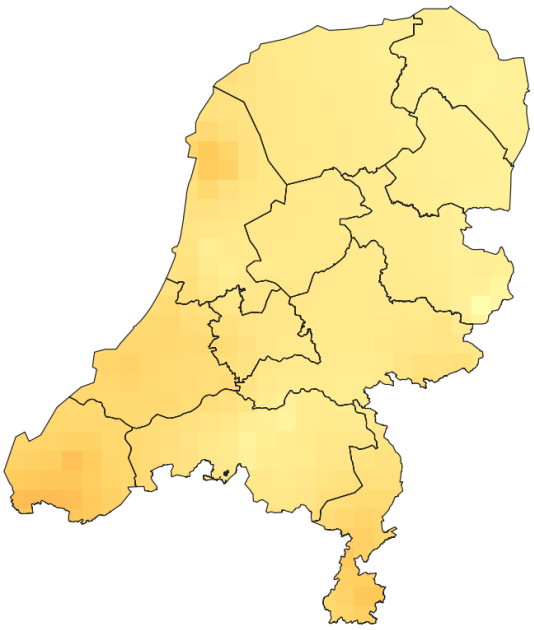

(a) Scenario 1: SY ranging form 814-929 kWh/kWp

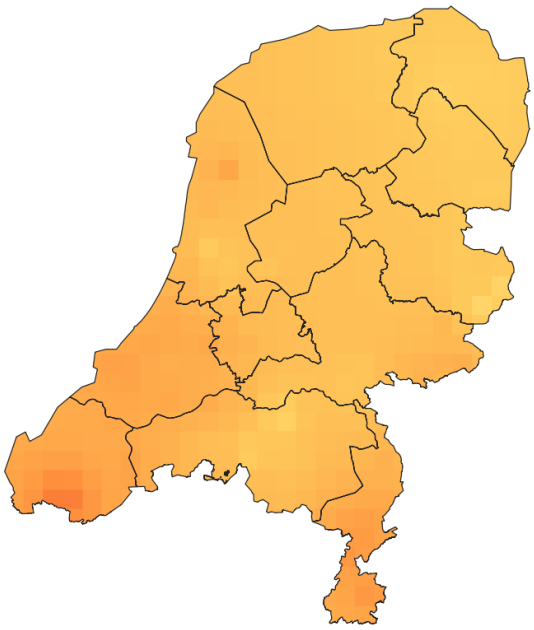

(b) Scenario 2: SY ranging from 886 - 992 kWh/kWp

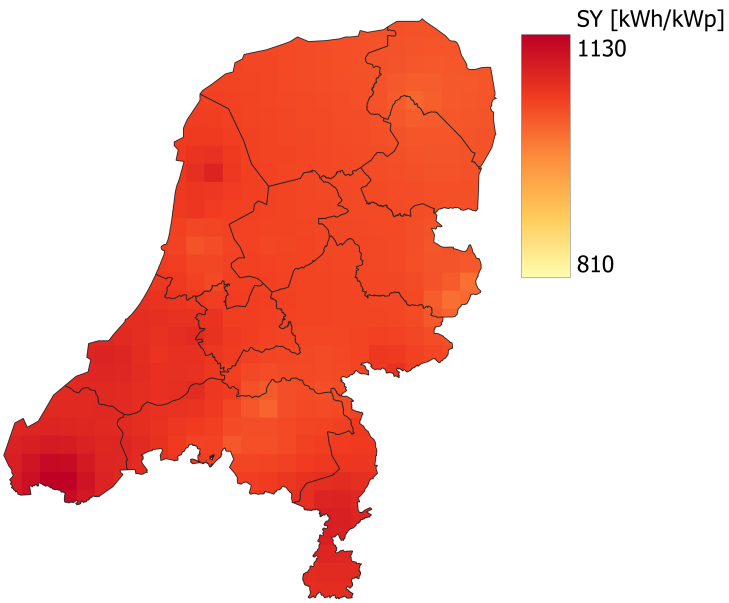

(c) Scenario 3: SY ranging from 981-1124 kWh/kWp

Figure B.8: Comparison of Specific Yield (SY) across three scenarios(coverage percentage 15%)